Exploration of Planetary Bodies with Electrospray Thrusters

by

Oliver Jia-Richards

Sc.B., Massachusetts Institute of Technology (2018)
Sc.M., Massachusetts Institute of Technology (2019)

Submitted to the Department of Aeronautics and Astronautics
in partial fulfillment of the requirements for the degree of

Doctor of Science in Space Propulsion and Controls

at the

MASSACHUSETTS INSTITUTE OF TECHNOLOGY

May 2022

Author . . . .
Department of Aeronautics and Astronautics
March 15, 2022

Certified by. . . . .
Paulo C. Lozano
M. Alemán-Velasco Professor of Aeronautics and Astronautics
Thesis Supervisor

Certified by. . . . .
Youssef M. Marzouk
Professor of Aeronautics and Astronautics
Thesis Committee Member

Certified by. . . . .
Nicholas Roy
Professor of Aeronautics and Astronautics
Thesis Committee Member

Accepted by . . . .
Jonathan P. How
R. C. Maclaurin Professor of Aeronautics and Astronautics
Chair, Graduate Program Committee

Exploration of Planetary Bodies with Electrospray Thrusters

by

Oliver Jia-Richards

Submitted to the Department of Aeronautics and Astronautics
on March 15, 2022, in partial fulfillment of the
requirements for the degree of
Doctor of Science in Space Propulsion and Controls

Abstract

The exploration of planetary bodies such as asteroids can provide insight into the development of the solar system and targets for future *in situ* resource utilization. However, the current paradigm of using a single, monolithic, spacecraft limits the number of asteroid visits to one every few years. By using fleets of standardized small spacecraft, the frequency of asteroid visits could be dramatically increased while simultaneously decreasing the cost per visit. With the development of miniaturized spacecraft systems beginning to mature, attention also needs to be given to methodologies for operating these small spacecraft.

Electrospray propulsion is a promising technology for high-Δv propulsion of small spacecraft due to its mechanical simplicity and scalability. However, methodologies for characterizing the propulsion system thrust on orbit have so far been underdeveloped, and are required for continued development of electrospray thrusters. In addition, the use of electrospray thrusters during operations around or on an asteroid can have further implications. First, the low thrust density of electrospray propulsion, relative to monopropellant or cold-gas propulsion, likely constrains many propulsion architectures to have a single thrust axis with respect to the spacecraft body, complicating the trajectory design process. Second, the ability to operate electrospray thrusters in a bipolar configuration opens up new mission possibilities that leverage intentional charging of the parent vehicle as well as the surface of the planetary body in order to create electric forces for actuation.

This thesis resolves three technical challenges associated with the application of electrospray thrusters for potential planetary exploration missions. Numerical and analytical approaches for inferring the thrust output of a propulsion system based on a simple orbital maneuver are developed. These approaches allow for characterization of the propulsion system performance including quantification in the uncertainty of the thrust output. The controllability of an underactuated spacecraft during proximity operations is also resolved, and an analytical maneuver library is derived in order to guide the spacecraft through different maneuvers. Finally, the application of electric forces for a novel form of actuation on the surfaces of atmosphere-less planetary bodies is analyzed in order to enable a small vehicle to anchor the surface of a rotating asteroid or potentially achieve levitation.

Thesis Supervisor: Paulo C. Lozano
Title: M. Alemán-Velasco Professor of Aeronautics and Astronautics

Acknowledgments

Funding for this research was provided by the NASA Space Technology Mission Directorate through a NASA Space Technology Research Fellowship under grant 80NSSC18K1186 and in part through the Small Spacecraft Technology Program under grant 80NSSC18M0045.

Contents

List of Figures

List of Tables

Chapter 1

Introduction

The exploration of asteroids to determine their composition and characteristics could improve our understanding of the development of the solar system and provide targets for future in-situ resource utilization. Asteroids such as 16 Psyche are hypothesized to be exposed metallic planetary cores [1] whose exploration could provide insight into the formation of planets such as Earth. Asteroid families, groups of asteroids with similar orbital elements, are thought to be the collision products of parent asteroids [2]. Exploration of the members of these families could provide a convenient window into the inside of planetary bodies, but their sheer number requires the capability to perform asteroid missions at a high frequency.

From an engineering perspective, the exploitation of asteroids through mining could allow for *in situ* resource utilization or provide deposits of materials rare on Earth. Carbonaceous-type (C-type) asteroids may contain water [3] which could be used to support life-support systems for human exploration of the solar system or as propellant for propulsion systems to allow for in-flight refueling. It is also believed that metallic-type (M-type) asteroids contain concentrations of platinum-group metals [4], amongst other precious metals, which could be mined and transported back to Earth. However, in order to efficiently perform mining operations, the composition of target asteroids needs to be known *a priori*, or spacecraft need the capability to quickly hop between potential targets.

There are over one million known asteroids in the solar system,[1] of which only 15 have been visited.[2] The current paradigm of using a single, monolithic spacecraft to explore these asteroids limits the number of asteroid visits to one every few years. The size, complexity,

---

[1] https://solarsystem.nasa.gov/asteroids-comets-and-meteors/asteroids/in-depth/

[2] https://ssd.jpl.nasa.gov/sb/targets.html

and uniqueness of each of these spacecraft requires the work of a sizable team of scientists and engineers over long development periods, which creates a bottleneck in terms of how many missions can be performed. Further costs are incurred from the use of a dedicated launch vehicle as well as the daily operations in order to track, communicate with, and ensure the health of the spacecraft.

If instead fleets of standardized small spacecraft were used, the frequency of visits could be significantly increased while simultaneously decreasing the cost per visit. The standardization of components for nano-spacecraft (1-10 kg),[3] through the CubeSat standard [5], has dramatically decreased the cost of spacecraft development to the point that universities can launch their own spacecraft. In addition, since these spacecraft are small, relative to the typical monolithic spacecraft, they can be launched as secondary payloads thereby reducing the cost of launch. A fleet of identical spacecraft could be launched into orbit on a common launch vehicle or be deployed in a convenient location, such as in the asteroid belt, by a mothership. Each spacecraft would then select its own target asteroid, independently propel itself to the asteroid, and then characterize it.

With miniaturized spacecraft subsystems beginning to mature, the feasibility of realizing such a fleet of spacecraft is becoming possible. The Mars Cube One (MarCO) mission,[4] which traveled to Mars with the InSight lander, demonstrated many of he required subsystems for deep-space missions with micro-spacecraft (10-100 kg).[5] The major technology gap for miniaturized spacecraft subsystems after MarCO's success is the development of high-Δv propulsion systems. Since the MarCO spacecraft were able to ride-share to Mars with the InSight lander, their propulsion systems were cold-gas systems intended only for trajectory correction and attitude control maneuvers [6]. However, even if the MarCO team wanted a high-performance (high-Δv) propulsion system, such a system would not have been available. The majority of propulsion systems currently available for small spacecraft are based on cold-gas or monopropellant technology and can only provide enough Δv for small orbit changes [7].

Electrospray propulsion is a promising technology for high-Δv propulsion of nano- and micro-spacecraft due to its mechanical simplicity and scalability. Of particular interest are micro-fabricated ionic-liquid electrospray thrusters which are actively under development at

---

[3] https://www.nasa.gov/directorates/spacetech/small spacecraft/smallsat tech.html

[4] https://www.jpl.nasa.gov/cubesat/missions/marco.php

[5] See footnote 3

multiple institutions. Micro-fabricated ionic-liquid electrospray thrusters make use of near-zero vapor pressure ionic liquids that are fed to the thruster with passive, capillary forces. Such a design eliminates the need for propellant management systems and further reduces the size and mass of the thrusters such that they are compatible with nano- and micro-spacecraft. One of the main limitations of micro-fabricated ionic-liquid electrospray thrusters is their operational lifetime, which limits the throughput, and therefore total impulse, of the propulsion system. However, improvements in micro-fabrication techniques as well as methodologies for bypassing lifetime limitations such as staging [8] mean that a deep-space mission with micro-spacecraft is feasible with current technology [9].

While improvements to miniaturized subsystems have been made, the operation of these spacecraft has been similar to the operation of a monolithic spacecraft, where commands are sent from the ground and the autonomy of the spacecraft is limited to running pre-made procedures. When fleets of spacecraft are involved, the cost and user-time requirements of tracking and communication can be prohibitively expensive and diminish the advantages of small spacecraft. Assuming contact with the spacecraft needs to be made once per week, which may be acceptable during the long-duration transfer to the asteroid, the hourly cost of using NASA's Deep Space Network could be over \$4,000. Once the spacecraft reaches the asteroid and enters proximity operations, contact may need to be made daily. During this period, the hourly cost of using the Deep Space Network could be over \$6,500 [10]. Over the course of a mission, the cost of using time on the Deep Space Network would be comparable to the cost of the entire spacecraft or more. Attention therefore needs to be given to new methodologies of operating small spacecraft, in particular the shift towards semi-autonomous operation in order to minimize the required communication with Earth.

In terms of methodologies for autonomous maneuvering of spacecraft, there is a significant gap between the methods that have been implemented and those that are studied academically. Implemented methods are often simple, with trajectories described analytically, while academic methods are often complex and rely on numerical optimization techniques. Numerical techniques are likely beyond the computational capabilities of current small spacecraft computers. However, even in the future when computational capabilities are increased, numerical techniques often do not have guarantees on if they will find a solution or how long it will take to find one. In addition, on a more subjective level, engineers implementing these methods will not know what trajectory the spacecraft will attempt to take until runtime. While this is not an explicit downside to the performance of the numerical methods, it adds complexity to the verification and validation of the spacecraft's performance before it is launched.

There are other technical challenges outside of trajectory design that also need to be addressed in order to fully enable space exploration with autonomous nano- and micro-spacecraft. Knowledge of the thrust output, including uncertainty quantification, of the propulsion system will be necessary in order for the spacecraft to design appropriate trajectories. Additionally, surface operations is a domain that is typically not considered for nano- and micro-spacecraft, but is an important domain to address when considering the exploration of planetary bodies. The complexity of surface operations will primarily be tied to operating in the low-gravity environments of small asteroids.

The focus of this thesis will be on addressing three research gaps associated with planetary exploration with electrospray thrusters which serve to answer three questions. The first question is how do we infer the thrust output of the propulsion system in low-Earth orbit? Inference of the thrust output will aid both in the development of propulsion systems for nano- and micro-spacecraft and also in future missions where the thrust may be characterized in low-Earth orbit before the spacecraft executes its mission. The second question is how do we guide and control a spacecraft that uses electrospray thrusters during proximity operations? The low thrust density of electrospray thrusters will likely cause the spacecraft to be underactuated and complicate the trajectory design process. The final question is how do we utilize ionic-liquid ion sources for actuation on the surfaces of atmosphere-less planetary bodies? The unique characteristics of ionic-liquid ion sources, such as electrospray thrusters, can enable novel modes of actuation on these atmosphere-less bodies that could dramatically improve our ability to explore their surfaces.

The remainder of this chapter serves as a brief introduction to electrospray propulsion in order to provide technical background for the other chapters. Chapter 2 addresses the question of thrust inference, Chapter 3 addresses the question of proximity operations, and Chapter 4 address the question of surface operations. Due to the disparity of topics for each chapter, literature review is conducted on a chapter-by-chapter basis. In addition, due to the limited number of latin and greek letters, notation is defined on a chapter-by-chapter basis unless otherwise specified.

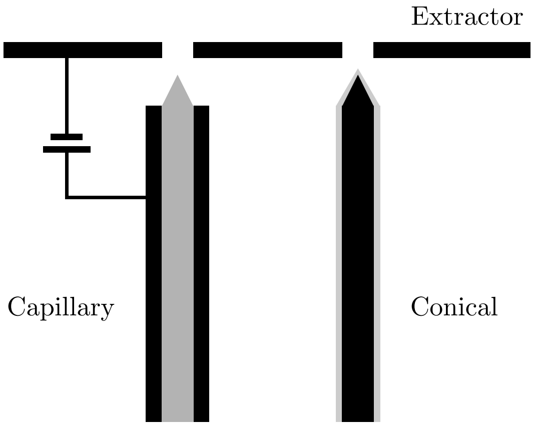

Figure 1-1: Notional diagram of capillary and conical emitters with an extractor grid.

1.1 Electrospray Propulsion

Electrospray thrusters belong to the class of ion engines, where charged particles are accelerated through a potential difference in order to produce thrust. In an electrospray thruster, the charged particles are extracted from an electrically-conductive liquid such as a liquid metal or ionic liquid. Propellant is fed to an emitter and a potential difference is applied between the emitter and an extractor grid. The resulting electric field deforms the liquid and creates a conical meniscus where the upstream pressure, surface tension, and electrical pressure are all at equilibrium. The sharp tip of the cone enhances the electric field to the point that charged particles can be extracted from the emitter and accelerated, out through the extractor grid, to produce thrust.

Figure 1-1 shows notional diagrams of two types of emitter geometries. Capillary emitters simply act as a pathway for the liquid propellant; the liquid is fed to the end of the capillary where the conical meniscus is formed and particles can be extracted. Conical emitters can be used in order to enhance the local electric field and aid in particle extraction. In a conical emitter, propellant can either be fed along the surface of the emitter (externally-wetted) or the emitter material can be porous and allow for propellant to be fed through capillary forces inside the emitter (internally-wetted).

Two regimes of operation can occur. In the pure-ion regime, individual ions are evaporated directly from the liquid. In the cone-jet regime, the tip of the meniscus breaks up into droplets and a jet of droplets is produced. Typically, electrospray thrusters operate in a mixture of the pure-ion and cone-jet regimes where both individual ions as well as droplets are observed. Characteristically, the pure-ion regime exhibits higher efficiencies due to the higher exhaust velocity of the charged particles, while the cone-jet regime exhibits higher thrust-to-power due to the lower specific charge of the droplets. For propulsive efficiency, operation in either the pure-ion or cone-jet regimes is preferred as operation in the mixed regime implies beam polydispersity and therefore a mixture of exhaust velocities.

Electrospray thrusters designed to operate in the cone-jet regime and have been well studied [11, 12, 13]. In terms of in-space operation, these types of thrusters have demonstrated success as high-precision actuators for position and attitude control during the Laser Interferometer Space Antenna (LISA) Pathfinder mission [14]. However, the specific impulse of these thrusters was only around 250 s which is insufficient for high-Δv missions. The power-efficiency of these thrusters is also poor as operating in the pure cone-jet regime (with no direct ion evaporation) is difficult. Evaporated ions contribute negligibly to the overall thrust due to their low mass, but can dominate the current draw, and therefore power draw, of the system. In addition, operation in the cone-jet regime requires active propellant feed systems with bellows, to provide pressure to move the propellant from the tanks to the emitters, as well as values, to control the propellant feed rate [15].

For propulsion of small spacecraft, electrospray thrusters that operate in the pure-ion regime are preferred due to their greater efficiency. In order to reliably achieve the low flow rates required for operation in the pure-ion regime, externally-wetted and internally-wetted emitters are often used. Devices that use liquid metal as their propellant have been considered [16] and developed to the point that they have been operated in space [17]. More recently, ionic liquids have been investigated as a propellant for pure-ion electrospray thrusters. Ionic liquids hold many advantages that improve the scalability of electrospray thrusters, especially for nano- and micro-spacecraft. First, ionic liquids remain in the liquid state at room temperature, and therefore do not require heating like liquid metal propellants. Second, since these liquids are composed of positive and negative ions, they also do not require any pre-ionization and allow for the thruster to fire in either a positive or negative mode. In addition, ionic liquids have negligible vapor pressure at the temperatures experienced by a spacecraft [18, 19], and therefore do not require any form of pressurized containment. These advantages allow for thrusters to be miniaturized to the point that they actually need to be scaled up for use on a nano-spacecraft.

The use of passively-fed ionic liquids for electrospray propulsion was first demonstrated

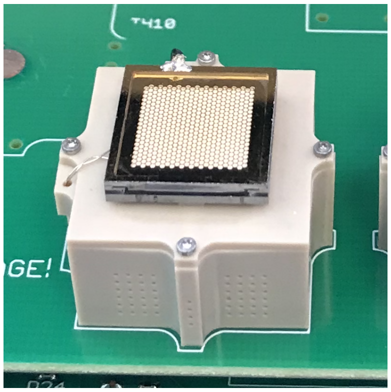

Figure 1-2: Example of an electrospray thruster designed for use on a small spacecraft.

with externally-wetted tungsten emitters [20, 21]. However, the thrust produced by a single emitter is insufficient for main propulsion. In order to produce a device useful for space propulsion, multiple emitters are multiplexed into an array. Typically, these arrays are manufactured from a single piece of porous material with micro-fabrication techniques, creating thrusters composed of hundreds of emitters [22, 23, 24]. Since a single emitter is on the 100-micrometer scale, arrays of hundreds of emitters can be created that are on the single-centimeter scale. Figure 1-2 shows an example of an electrospray thruster designed for use on small spacecraft [24]. The array contains 480 emitters, has a footprint of approximately 1 cm x 1 cm, and is around 2.5 mm tall. A single thruster still does not produce enough thrust for main propulsion except for extremely small spacecraft, only around 12.5 μN, but does have application in precision attitude control [25].

In order to produce enough thrust for main propulsion, arrays of thrusters are used. An array of eight thrusters can provide approximately 100 μN of thrust which may be sufficient for main propulsion of nano-spacecraft [26]. Propulsion system architectures that feature more thrusters can be designed, including those with 36 thrusters [27]. Such a propulsion system could produce a thrust of approximately 0.45 mN. While this level of thrust still seems relatively low compared to other electric propulsion devices, given the low mass of the spacecraft considered, approximately 4 kg for a 3U CubeSat, the net acceleration is comparable to that of other electric propulsion missions such as Dawn [28].

1.2 Staging Systems

While ionic-liquid electrospray thrusters are a promising technology for main propulsion of small spacecraft, their main limitation for application to planetary exploration is their operational lifetime. The miniaturization of propulsion systems typically results in a deterioration of their lifetime. The larger-scale thrusters used during the LISA Pathfinder mission were able to consistently demonstrate lifetimes of over 2,400 hours, limited by the length of the mission, but a cluster of four thrusters had a mass of 14.8 kg [15]. Four microfabricated ionic-liquid electrospray thrusters, fully fueled, have a mass of 14 g [29] and can produce a similar amount of thrust compared to the LISA Pathfinder thrusters. However, microfabricated ionic-liquid electrospray thrusters only have reliably-demonstrated lifetimes of a few hundred hours [24]. While individual tests of single thrusters have demonstrated longer lifetimes, the reliability of these longer lifetimes needs to be confirmed.

For microfabricated ionic-liquid electrospray thrusters, the two main life-limiting mechanisms are propellant accumulation on the extractor grid as well as arcing between isolated tips on the emitter array and the extractor grid. The beam of ions which is extracted from an emitter tip leaves in a conical shape with observed half angles of up to 60 degrees [24]. The beam can therefore impact the extractor grid and allow propellant to accumulate on the extractor grid or backspray onto the emitter array. If enough propellant accumulates, an ionic-liquid connection can form between the emitter array and extractor grid causing an electrical short on the thruster and rendering it inoperable [30]. In addition, not all tips on the emitter array will be identical due to difficulties with repeatable manufacturing and inherent material non-uniformity [31, 32]. The non-uniformity between emitter tips can lead to non-uniformity in the emitted current over a particular array [33]. While most emitter tips will operate as intended, some emitter tips might have unstable menisci [34] which can lead to erratic liquid emission and occasional electrical discharges between the emitter tip and extractor grid [35] degrading the thruster over time.

In order to truly enable deep-space missions where a nano- or micro-spacecraft could independently propel itself from Earth orbit and out into deep space, propulsion systems based on microfabricated ionic-liquid electrospray thrusters need to reliably demonstrated lifetimes of 5,000+ hours [36]. Two strategies could be taken: improve the lifetime of individual thrusters through a better understanding and mitigation of the life-limiting mechanisms

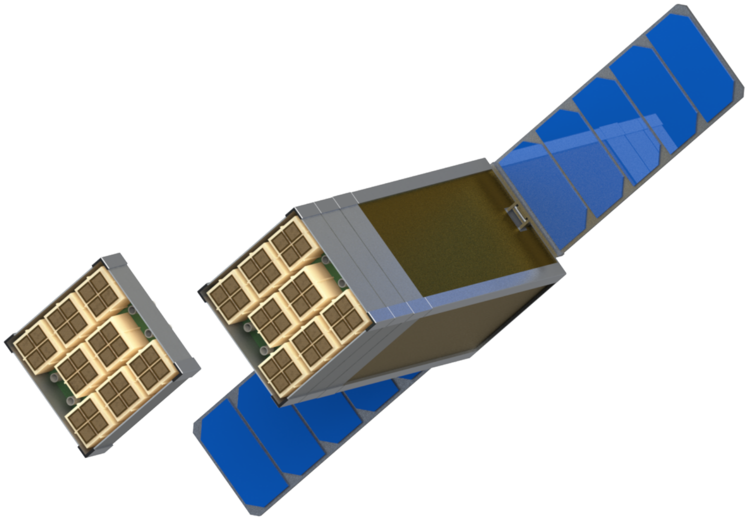

Figure 1-3: Conceptual image of staging on a 3U CubeSat.

or bypass the lifetime limitations of individual thrusters through an alternative method. While the former strategy is continuously being explored and will bring lifetime improvements in the future, if an alternative method can be found, high-Δv capabilities for nano- and micro-spacecraft with existing ionic-liquid electrospray technology could be enabled.

Staging, analogous to launch vehicle staging, is one such alternative method. Instead of the propulsion system consisting of a single array of thrusters, multiple arrays of thrusters are stacked on top of each other. As each array reaches its lifetime limit, it is ejected from the spacecraft, exposing the next array of thrusters which can then continue the mission. Figure 1-3 shows a conceptual image of staging on a 3U CubeSat. Due to the low mass and volume of ionic-liquid electrospray thrusters, multiple stages can be used without significantly increasing the overall mass and volume of the propulsion system.

Staging of ionic-liquid electrospray thrusters, or of space propulsion systems in general, is a recent idea and was first studied for reducing mission times for lunar missions [8]. More recently, work has been conducted to analyze the use of staging systems for missions to near-Earth asteroids [36], demonstrate a staging system in a laboratory environment [37], develop analytical methodologies for analyzing the use of staging systems [38], determine the feasibility of a mission to near-Earth asteroids with staging systems and a MarCO-like spacecraft [9], and provide propulsion system redundancy during the detumbling of small asteroids [39]. Further studies have investigated the use of analytical low-thrust trajectories for guidance of a spacecraft with staging systems between circular orbits [40]. All of this work together shows the feasibility of performing a nano- or micro-spacecraft mission to a near-Earth asteroid, or other destination, with current technology, including some preliminary work towards autonomous guidance of such a spacecraft. Ongoing work aims to perform an on-orbit demonstration of a staging system in the near future [41]. Attention now needs to be given to other technical aspects of such a mission including the thrust inference, proximity operations, and surface operations. This thesis aims to address these aspects.

1.3 Thesis Contributions

1. Evaluation of the use of the ensemble Kalman update for inferring the thrust of low-acceleration propulsion systems in low-Earth orbit including the ability to account for modeling error of the Earth's gravitational field in low-Earth orbit.

2. Derivation of an analytical linear measurement model for thrust inference of low-acceleration propulsion systems in low-Earth orbit as well as optimization of measurement timing in order to minimize the posterior uncertainty in the thrust estimate.

3. Application of polynomial chaos expansions for representing modeling error of the Earth's gravitational field in low-Earth orbit in order to enable rapid predictions of the expected uncertainty from thrust inference of low-acceleration propulsion systems.

4. Application of forced-circular motion in order to stabilize an underactuated spacecraft during proximity operations around a central target and enable the use of low-thrust propulsion systems for remote inspection.

5. Derivation of an analytical maneuver library for maneuvering of an underactuated spacecraft during proximity operations around a central target which can incorporate constraints such as thrust saturation and plume impingement avoidance.

6. Initial feasibility analysis of the use of ionic-liquid ion sources for combined vehicle and surface charging in order to enable electric forces for actuation on the surfaces of atmosphere-less planetary bodies.

Chapter 2

On-Orbit Thrust Inference

One of the last steps in the development of a propulsion system is an in-space demonstration. As part of the demonstration, a measurement of the thrust produced by the propulsion system is usually desired such that the performance in space can be compared to the performance measured in a laboratory environment. Thrust measurements typically rely on using the propulsion system to induce an angular or linear acceleration on the parent spacecraft and measuring the response. Both of these approaches were demonstrated in the Space Electric Rocket Test (SERT) missions: SERT-1 configured the propulsion system to produce torques on the spacecraft and measured the change in the spacecraft's spin rate [42] while SERT-2 configured the propulsion system to produce linear accelerations on the spacecraft and measured the change in the spacecraft's orbital radius [43]. Both spacecraft also carried on-board accelerometers in order to take instantaneous measurements of the acceleration produced by their respective propulsion systems.

In many cases, measurement of thrust through orbital maneuvers may be the desired approach as it imposes the least amount of requirements on the mission. For missions that are not dedicated technology demonstration missions, measuring thrust through angular accelerations by offsetting the thrust vector from the center of mass of the spacecraft requires gimbaling mechanisms or that multiple thrusters be used throughout the primary mission. For some spacecraft this is possible with the desired propulsion system architecture for the mission, as was the case with the Mars Cube One spacecraft [44], but is not always the case. Direct measurement of the propulsive acceleration through an on-board accelerometer that can provide precise measurements of the propulsive acceleration takes away from valuable payload mass and volume, particularly for low-accelerations (order 1 μg).

These problems are exacerbated for small-spacecraft missions which feature reduced budgets and operational support throughout the mission. Development of propulsion systems for small spacecraft is also an extremely active research area. Many low-thrust propulsion systems for small spacecraft such as ionic-liquid electrospray thrusters [24], film-evaporating water microcapillaries [45], miniaturized ion thrusters [46], and plasma thrusters [47, 48] are actively in development and likely will have in-space demonstrations in the near future. Since these propulsion systems are designed for small spacecraft, it is likely that the in-space demonstration will be conducted on a dedicated technology CubeSat demonstration mission.

The combination of low-thrust propulsion with small spacecraft creates a unique challenge for in-space thrust measurements. The low cost and size of the spacecraft likely prohibits the use of accelerometers with precision high enough to directly measure the thrust. Even with a dedicated technology demonstration mission, the small size of the spacecraft can also present issues for measurements relying on angular accelerations due to uncertainty in the lever arm of the propulsion system. For a CubeSat, unless the propulsion system is mounted on an extendable boom, the maximum lever arm will be on the order of a few centimeters. Therefore, uncertainty in the lever arm of the propulsion system of only a few millimeters will lead to errors in the thrust measurement on the order of 10%. Uncertainty in the lever arm can come from many sources including the thruster itself. For example, spatial variation of emission across an ionic-liquid electrospray thruster [33, 49] could lead to variations of the center of thrust of the thruster on the order of a few millimeters, placing an inherent limit on the achievable precision of the thrust estimate.

Due to these limitations, while methods for estimating propulsion system thrust from orbital maneuvers may be desired for general spacecraft, these methods may be required for thrust estimation on CubeSats and other small spacecraft. One of the simplest approaches for estimating thrust from an orbital maneuver is to perform a circular orbit raise. An analytical approximation for the radial position of the spacecraft can be derived

$$r(t) = r(0)\left(1 - \frac{a_\mathrm{p}}{v(0)}t\right)^{-2} \tag{2.1}$$

where r is the spacecraft's radial position, v is the spacecraft's velocity, a_p is the propulsive acceleration, and t is time [50]. By measuring the spacecraft's radial position and inverting

Eq. 2.1, an estimate of the propulsive acceleration can be determined, from which an estimate of the thrust can be obtained. This approach was used during the SERT-2 mission [51] and will be further analyzed in Section 2.7. However, there are many limitations of measuring thrust in this manner. First, it requires that the propulsion system be active for the entire duration of the maneuver which may not be possible, especially for power-limited spacecraft such as CubeSats. Second, only a point-estimate of the thrust is obtained and the uncertainty in the estimate can be difficult to quantify [52]. Last, it is restricted to maneuvers where the spacecraft starts in a near-circular orbit and cannot be generalized to other maneuvers. These limitations mean that changes to the spacecraft's radial position can be used to check that the thrust is close to what is expected [53], but an alternative method for estimating thrust from orbital maneuvers is desired.

Augmented Kalman filters have been considered for maneuver detection of uncooperative satellites [54] and a linear batch filter has been evaluated for estimating thrust from a low-thrust maneuver [55]. However, both of these approaches require linearizing the spacecraft dynamics in order to propagate the spacecraft's state over time. Due to the significant nonlinearity of orbital dynamics, a linearization of the spacecraft's dynamics requires that measurements be taken frequently in order to produce reliable results. Measurement intervals of 1 s [54] and 30 s [55] are used, which may be difficulty to achieve on resource-constrained spacecraft such as CubeSats while also powering an electric propulsion system. Additionally, methods based in linear filtering assume that all uncertainties, such as measurement noise and parameter uncertainty, are Gaussian. While an estimate of the variance in the parameter estimates is provided, it may not reflect the true uncertainty both in terms of magnitude as well as the shape of the distribution.

In this work, an inference approach is considered where the thrust is inferred based on measurements taken over an entire maneuver. Specifically, for a system that can be parameterized by a parameter vector ψ and produces a measurement vector y, Bayes' rule gives that the posterior probability denisty of the parameter vector given the measurement vector is proportional to the product of the likelihood of observing the measurement vector given the parameter vector with the prior knowledge of the parameter vector

$$\mathcal{P}(\psi|y) \propto \mathcal{P}(y|\psi)\mathcal{P}(\psi) \tag{2.2}$$

The goal of this inference method is to generate samples from the posterior distribution $\mathcal{P}(\psi|y)$. By using a sampling-based approach the likelihood probability, $\mathcal{P}(y, \psi)$, and prior probability, $\mathcal{P}(\psi)$, can be any distribution rather than being restricted to Gaussian distributions. Additionally, by using an inference approach, measurements over the entire trajectory are considered simultaneously, allowing the nonlinearities of the spacecraft's dynamics to be explicitly accounted for. Although this method is applicable to any level and duration of thrust, the focus of this work will be on cases with low acceleration as they represent the more-difficult scenario.

2.1 Research Gap

There currently exists a research gap for on-orbit thrust inference based on using the propulsion system to perform an orbital maneuver. Analytical approaches lack the desired accuracy and precision while methods based in linear filtering require linearization of the dynamics and relatively high measurement frequencies. In addition, many methods neglect to account for the possibility of modeling error during simulation, which can cause the resulting predictions to be overly confident.

This work considers the use of the ensemble Kalman update for inferring the propulsion system thrust based on measurements of the spacecraft's position taken during an orbital maneuver. The ensemble Kalman update provides a flexible numerical approach which can account for non-Gaussian distributions as well as potential modeling error. In addition, an analytical formulation of a linear measurement model for thrust inference is derived which can provide insight into the outputs of the ensemble Kalman update and potentially reduce the computational complexity of the thrust inference process. Progress towards the solutions shown here will be published in Refs. [56, 57, 58]. The ensemble Kalman update approach used here has also been considered for thrust inference on a magnetically-levitating thrust balance in a laboratory environment [59] and for inferring the spatial uniformity of emission across an electrospray array [60].

2.2 Ensemble Kalman Update

The ensemble Kalman update [61] is a form of approximate Bayesian inference meaning that the distribution of samples it generates approximates the true posterior distribution.

The idea behind the ensemble Kalman update is the same as the update step of a standard Kalman filter where parameters of inference are updated based on a linear update rule

$$\psi = \psi - K(y - y^*) \tag{2.3}$$

where K is the Kalman gain, y is the vector of simulated measurements based on the current estimate of the parameters, and y^* is the vector of observed measurements. For linear-Gaussian models, the Kalman gain can be calculated analytically based on the measurement model and prior uncertainty in the parameters. However, for models that contain nonlinearities or non-Gaussian distributions an analytical form of the Kalman gain is generally not possible to obtain.

Instead, the ensemble Kalman update attempts to approximate the Kalman gain through Monte Carlo methods. The key idea is that the Kalman gain can be calculated from

$$K = \Sigma_{\psi,y}\Sigma_y^{-1} \tag{2.4}$$

where $\Sigma_{\psi,y}$ is the covariance between the parameters and measurements, and Σ_y is the auto-covariance of the measurements. By generating an ensemble of initial parameter estimates, based on the assumed prior distribution of the parameters, the measurements for each ensemble member can be simulated from a model of the system. With a collection of parameter estimates and corresponding measurements, $\Sigma_{\psi,y}$ and Σ_y can be numerically estimated which allows for an estimate of the Kalman gain to be obtained.

Algorithm 1 shows the ensemble Kalman update routine. The ensemble, Ψ, consists of a collection of parameter vectors. For a given number of ensemble members, each member of the ensemble is generated by randomly sampling a parameter vector from the prior distribution, $\mathcal{P}(\psi)$. Then, a model of the system, $f(\psi)$, is used to generate a simulated measurement vector given the parameter vector for each ensemble member. Given the collection of parameter vectors and simulated measurement vectors, the covariances $\Sigma_{\psi,y}$ and Σ_y are estimated which allows a numerical estimate of the Kalman gain to be obtained. With the estimate of the Kalman gain, the parameter estimates for each ensemble member can be updated using the linear update rule in Eq. 2.3. The posterior distribution of the parameter vectors in the ensemble is then an approximation of the true distribution in Eq. 2.2.

Algorithm 1 Ensemble Kalman update

```
Given observed measurement vector, $y^*$
Initialize ensemble, $\Psi$
Initialize measurement matrix, $\Upsilon$
for each ensemble member $i$ do
    Draw parameter vector from prior, $\Psi_i \leftarrow \mathcal{P}(\psi)$
    Simulate measurement vector, $\Upsilon_i = f(\Psi_i)$
Estimate $\Sigma_{\psi,y}$ and $\Sigma_y$ from $\Psi$ and $\Upsilon$
Estimate Kalman gain, $K = \Sigma_{\psi,y}\Sigma_y^{-1}$
for each ensemble member $i$ do
    Update parameter vector, $\Psi_i = \Psi_i - K(\Upsilon_i - y^*)$
return ensemble, $\Psi$
```

2.3 Dynamics Models

Two models of the dynamics in low-Earth orbit are used in this work: a high-fidelity model for simulating the data that would be collected on-orbit and a low-fidelity model used as the forward model, $f(\psi)$, in the ensemble Kalman update. The high-fidelity model is the General Mission Analysis Tool [62] and uses a 70 x 70 spherical-harmonics representation of the Earth's gravitational field with Joint Gravity Model 3 coefficients [63], the MSISE90 atmospheric model [64], solar radiation pressure, and point-mass representations of the Sun, Moon, and other planets. This model is only used to simulate the data that would be collected on-orbit and is not used during the inference step.

The low-fidelity model only accounts for the gravitational field of the Earth and atmospheric drag, and does not consider solar radiation pressure or the influence of other planetary bodies outside of their impact on an Earth-centered, Earth-fixed reference frame, as they are negligible relative to the gravitational and drag forces. In addition, the spherical-harmonics representation of the Earth's gravitational field is truncated to 30 x 30 and the atmospheric density is assumed to be spatially and temporally constant. In principle, the high-fidelity model could be used in the inference step. However, the use of a low-fidelity model offers two advantages: it reduces the computational complexity of the model and reduces the number of parameters that need to be inferred. In addition, the low-fidelity model alleviates potential issues over overfitting a particular model to the data, particularly for modeling the atmospheric drag.

With the low-fidelity model, the acceleration vector of the spacecraft in an Earth-centered, Earth-fixed frame becomes

$$\vec{a} = \vec{g}(\vec{r}) + \frac{F}{m}\hat{u} - \frac{1}{2}\frac{v^2}{m}\kappa\hat{v} - 2\vec{\Omega} \times \vec{v} - \vec{\Omega} \times \left(\vec{\Omega} \times \vec{r}\right) + \vec{n}(t) \tag{2.5}$$

where $\vec{r}$ and $\vec{v}$ are the spacecraft's position and velocity vectors respectively, v and $\hat{v}$ are the magnitude and unit vector of the spacecraft's velocity, $\vec{\Omega}$ is the rotational frequency of the Earth, $\vec{g}$ is the local gravitational acceleration, F is the propulsion system thrust, m is the spacecraft's mass, $\hat{u}$ is the unit vector of the thrust, and κ is the combined drag coefficient which accounts for the local atmospheric density, ρ, the actual drag coefficient, C_D, and drag area, A

$$\kappa = \rho C_D A \tag{2.6}$$

It is assumed that the atmosphere rotates with the Earth, therefore the appropriate velocity for determining the acceleration due to drag is the spacecraft's velocity in the Earth-centered, Earth-fixed frame. The final term of the acceleration, $\vec{n}(t)$, represented process noise added to the simulation in order to represent modeling error, and will be discussed further in Section 2.4.

Only eight parameters are required in order to simulate a trajectory using the acceleration in Eq. 2.5: the initial position and velocity vectors of the spacecraft, the propulsion system thrust, and the combined drag coefficient. These parameters are therefore the parameters of inference and form the parameter vector ψ

$$\psi = \begin{bmatrix} \vec{r}(0) \\ \vec{v}(0) \\ F \\ \kappa \end{bmatrix} \tag{2.7}$$

The forward model for the ensemble Kalman update is then just a propagation of the spacecraft's position and velocity over time for a particular parameter vector ψ given the acceleration of Eq. 2.5.

Measurements are obtained by taking the spacecraft's position in Cartesian coordinates at desired instances in time and adding additive measurement noise. Noise in the mea-

Table 2.1: Approximate order of magnitude for different sources of modeling error in an Earth-fixed, Earth-centered reference frame. Note that the expected propulsive acceleration is of order 10^{-1} km/hr^2.

Source	Order of Magnitude [km/hr^2]
Earth's gravitational field truncation	10^{-1}
Atmospheric drag	10^{-2}
Moon gravitational acceleration	10^{-2}
Sun gravitational acceleration	10^{-3}
Solar radiation pressure	10^{-3}
Other planets gravitational acceleration	10^{-7}

surements is assumed to be added to all three axes in Cartesian coordinates with the noise along each axis independent of the noise in the other axes. This noise model was chosen for simplicity, but other noise models including those that contain nonlinearities or correlation between noise in the different axes can be used. Unlike in a filtering scheme, the measurement vector, y, includes the spacecraft's position over the entire trajectory rather than at individual instances in time.

2.4 Model Error

One of the key aspects in inferring the probability distribution for the thrust is the handling of modeling error. In this problem, modeling error will be caused by errors in the acceleration applied to the spacecraft from different sources, and will determine the process noise in Eq. 2.5. For the choice of low-fidelity model used in this work, the dominant source of modeling error will be caused by truncation of the spherical-harmonics representation of the Earth's gravitational field. Table 2.1 shows the approximate order of magnitude for different sources of modeling error in an Earth-fixed, Earth-centered reference frame for a near-circular orbit with altitude of 410 km. When calculating the acceleration errors due to atmospheric drag and solar radiation pressure, the spacecraft is assumed to have a drag area of 0.1 m^2, coefficients of drag and reflectivity of 1.0, and mass of 4 kg, representative of a 3U CubeSat.

Figure 2-3 shows the acceleration error in the along-track direction caused by truncating the spherical-harmonics representation of the Earth's gravitational field for a 410 km circular orbit. The magnitude of the acceleration error has some cyclical behavior with period close to the 90 minute orbital period. However, the error qualitatively appears to be random noise.

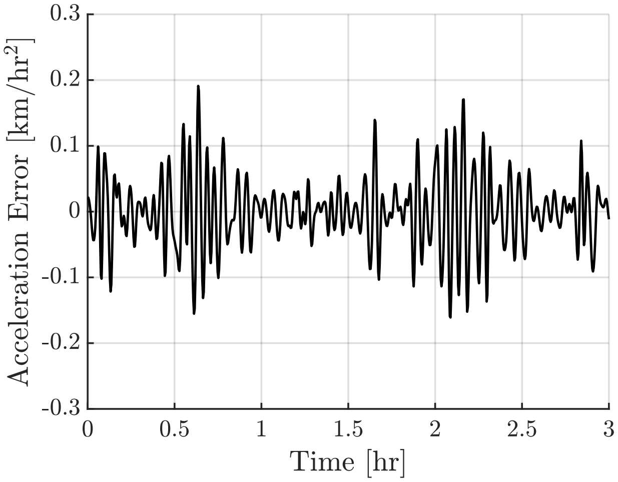

Figure 2-1: Along-track gravitational acceleration error for a 410 km altitude orbit.

Furthermore, Figure 2-2 shows a histogram of the acceleration error which shows that the acceleration error is near-Gaussian. These two aspects combined suggest that generating the process noise for Eq. 2.5 from a Gaussian process may be a reasonable representation of the modeling error due to truncating the spherical-harmonics representation of the Earth's gravitational field.

In order to generate realizations of the process noise from a Gaussian process, the covariance between samples in the process noise needs to be defined. Figure 2-3 shows the sample autocorrelation between samples of the acceleration error with an exponentiated-quadratic curve fit

$$\sigma(\Delta t) = \tau \, \exp\left[-\frac{1}{2}\left(\frac{\Delta t}{L}\right)^2\right] \tag{2.8}$$

where Δt is the time between samples or lag, τ is the scale, and L is the length. The exponentiated quadratic is able to represent the sample autocorrelation for a lag of approximately two minutes and lower, but cannot represent the autocorrelation for longer lags. Instead, samples that are separated by two minutes or greater are assumed to be uncorrelated. Future work will explore the use of different kernels for the Gaussian process in order to better represent the true sample autocorrelation.

With the scale of the kernel determined from Figure 2-2 and the length of the kernel determined from Figure 2-3, realizations of the Gaussian process can be generated that provide a reasonable approximation of the expected modeling error. Figure 2-4 shows one

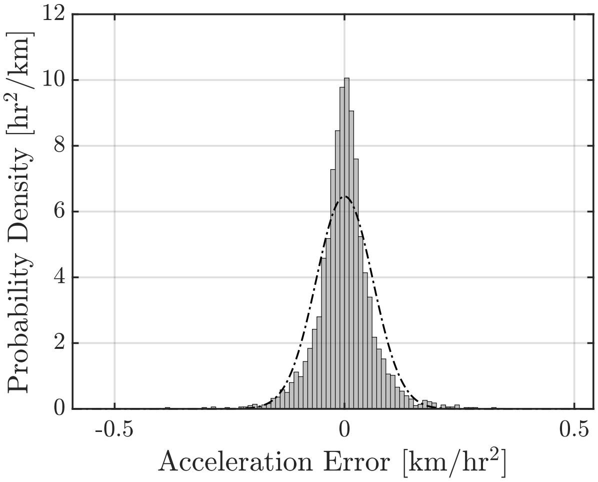

Figure 2-2: Probability density of along-track gravitational acceleration error for a 410 km altitude orbit. Dash-dot line represents a Gaussian fit to the histogram data.

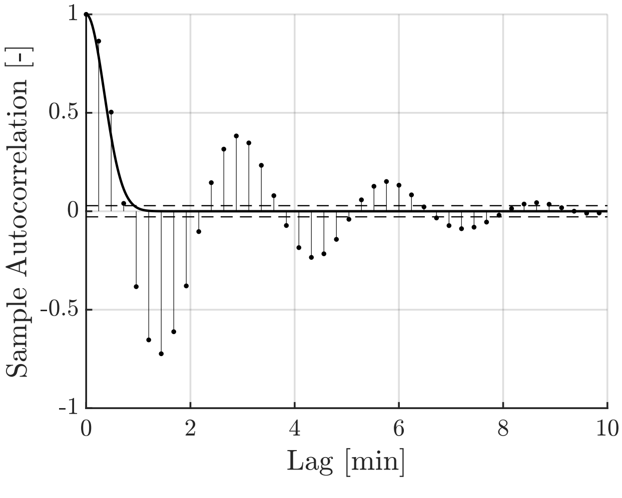

Figure 2-3: Sample autocorrelation of along-track gravitational acceleration error for a 410 km altitude orbit. Solid line represents an exponentiated-quadratic fit to the data.

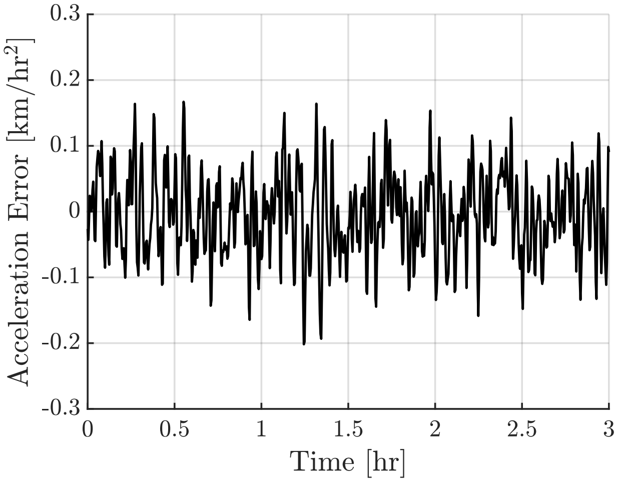

Figure 2-4: Realization of Gaussian process for representing along-track gravitational acceleration error for a 410 km altitude orbit.

such realization for the along-track acceleration error. Qualitatively, it looks similar to the true error in Figure 2-1 but with a greater content of high-frequency noise. The increase in high-frequency noise is caused by the poor representation of the sample autocorrelation for lags greater than two minutes. Although only the noise in the along-track direction is shown here, the same process can be applied to the acceleration error in the radial and cross-track directions to fully represent the process noise.

2.5 Implementation

For this work a simple maneuver is considered where the spacecraft maintains its thrust axis pointed in the angular direction throughout the entire maneuver

$$\hat{u} = \hat{h} \times \hat{r} \tag{2.9}$$

where $\hat{h}$ is the unit vector of the orbit's angular momentum vector, calculated in an Earth-centered inertial frame, and $\hat{r}$ is the unit vector of the spacecraft's position vector. There are no restrictions on the direction of the thrust vector in implementation. However, a thrust vector aligned with either the angular or velocity direction will produce a more significant change in spacecraft state which will lead to better inference of the thrust value. The maneuver is also broken into two distinct phases: a powered phase where the propulsion system maintains a constant thrust and a decay phase where the propulsion system is off and

Table 2.2: Initial spacecraft orbital parameters.

Parameter	Value
Semi-major axis	6,798.0488 km
Eccentricity	0.0003393
Inclination	51.6441 deg
Right ascension of the ascending node	76.2242 deg
Argument of perigee	119.8379 deg
Mean anomaly	30.2224 deg

the spacecraft's orbit is allowed to decay due to atmospheric drag. This maneuver is used to aid in differentiating the effects of atmospheric drag and propulsive thrust. Measurements of the spacecraft's position are collected at a fixed interval over the entire trajectory and used to infer the initial state of the spacecraft, the propulsion system thrust, and the combined drag coefficient. There is no requirement that measurements have to be taken at a fixed interval, and the effects of uneven sampling will be explored in Section 2.9. Gaussian measurement noise with standard deviation of 1/3 m is added to the measurements along each axis to represent measurements taken by a Global Positioning System antenna.

For all results the true spacecraft trajectory is simulated from the initial orbital parameters given in Table 2.2, representative of deployment from the International Space Station. Unless otherwise specified, the initial spacecraft mass was set to 4 kg, the coefficient of drag and coefficient of reflectivity were both set to 1.0, while the drag and solar radiation pressure areas were both set to 0.1 m^2. For the MSISE90 atmospheric model, the $\mathrm{F}_{10.7}$ solar flux and average solar flux were both set to 150 solar flux units while the geomagnetic index was set to 3. The propulsion system was assumed to provide a constant thrust with a specific impulse of 1000 s. While propellant mass flow was simulated, due to the high specific impulse and relatively short maneuver lengths, the impact of propellant mass flow on the trajectory is negligible.

In order to determine the appropriate parameters for the Gaussian processes used to generate realizations of the process noise, an orbit close to the expected orbit of the spacecraft is simulated. This orbit does not need to match the actual orbit of the spacecraft, but should be qualitatively similar such that reasonable estimates of the modeling error can be determined. Based on the simulation of the nearby orbit, the acceleration error in the radial, along-track, and cross-track directions due to truncating the spherical-harmonics

Table 2.3: Gaussian process parameters for representing acceleration error along each axis.

	Scale [km^2/hr^4]	Length [min]
Radial	0.00772	0.446
Along-track	0.00381	0.345
Cross-track	0.00385	0.707

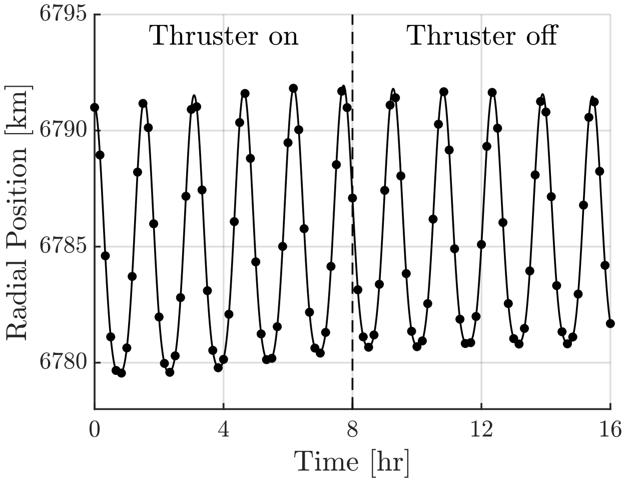

Figure 2-5: Radial position of the spacecraft throughout the proposed maneuver. Markers indicate measurement locations.

representation of the Earth's gravitational field can be determined. A similar process as used in Section 2.4 is used in order to determine the scale and length of the respective kernels. Table 2.3 shows the scale and length of the kernel in all three axes based on a simulation of a 410 km altitude circular orbit.

2.6 Numerical Results

Figure 2-5 shows the radial position of the spacecraft during a 16-hour maneuver where the propulsion system is on for the first eight hours with a thrust of 100 μN and off for the last eight hours. Measurements are taken every 10 minutes for a total of 97 measurement times throughout the entire maneuver. Figure 2-6 shows the marginal probability density of the posterior thrust estimate using an ensemble Kalman update with an ensemble size of 2,500. The posterior distribution is near-Gaussian, represented by the dash-dot line. The posterior distribution has a mean of 98.53 μN and a standard deviation of 1.12 μN giving a 1.47% error in the mean value and 3.36% uncertainty in the estimate (3σ).

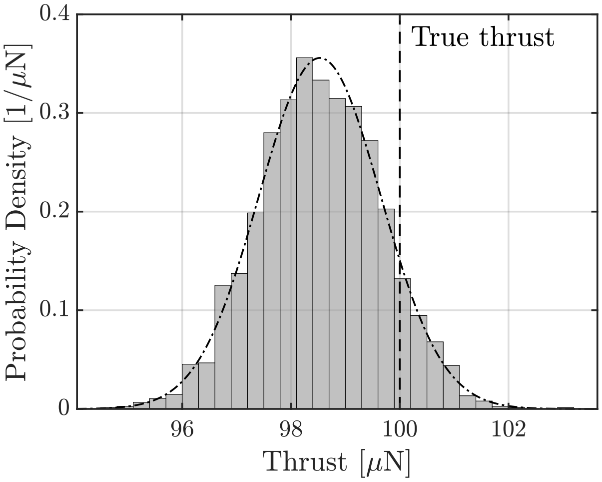

Figure 2-6: Marginal posterior distribution of the thrust estimate obtained using an ensemble Kalman update.

In addition to an estimate of the thrust, the ensemble Kalman update provides an estimate of the average combined drag coefficient throughout the trajectory. Figure 2-7 shows the marginal probability density for the posterior distribution of the combined drag coefficient estimate. The mean of the distribution is approximately 0.476 μg/km which for a coefficient of drag of 1.0 and a drag area of 0.1 m^2 indicates an average atmospheric density of approximately 4.76 g/km^3. This average atmospheric density is reasonably close to the expected average atmospheric density for a ∼410 km altitude orbit [65]. Figure 2-8 shows a scatter plot of the thrust and combined drag coefficient for the posterior ensemble members. There is a clear positive correlation between the thrust and combined drag coefficient estimates which is to be expected; trajectories with a larger combined drag coefficient require larger thrust values in order to explain the data.

One of the key advantages of using the ensemble Kalman update is that it automatically quantifies uncertainty in the parameter estimates by providing a full estimate for the probability density of the posterior distribution. As such, the effects of different parameters of the maneuver can be explored. First and foremost, since the propulsion system alters the spacecraft's trajectory by providing an acceleration, the uncertainty in the thrust estimate actually comes from an uncertainty in the acceleration. Therefore, for two different spacecraft, if the propulsive acceleration is the same then the uncertainty in estimating the propulsive acceleration should be constant and the difference in uncertainty in the thrust should be proportional to the difference in mass. To illustrate this, Figure 2-9 shows the

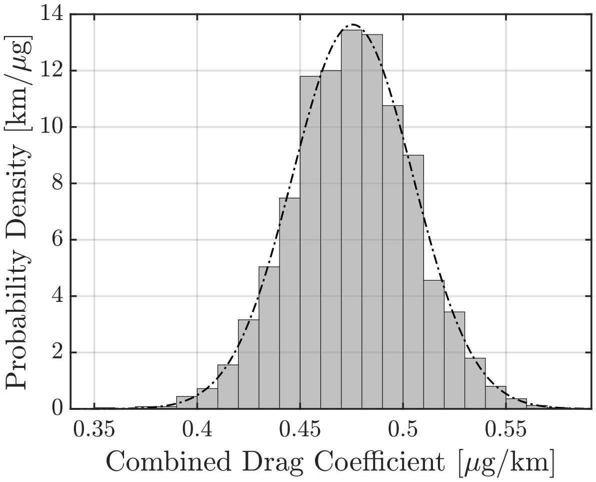

Figure 2-7: Marginal posterior distribution of the combined drag coefficient estimate obtained using an ensemble Kalman update.

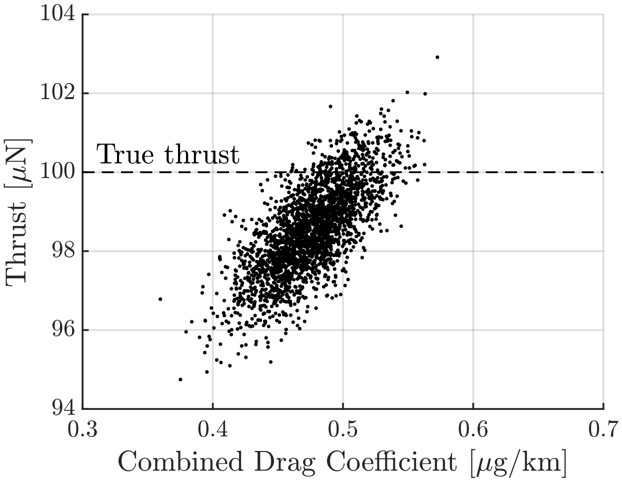

Figure 2-8: Scatter plot of the posterior ensemble showing the correlation between estimates of thrust and combined drag coefficient.

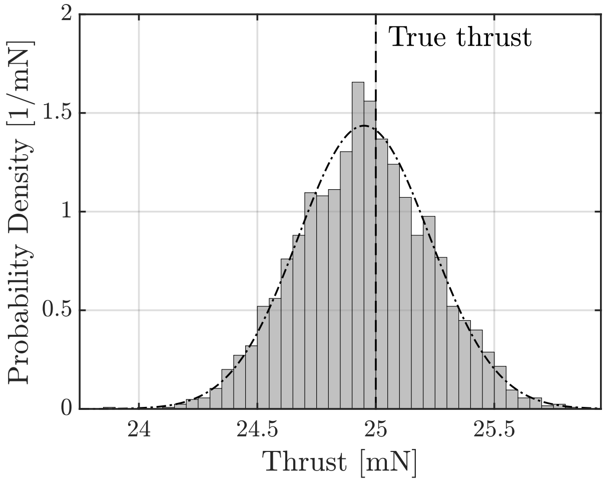

Figure 2-9: Marginal posterior distribution of the thrust estimate obtained using an ensemble Kalman update. Both the thrust and spacecraft mass were increased by a factor of 250 from previous simulations.

marginal probability density of the posterior thrust estimate for the same scenario as before, but for a spacecraft mass of 1000 kg and propulsion system thrust of 25 mN. Since both the mass and thrust are increased by a factor of 250, the propulsive acceleration is the same as before: 2.55 μg. Previously, for a spacecraft mass of 4 kg and thrust of 100 μN, the posterior uncertainty in thrust was 1.12 μN which corresponds to an acceleration of 28.5 ng. Here, the standard deviation of the posterior thrust distribution is 0.278 mN which corresponds to an acceleration of 28.3 ng.

Since the uncertainty in the thrust estimate is inherently tied to propulsive acceleration, the trends in posterior uncertainty in the propulsive acceleration are explored versus other maneuver parameters. Figure 2-10 shows the standard deviation of the marginal posterior distribution of the propulsive acceleration for different values of the true propulsive acceleration. In all cases the maneuver was fixed to eight hours of thruster firing and eight hours of decay due to drag with measurements taken every 10 minutes. Within numerical noise, the standard deviation is constant with propulsive acceleration.

Figure 2-11 shows the standard deviation of the posterior marginal distribution of the propulsive acceleration for different maneuver durations. For a given maneuver duration, the propulsion system is active for the first half of the maneuver duration and off for the second half of the maneuver duration. In all cases, the true propulsive acceleration was fixed to 25 $\mu\text{m/s}^2$ and 50 measurements were taken throughout the maneuver. The standard deviation

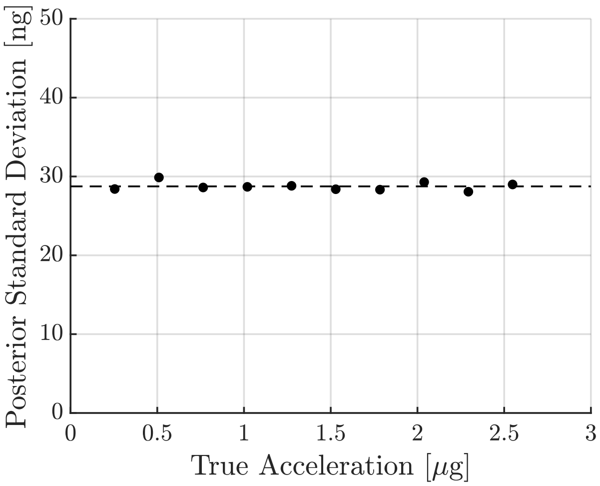

Figure 2-10: Standard deviation of the posterior marginal distribution of the propulsive acceleration versus true acceleration value.

decreases approximately as $T^{-0.8}$ where T is the maneuver duration.

Figure 2-12 shows the standard deviation of the posterior marginal distribution of the propulsive acceleration for different measurement intervals. In all cases the true propulsive acceleration was fixed to 25 μm/s^2 and the maneuver was fixed to eight hours of propulsion system firing and eight hours of decay due to atmospheric drag. The dependence of the standard deviation on measurement interval is exceedingly weak, with the dependence corresponding to approximately $\Delta t^{0.05}$ until measurement intervals below approximately five minutes are used.

These trends in the standard deviation of the posterior propulsive acceleration allow results obtained for one maneuver to be generalized to other cases. In addition, if a particular standard deviation is observed for a given maneuver it is relatively easy to determine how to alter the maneuver in order to achieve a desired level of uncertainty. Minor improvements to the posterior uncertainty can be achieved by taking more measurements throughout the maneuver through reducing the measurement interval. Alternatively, if a larger decrease in the posterior uncertainty is required, then it may be better to increase the overall length of the maneuver. A final method of decreasing the uncertainty in the propulsive thrust would be to reduce the mass of the spacecraft. Since the posterior uncertainty in propulsive acceleration will remain constant for different propulsive accelerations, using the same propulsion system on a lighter spacecraft will result in decreased uncertainty in the thrust. Potential explanations for some of the trends observed here will be discussed in Section 2.7.3.

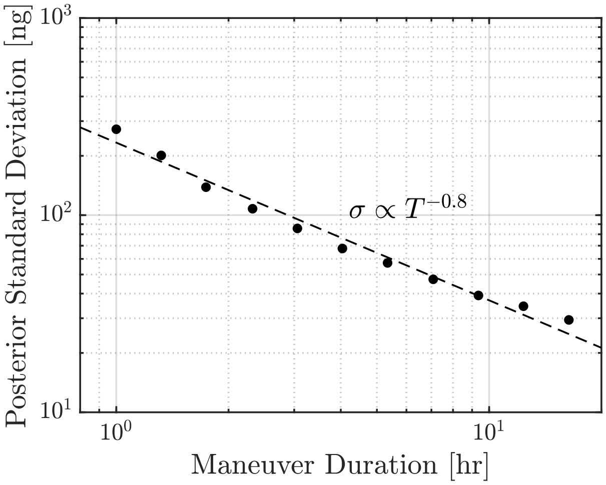

Figure 2-11: Standard deviation of the posterior marginal distribution of the propulsive acceleration versus maneuver duration.

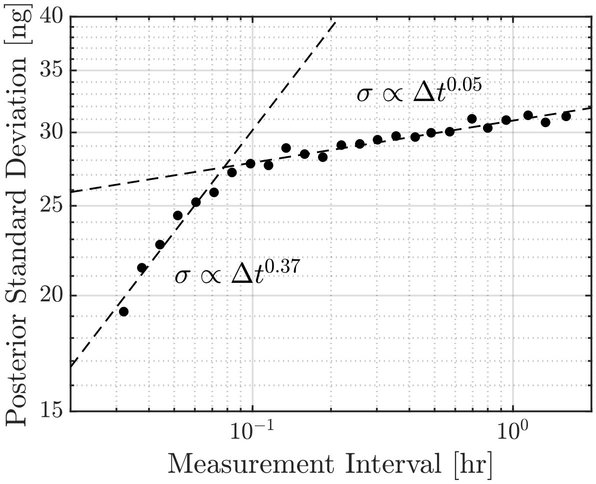

Figure 2-12: Standard deviation of the posterior marginal distribution of the propulsive acceleration versus measurement interval.

The posterior uncertainty in the propulsive acceleration is driven by the process noise used to represent modeling error. The theoretical limits in posterior uncertainty for an ensemble Kalman update can be estimated by using the low-fidelity model to both generate the observed data and for inference, eliminating the need to introduce process noise as there is no modeling error. Figure 2-13 shows the standard deviation of the posterior marginal distribution of the propulsive acceleration for exactly this case. Comparing to Figures 2-11 and 2-12, a reduction in posterior standard deviation of the propulsive acceleration of over an order of magnitude is observed. For an uncertainty threshold of 30 ng (1σ), a two-hour maneuver could be used if the inference model perfectly represents the true system dynamics whereas a 16-hour maneuver was required when the data were generated with the high-fidelity model.

Another interesting aspect of Figure 2-13 is the rate of convergence in the posterior standard deviation. Looking at the dependence with maneuver duration, for short maneuver durations (<0.3 hr) the posterior standard deviation is constant with maneuver duration and for long maneuver durations (>2 hr) the posterior standard deviation decreases quadratically with maneuver duration. Between these two regions is a transitional region where the posterior standard deviation decreases almost linearly with maneuver duration. It is likely that the constant standard deviation for short maneuver durations is due to the posterior standard deviation being close to the prior standard deviation. For the dependence with measurement interval, a clear trend of the standard deviation scaling with $\sqrt{\Delta t}$ where Δt is the measurement interval can be observed. Potential explanations for these trends will be further discussed in Section 2.7.3.

2.7 Linear Measurement Model

In order to better understand the outputs of the ensemble Kalman update and improve the computational efficiency of thrust inference, an analytical approach to the thrust inference problem is desired. Specifically, a linear measurement model of the form

$$\Delta y = H\Delta\phi + \nu \tag{2.10}$$

is sought where Δy corresponds to small changes in the measurements, $\Delta\phi$ corresponds to small changes in the input parameters, H is the sensitivity matrix, and ν is measurement

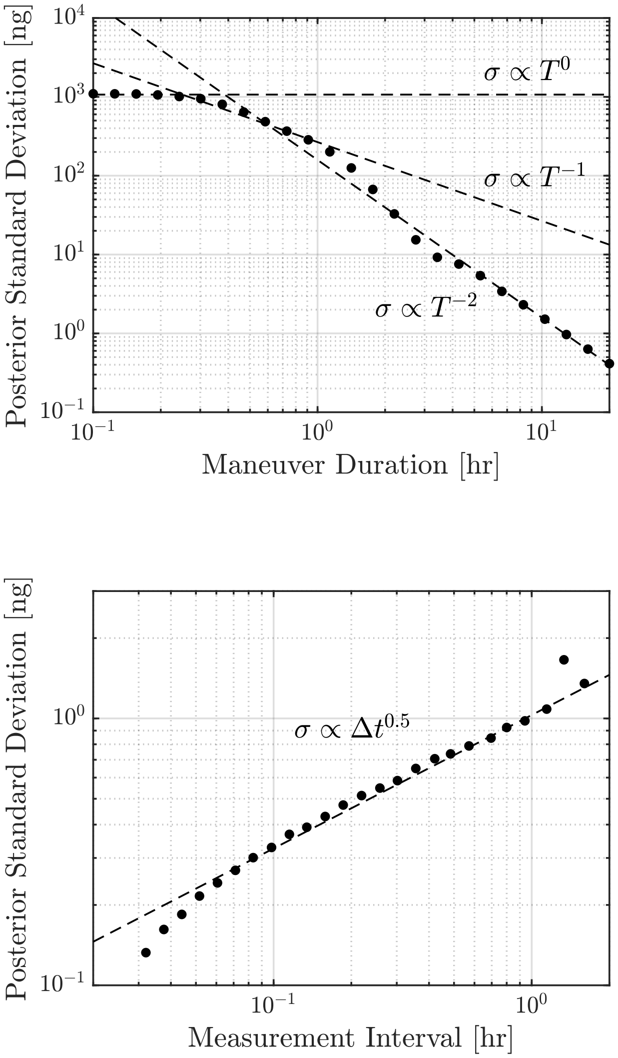

Figure 2-13: Standard deviation of the posterior marginal distribution of the propulsive acceleration versus maneuver duration and measurement interval with no modeling error.

noise. The primary goal of this section is to derive an analytical form of H which determines how small changes to the input parameters affect the observed measurements.

In order to derive the sensitivity matrix, a modified form of the thrust inference problem is used where the measurements are taken to be in a local-vertical, local-horizontal frame rather than the Cartesian coordinates used previously. Small changes to the measurement vector are then

$$\Delta y = \begin{bmatrix} \Delta r(t_1) \\ \vdots \\ \Delta r(t_m) \\ \Delta s(t_1) \\ \vdots \\ \Delta s(t_m) \end{bmatrix} \tag{2.11}$$

where $\Delta r(t)$ correspond to small changes in the radial position, $\Delta s(t)$ correspond to small changes in the along-track position, and $t_1, \ldots, t_m$ are the discrete measurement locations. Two parameter vectors will be considered here. One where atmospheric drag is neglected and the parameters of inference correspond to the initial radial and along-track position and velocity of the spacecraft as well as a propulsive acceleration. This case will be referred to as the "one-acceleration" case and small changes in the parameter vector are given by

$$\Delta \phi_1 = \begin{bmatrix} \Delta r_0 \\ \Delta s_0 \\ \Delta v_{r,0} \\ \Delta v_{s,0} \\ \Delta a_{\mathrm{p}} \end{bmatrix} \tag{2.12}$$

In this scenario, the sensitivity matrix H_1 is

$$H_1 = \begin{bmatrix} \frac{\partial}{\partial r_0} r(t_1) & \frac{\partial}{\partial s_0} r(t_1) & \frac{\partial}{\partial v_{r,0}} r(t_1) & \frac{\partial}{\partial v_{s,0}} r(t_1) & \frac{\partial}{\partial a_{\mathrm{p}}} r(t_1) \\ \vdots & \vdots & \vdots & \vdots & \vdots \\ \frac{\partial}{\partial r_0} r(t_m) & \frac{\partial}{\partial s_0} r(t_m) & \frac{\partial}{\partial v_{r,0}} r(t_m) & \frac{\partial}{\partial v_{s,0}} r(t_m) & \frac{\partial}{\partial a_{\mathrm{p}}} r(t_m) \\ \frac{\partial}{\partial r_0} s(t_1) & \frac{\partial}{\partial s_0} s(t_1) & \frac{\partial}{\partial v_{r,0}} s(t_1) & \frac{\partial}{\partial v_{s,0}} s(t_1) & \frac{\partial}{\partial a_{\mathrm{p}}} s(t_1) \\ \vdots & \vdots & \vdots & \vdots & \vdots \\ \frac{\partial}{\partial r_0} s(t_m) & \frac{\partial}{\partial s_0} s(t_m) & \frac{\partial}{\partial v_{r,0}} s(t_m) & \frac{\partial}{\partial v_{s,0}} s(t_m) & \frac{\partial}{\partial a_{\mathrm{p}}} s(t_m) \end{bmatrix} \tag{2.13}$$

The second parameter vector considers two accelerations that act on the spacecraft, a_1 and a_2, which can represent the propulsive acceleration and atmospheric drag acceleration respectively. This case will be referred to as the "two-acceleration" case and small changes in the parameter vector are given by

$$\Delta\phi_1 = \begin{bmatrix} \Delta r_0 \\ \Delta s_0 \\ \Delta v_{r,0} \\ \Delta v_{s,0} \\ \Delta a_1 \\ \Delta a_2 \end{bmatrix} \tag{2.14}$$

In this scenario, the sensitivity matrix H_2 is

$$H_2 = \begin{bmatrix} \frac{\partial}{\partial r_0} r(t_1) & \frac{\partial}{\partial s_0} r(t_1) & \frac{\partial}{\partial v_{r,0}} r(t_1) & \frac{\partial}{\partial v_{s,0}} r(t_1) & \frac{\partial}{\partial a_1} r(t_1) & \frac{\partial}{\partial a_2} r(t_1) \\ \vdots & \vdots & \vdots & \vdots & \vdots & \vdots \\ \frac{\partial}{\partial r_0} r(t_m) & \frac{\partial}{\partial s_0} r(t_m) & \frac{\partial}{\partial v_{r,0}} r(t_m) & \frac{\partial}{\partial v_{s,0}} r(t_m) & \frac{\partial}{\partial a_1} r(t_m) & \frac{\partial}{\partial a_2} r(t_m) \\ \frac{\partial}{\partial r_0} s(t_1) & \frac{\partial}{\partial s_0} s(t_1) & \frac{\partial}{\partial v_{r,0}} s(t_1) & \frac{\partial}{\partial v_{s,0}} s(t_1) & \frac{\partial}{\partial a_1} s(t_1) & \frac{\partial}{\partial a_2} s(t_1) \\ \vdots & \vdots & \vdots & \vdots & \vdots & \vdots \\ \frac{\partial}{\partial r_0} s(t_m) & \frac{\partial}{\partial s_0} s(t_m) & \frac{\partial}{\partial v_{r,0}} s(t_m) & \frac{\partial}{\partial v_{s,0}} s(t_m) & \frac{\partial}{\partial a_1} s(t_m) & \frac{\partial}{\partial a_2} s(t_m) \end{bmatrix} \tag{2.15}$$

Both H_1 and H_2 have in common the sensitivities of the measurements to the spacecraft's initial position and velocity. These sensitivities can be determined from linear orbit theory

[66] and are

$$\frac{\partial}{\partial r_0} r(t) \approx 4 - 3\cos(nt) \tag{2.16}$$

$$\frac{\partial}{\partial s_0} r(t) \approx 0 \tag{2.17}$$

$$\frac{\partial}{\partial v_{r,0}} r(t) \approx \frac{1}{n}\sin(nt) \tag{2.18}$$

$$\frac{\partial}{\partial v_{s,0}} r(t) \approx \frac{2}{n}(1 - \cos(nt)) \tag{2.19}$$

in the radial direction, and

$$\frac{\partial}{\partial r_0} s(t) \approx 6(\sin(nt) - nt) \tag{2.20}$$

$$\frac{\partial}{\partial s_0} s(t) \approx 1 \tag{2.21}$$

$$\frac{\partial}{\partial v_{r,0}} s(t) \approx \frac{2}{n}(\cos(nt) - 1) \tag{2.22}$$

$$\frac{\partial}{\partial v_{s,0}} s(t) \approx \frac{1}{n}(4\sin(nt) - 3nt) \tag{2.23}$$

in the along-track direction where n is the frequency of the spacecraft's orbit. The primary focus of this chapter will be on deriving the sensitivities of the radial and along-track positions of the spacecraft with respect to along-track accelerations, a_p in the one-acceleration case and a_1 and a_2 in the two-acceleration case. For the derivation, sensitivities of the spacecraft's radial and angular position within an orbital plane will be derived. Small changes in the along-track position of the spacecraft can be related to small changes in the angular position of the spacecraft through

$$\Delta s(t) = r(t)\Delta\theta(t) = (r_0 + \Delta r(t))\Delta\theta(t) \approx r_0 \Delta\theta(t) \tag{2.24}$$

which provides a relation in the sensitivities with respect to a generic acceleration, a, of

$$\frac{\partial}{\partial a} s(t) \approx r_0 \frac{\partial}{\partial a}\theta(t) \tag{2.25}$$

2.7.1 One Acceleration

The specific energy of a spacecraft's orbit, ϵ, is given by

$$\epsilon = \frac{1}{2}v^2 - \frac{\mu}{r} \tag{2.26}$$

where v is the speed of the spacecraft, μ is the gravitational parameter of the central body, and r is the radial position of the spacecraft. Assuming that the orbit is circular, then the specific energy can be written as a function of only the orbital radius as

$$\epsilon = -\frac{1}{2}\frac{\mu}{r} \tag{2.27}$$

The time derivative of the specific energy, the specific power, is therefore

$$\frac{d\epsilon}{dt} = \frac{1}{2}\frac{\mu}{r^2}\frac{dr}{dt} \tag{2.28}$$

If the spacecraft carries a propulsion system that produces a constant propulsive acceleration, a_{p}, and assuming that the propulsive acceleration is aligned with the spacecraft's velocity vector, then the specific power input to the spacecraft's orbit from the propulsion system is given by

$$p_{\mathrm{p}} = a_{\mathrm{p}}v = a_{\mathrm{p}}\sqrt{\frac{\mu}{r}} \tag{2.29}$$

Assuming that the only power input to the spacecraft's orbit comes from its propulsion system, then Eqs. 2.28 and 2.29 can be equated to give

$$\frac{1}{2}\frac{\mu}{r^2}\frac{dr}{dt} = a_{\mathrm{p}}\sqrt{\frac{\mu}{r}} \tag{2.30}$$

which can be rearranged to give an ordinary differential equation for the orbital radius

$$\frac{dr}{dt} = \frac{2a_{\mathrm{p}}}{\sqrt{\mu}}r^{3/2} \tag{2.31}$$

This differential equation can be analytically integrated to give an approximation for the orbital radius as a function of time

$$r(t) = \frac{r_0}{\left(1 - \frac{a_\mathrm{p}}{v_0} t\right)^2} \tag{2.32}$$

where r_0 is the initial orbital radius and v_0 is the initial orbital speed

$$v_0 = \sqrt{\frac{\mu}{r_0}} \tag{2.33}$$

From the approximation of the spacecraft's radial position over time, the angular position of the spacecraft in the orbital plane can also be approximated

$$\begin{aligned} \theta(t) &= \theta_0 + \int_0^t \sqrt{\frac{\mu}{r^3(\tau)}} d\tau && (2.34) \\ &= \theta_0 + \frac{1}{4} \frac{v_0^2}{a_\mathrm{p} r_0} \left[1 - \left(1 - \frac{a_\mathrm{p}}{v_0} t\right)^4\right] && (2.35) \end{aligned}$$

The approximation of the spacecraft's position within the orbital plane above is well known and has been presented previously [50]. Given a particular maneuver time, T, and an initial and final radius of the spacecraft, r_0 and r_f, the propulsive acceleration can be approximated by inverting Eq. 2.32.

$$a_\mathrm{p} \approx \frac{1}{T} \left(\sqrt{\frac{\mu}{r_0}} - \sqrt{\frac{\mu}{r_f}}\right) \tag{2.36}$$

As mentioned previously, this approach was taken during the SERT-2 mission [51]. However, the approximation was derived under the assumption that the gravitational field of the Earth can be approximate as that of a point mass. While this limitation may not be significant for high-altitude orbits with long maneuver durations, it will certainly be significant for low-altitude orbits with shorter maneuver durations. In the case of SERT-2, the spacecraft had an orbital altitude of 1,000 km and maneuver durations of several months which allowed for application of the analytical approximation [67]. However, for scenarios such as that of Figure 2-5, the oscillations of the spacecraft's radial position due to the non-spherical nature of the Earth's gravitational field are quite apparent. It is unclear what the initial and final radii of the spacecraft are, and the magnitude of the oscillations dominate any change in the spacecraft's radial position due to the propulsive acceleration.

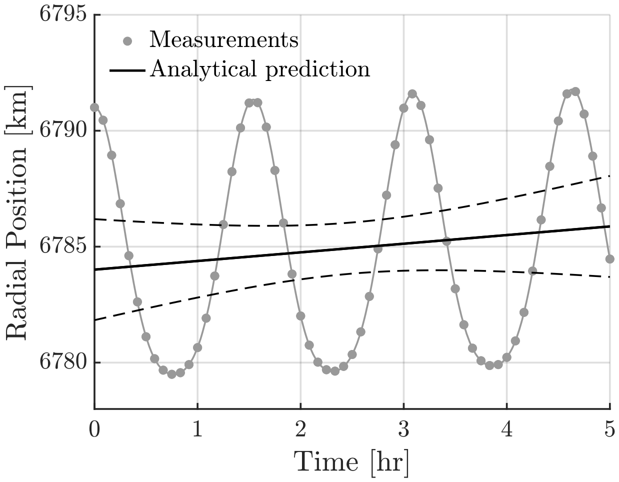

Figure 2-14: Radial position of the spacecraft during an orbit-raising maneuver along with curve fit of the analytical approximation where the initial radius and propulsive acceleration are free parameters. Dashed lines show the 95% confidence interval of the fit.

One possible approach for using the analytical approximation on low-altitude and short-duration maneuvers would be to fit Eq. 2.32 to the obtained data with the initial radius and propulsive acceleration as the free parameters. Figure 2-14 shows this approach for a 5-hour maneuver with measurements taken every five minutes. Since Eq 2.32 only accounts for a single acceleration, atmospheric drag was not simulated for this case and the propulsion system thrust was 100 μN acting on a 4 kg spacecraft. The solid black line shows the mean of the fit and the dashed lines show the 95% confidence interval. Looking solely at the estimated thrust, the mean estimated value was 233.87 μN with a 95% confidence interval of [-237.78 μN, 705.52 μN]. Comparatively, an ensemble Kalman update can provide a far better estimate. Modifying the forward model and parameter vector to not account for atmospheric drag, Figure 2-15 shows the resulting posterior marginal distribution of the thrust estimate. The mean of the distribution is 100.72 μN with a 95% confidence interval of [98.52 μN, 102.93 μN].

While the analytical approximation in its original form may not be useful for thrust estimation in low-Earth orbit, the sensitivities of the spacecraft's position with respect to the propulsive acceleration are still valuable. The partial derivative of the radial position with respective to the propulsive acceleration is

$$\frac{\partial}{\partial a_{\mathrm{p}}} r(t) \approx \frac{2 r_0 t}{v_0} \left(1 - \frac{a_{\mathrm{p}}}{v_0} t\right)^{-3} \tag{2.37}$$

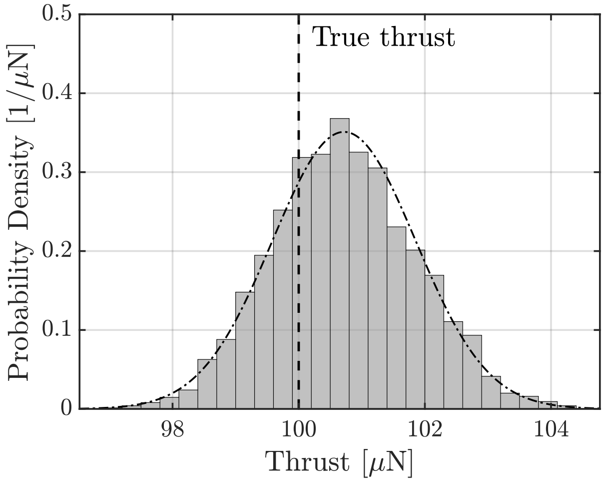

Figure 2-15: Inferred marginal probability distribution for the propulsive thrust in the one-acceleration case.

Typical parameters are $a_{\mathrm{p}} = 25\ \mu\mathrm{m/s}^2$, $t = 10$ hr, and $v_0 = 7.4$ km/s which gives

$$\frac{a_{\mathrm{p}}}{v_0}t = 1.2 \times 10^{-4} \tag{2.38}$$

and

$$\left(1 - \frac{a_{\mathrm{p}}}{v_0}t\right)^{-3} = 0.9996 \tag{2.39}$$

which allows for the sensitivity of the radial position with respect to the propulsive acceleration to be approximated as

$$\frac{\partial}{\partial a_{\mathrm{p}}} r(t) \approx 2\frac{r_0 t}{v_0} \tag{2.40}$$

using the assumption that $a_{\mathrm{p}}t/v_0 \ll 1$. For determining the sensitivity of the angular position with respect to the propulsive acceleration, start by expanding Eq. 2.35 to

$$\theta(t) \approx \theta_0 + \frac{1}{4}\frac{v_0^2}{r_0}\left[\frac{4t}{v_0} - \frac{6a_{\mathrm{p}}t^2}{v_0^2} + \frac{4a_{\mathrm{p}}^2t^3}{v_0^3} - \frac{a_{\mathrm{p}}^3t^4}{v_0^4}\right] \tag{2.41}$$

The sensitivity of the angular position with propulsive acceleration can be determined from

$$\frac{\partial}{\partial a_{\mathrm{p}}}\theta(t) \approx \frac{1}{4r_0}\left[-6t^2 + 8t^2\left(\frac{a_{\mathrm{p}}}{v_0}t\right) - 3t^2\left(\frac{a_{\mathrm{p}}}{v_0}t\right)^2\right] \tag{2.42}$$

Under the assumption that $a_\mathrm{p} t/v_0 \ll 1$ then

$$\frac{\partial}{\partial a_\mathrm{p}}\theta(t) \approx -\frac{3}{2}\frac{t^2}{r_0} \tag{2.43}$$

Figure 2-16 shows the relationship between discrete changes in the spacecraft's position within the orbital plane versus discrete changes in the propulsive acceleration. The changes in the spacecraft's position are normalized by the sensitivities in Eqs. 2.40 and 2.43 and random parameters for the propulsive acceleration, time, and initial orbital radius were used. In both of the plots the data closely follows a line of slope one, indicating that the sensitivities in Eqs. 2.40 and 2.43 well-predict the actual sensitivities of the spacecraft's position in the orbital plane with respect to the propulsive acceleration.

2.7.2 Two Accelerations

The sensitivities for a single acceleration may be useful for high-altitude orbits, such as that of SERT-2, where the affect of atmospheric drag is negligible. However, in low-altitude orbits there are two significant accelerations that act on the spacecraft: the propulsive acceleration and atmospheric drag. Conveniently, both of these accelerations act roughly in the along-track direction for a near-circular orbit.

In deriving the linear measurement model when both propulsive acceleration and atmospheric drag act on the spacecraft, a general case where two along-track accelerations, a_1 and a_2, act on the spacecraft is considered. It is also assumed that a_1 only acts on the spacecraft for $t < T_s$ where T_s is a switching time, and that a_2 acts on the spacecraft for all time. Physically, a_1 would represent the propulsive acceleration and a_2 would represent the atmospheric drag. The total acceleration acting on the spacecraft is then

$$a(t) = \begin{cases} a_1 + a_2 & t < T_s \\ a_2 & t \geq T_s \end{cases} \tag{2.44}$$

The approach for analyzing this scenario is to consider two segments based on if the time is before or after the switching time, T_s. When $t < T_s$, the scenario is indistinguishable from the one-acceleration case, but with $a_\mathrm{p} = a_1 + a_2$. Therefore, the radial position of the

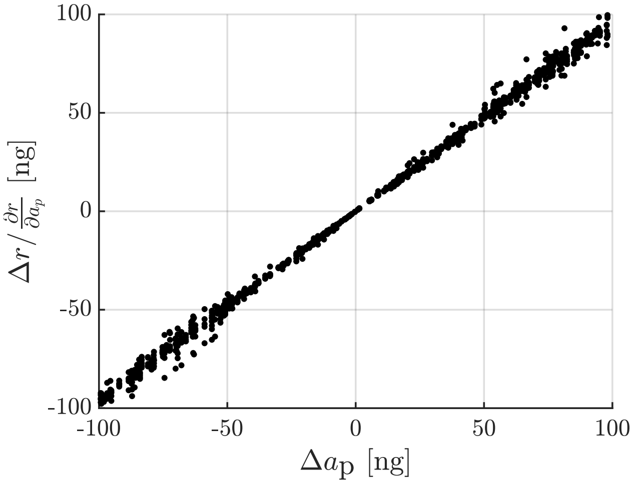

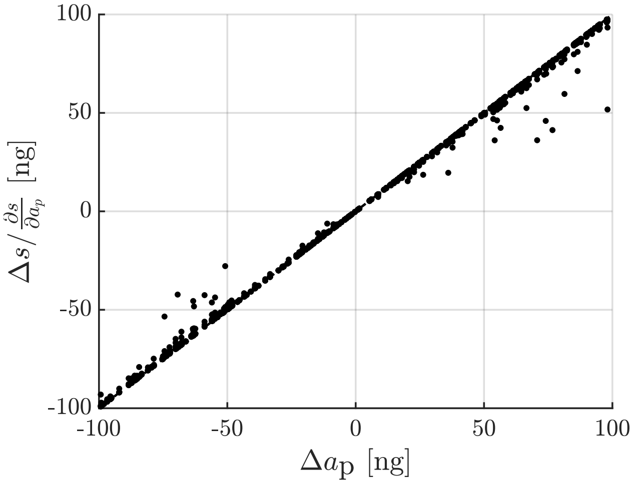

Figure 2-16: Relationship between discrete changes in the spacecraft's position within the orbital plane versus discrete changes in the propulsive acceleration for a single acceleration acting on the spacecraft. Top plot shows the radial position while the bottom plot shows the along-track position.

spacecraft can be approximated from

$$r_1(t) \approx \frac{r_0}{\left(1 - \frac{a_1+a_2}{v_0}t\right)^2} \tag{2.45}$$

and the sensitivity of the radial position with respect to both a_1 and a_2 is given by

$$\frac{\partial}{\partial a_1} r_1(t) = \frac{\partial}{\partial a_2} r_1(t) = \frac{2r_0 t}{v_0}\left(1 - \frac{a_1 + a_2}{v_0}t\right)^{-3} \tag{2.46}$$

Under the assumption that $a_1 t/v_0 \ll 1$ and $a_2 t/v_0 \ll 1$ then

$$\frac{\partial}{\partial a_1} r_1(t) \approx \frac{\partial}{\partial a_2} r_1(t) \approx \frac{2r_0 t}{v_0} \tag{2.47}$$

When $t \geq T_s$ then a new approximation for the radial position of the spacecraft is required. Under the assumption that the spacecraft is still in a near-circular orbit at $t = T_s$, then the radial position for $t \geq T_s$ can be approximated by

$$r_2(t) \approx \frac{r'_0}{\left(1 - \frac{a_2}{v'_0}(t - T_s)\right)^2} \tag{2.48}$$

where the initial radial position, r'_0, is given by the radial position of the spacecraft at the end of the first segment

$$r'_0 = r_1(T_s) = \frac{r_0}{\left(1 - \frac{a_1+a_2}{v_0}T_s\right)^2} \tag{2.49}$$

as is the initial orbital speed

$$v'_0 = \sqrt{\frac{\mu}{r'_0}} = \sqrt{\frac{\mu}{r_0}}\left(1 - \frac{a_1 + a_2}{v_0}T_s\right) \tag{2.50}$$

Substituting Eqs. 2.49 and 2.50 into Eq. 2.48 gives

$$r_2(t) \approx \frac{r_0}{\left(1 - \frac{a_1+a_2}{v_0}T_s - \frac{a_2}{v_0}(t - T_s)\right)^2} \tag{2.51}$$

The sensitivity of the spacecraft's radial position with respect to a_1 is then

$$\frac{\partial}{\partial a_1} r_2(t) \approx \frac{2r_0 T_s}{v_0} \left(1 - \frac{a_1 + a_2}{v_0} T_s - \frac{a_2}{v_0}(t - T_s)\right)^{-3} \tag{2.52}$$

Under the assumptions that $a_1 t/v_0 \ll 1$ and $a_2 t/v_0 \ll 1$ then

$$\frac{\partial}{\partial a_1} r_2(t) \approx \frac{2r_0 T_s}{v_0} \tag{2.53}$$

The sensitivity of the spacecraft's radial position with respect to a_2 is

$$\frac{\partial}{\partial a_2} r_2(t) \approx \frac{2r_0 t}{v_0} \left(1 - \frac{a_1 + a_2}{v_0} T_s - \frac{a_2}{v_0}(t - T_s)\right)^{-3} \tag{2.54}$$

Under the assumptions that $a_1 t/v_0 \ll 1$ and $a_2 t/v_0 \ll 1$ then

$$\frac{\partial}{\partial a_2} r_2(t) \approx \frac{2r_0 t}{v_0} \tag{2.55}$$

The same approach can be taken for the angular position of the spacecraft in the orbital plane. For $t < T_s$, the scenario is the same as the one-acceleration case with $a_{\mathrm{p}} = a_1 + a_2$, so the angular position of the spacecraft can be approximated from

$$\theta_1(t) \approx \theta_0 + \frac{1}{4} \frac{v_0^2}{r_0(a_1 + a_2)} \left[1 - \left(1 - \frac{a_1 + a_2}{v_0} t\right)^4\right] \tag{2.56}$$

and the sensitivities of $\theta_1(t)$ with respect to a_1 and a_2 are given by

$$\frac{\partial}{\partial a_1} \theta_1(t) \approx \frac{1}{4r_0} \left[-6t^2 + 8t^2 \left(\frac{a_1}{v_0} t\right) - 3t^2 \left(\frac{a_1}{v_0} t\right)^2\right] \tag{2.57}$$

and

$$\frac{\partial}{\partial a_2} \theta_1(t) \approx \frac{1}{4r_0} \left[-6t^2 + 8t^2 \left(\frac{a_2}{v_0} t\right) - 3t^2 \left(\frac{a_2}{v_0} t\right)^2\right] \tag{2.58}$$

Under the assumptions that $a_1 t/v_0 \ll 1$ and $a_2 t/v_0 \ll 1$ then

$$\frac{\partial}{\partial a_1} \theta_1(t) \approx \frac{\partial}{\partial a_2} \theta_1(t) \approx -\frac{3}{2} \frac{t^2}{r_0} \tag{2.59}$$

When $t \geq T_s$ the angular position can be approximated through integration

$$\theta_2(t) \approx \theta_0' + \int_0^t \sqrt{\frac{\mu}{r_2^3(\tau)}} d\tau \tag{2.60}$$

$$\approx \theta_0' + \frac{1}{4}\frac{v_0^2}{r_0 a_2}\left[\left(1 - \frac{a_1 + a_2}{v_0}T_s\right)^4 - \left(1 - \frac{a_1 + a_2}{v_0}T_s - \frac{a_2}{v_0}(t - T_s)\right)^4\right] \tag{2.61}$$

where the initial angular position, θ_0', is given by the angular position of the spacecraft at the end of the first segment

$$\theta_0' = \theta_1(T_s) = \theta_0 + \frac{1}{4}\frac{v_0^2}{r_0(a_1 + a_2)}\left[1 - \left(1 - \frac{a_1 + a_2}{v_0}T_s\right)^4\right] \tag{2.62}$$

Substituting Eq. 2.62 into Eq. 2.61 gives

$$\begin{aligned}\theta_2(t) \approx \theta_0 &+ \frac{1}{4}\frac{v_0^2}{r_0(a_1 + a_2)}\left[1 - \left(1 - \frac{a_1 + a_2}{v_0}T_s\right)^4\right] \\ &+ \frac{1}{4}\frac{v_0^2}{r_0 a_2}\left[\left(1 - \frac{a_1 + a_2}{v_0}T_s\right)^4 - \left(1 - \frac{a_1 + a_2}{v_0}T_s - \frac{a_2}{v_0}(t - T_s)\right)^4\right]\end{aligned} \tag{2.63}$$

In order to determine the sensitivity of the angular position for $t \geq T_s$, first define

$$\Gamma_1(t) = \frac{1}{4}\frac{v_0^2}{r_0(a_1 + a_2)}\left[1 - \left(1 - \frac{a_1 + a_2}{v_0}T_s\right)^4\right] \tag{2.64}$$

and

$$\Gamma_2(t) = \frac{1}{4}\frac{v_0^2}{r_0 a_2}\left[\left(1 - \frac{a_1 + a_2}{v_0}T_s\right)^4 - \left(1 - \frac{a_1 + a_2}{v_0}T_s - \frac{a_2}{v_0}(t - T_s)\right)^4\right] \tag{2.65}$$

such that $\theta_2(t) \approx \theta_0 + \Gamma_1(t) + \Gamma_2(t)$. Expanding $\Gamma_1(t)$ gives

$$\Gamma_1(t) = \frac{1}{4}\frac{v_0}{r_0}\left[4T_s - \frac{6(a_1 + a_2)T_s^2}{v_0} + \frac{4(a_1 + a_2)^2 T_s^3}{v_0^2} - \frac{(a_1 + a_2)^3 T_s^4}{v_0^3}\right] \tag{2.66}$$

which allows for the sensitivity of $\Gamma_1(t)$ with respect to a_1 to be calculated as

$$\frac{\partial}{\partial a_1}\Gamma_1(t) = \frac{1}{4}\frac{T_s^2}{r_0}\left[-6 + \frac{8(a_1 + a_2)T_s}{v_0} - \frac{3(a_1 + a_2)^2 T_s^2}{v_0^2}\right] \tag{2.67}$$

Under the assumption that $(a_1 + a_2)T_s/v_0 \ll 1$ then

$$\frac{\partial}{\partial a_1}\Gamma_1(t) \approx -\frac{3}{2}\frac{T_s^2}{r_0} \tag{2.68}$$

Similarly, the sensitivity of $\Gamma_1(t)$ with respect to a_2 is given by

$$\frac{\partial}{\partial a_2}\Gamma_1(t) = \frac{1}{4}\frac{T_s^2}{r_0}\left[-6 + \frac{8(a_1 + a_2)T_s}{v_0} - \frac{3(a_1 + a_2)^2 T_s^2}{v_0^2}\right] \tag{2.69}$$

Under the assumption that $(a_1 + a_2)T_s/v_0 \ll 1$ then

$$\frac{\partial}{\partial a_2}\Gamma_1(t) \approx -\frac{3}{2}\frac{T_s^2}{r_0} \tag{2.70}$$

In order to analyze the sensitivities of $\Gamma_2(t)$ define

$$\Lambda = 1 - \frac{a_1 + a_2}{v_0}T_s \tag{2.71}$$

such that

$$\Gamma_2(t) = \frac{1}{4}\frac{v_0}{r_0}(t - T_s)\left[4\Lambda^3 - 6\Lambda^2\frac{a_2(t - T_s)}{v_0} + 4\Lambda\frac{a_2^2(t - T_s)^2}{v_0^2} - \frac{a_2^3(t - T_s)^3}{v_0^3}\right] \tag{2.72}$$

Since $\Gamma_2(t)$ does not directly depend on a_1 the sensitivity of $\Gamma_2(t)$ with respect to a_1 can be calculated from

$$\frac{\partial}{\partial a_1}\Gamma_2(t) = \frac{\partial}{\partial \Lambda}\Gamma_2(t) \cdot \frac{\partial}{\partial a_1}\Lambda \tag{2.73}$$

$$= \left(-\frac{T_s}{v_0}\right)\frac{\partial}{\partial \Lambda}\Gamma_2(t) \tag{2.74}$$

$$= -\frac{T_s(t - T_s)}{r_0}\left[3\Lambda^2 - 3\Lambda\frac{a_2(t - T_s)}{v_0} + \frac{a_2^2(t - T_s)^2}{v_0^2}\right] \tag{2.75}$$

Under the assumptions that $(a_1 + a_2)T_s/v_0 \ll 1$ and $a_2(t - T_s)/v_0 \ll 1$ then $\Lambda \approx 1$ and

$$\frac{\partial}{\partial a_1}\Gamma_2(t) \approx -3\frac{T_s(t - T_s)}{r_0} \tag{2.76}$$

The sensitivity of $\Gamma_2(t)$ with respect to a_2 is given by

$$\frac{\partial}{\partial a_2}\Gamma_2(t) = \frac{1}{4}\frac{v_0}{r_0}(t-T_s)\left[12\Lambda^2\frac{\partial}{\partial a_2}\Lambda - 6\Lambda^2\frac{t-T_s}{v_0} - 12\Lambda\frac{a_2(t-T_s)}{v_0}\frac{\partial}{\partial a_2}\Lambda + 8\Lambda\frac{a_2(t-T_s)^2}{v_0^2}\right.$$
$$\left. +4\frac{a_2^2(t-T_s)^2}{v_0^2}\frac{\partial}{\partial a_2}\Lambda - 3\frac{a_2^2(t-T_s)^3}{v_0^3}\right] \tag{2.77}$$

Substituting in

$$\frac{\partial}{\partial a_2}\Lambda = -\frac{T_s}{v_0} \tag{2.78}$$

then

$$\frac{\partial}{\partial a_2}\Gamma_2(t) = \frac{1}{4}\frac{v_0}{r_0}(t-T_s)\left[-6\Lambda^2\frac{(t+T_s)}{v_0} + 4\Lambda\frac{a_2(t-T_s)(2t+T_s)}{v_0^2}\right.$$
$$\left. -\frac{a_2^2(t-T_s)^2(3t+T_s)}{v_0^3}\right] \tag{2.79}$$

Under the assumption that $(a_1+a_2)T_s/v_0 \ll 1$ which gives $\Lambda \approx 1$, note that all of the terms inside the brackets can be written as

$$k\frac{(nt+T_s)}{v_0}\left[\frac{a_2(t-T_s)}{v_0}\right]^n; \qquad n \in \{0,1,2\} \tag{2.80}$$

where k is some constant value independent of a_2, v_0, t, and T_s. Under the assumption that $a_2(t-T_s)/v_0 \ll 1$ then the dominant term will be that with $n=0$. Therefore

$$\frac{\partial}{\partial a_2}\Gamma_2(t) \approx \frac{1}{4}\frac{v_0}{r_0}(t-T_s)\left[-6\Lambda^2\frac{(t+T_s)}{v_0}\right] \tag{2.81}$$

$$\approx -\frac{3}{2}\frac{t^2}{r_0} + \frac{3}{2}\frac{T_s^2}{r_0} \tag{2.82}$$

Combining all of this information together then the sensitivities of the spacecraft's angular position with respect to a_1 and a_2 for $t \geq T_s$ are given by

$$\frac{\partial}{\partial a_1}\theta_2(t) = \frac{\partial}{\partial a_1}\Gamma_1(t) + \frac{\partial}{\partial a_1}\Gamma_2(t) \tag{2.83}$$

$$\approx -\frac{3T_s}{r_0}\left(t - \frac{1}{2}T_s\right) \tag{2.84}$$

and

$$\frac{\partial}{\partial a_2}\theta_2(t) = \frac{\partial}{\partial a_2}\Gamma_1(t) + \frac{\partial}{\partial a_2}\Gamma_2(t) \tag{2.85}$$

$$\approx -\frac{3}{2}\frac{t^2}{r_0} \tag{2.86}$$

The sensitivities of the spacecraft's radial position at any time with respect to a_1 and a_2 are given by

$$\frac{\partial}{\partial a_1}r(t) \approx \begin{cases} \frac{2r_0 t}{v_0} & t < T_s \\ \frac{2r_0 T_s}{v_0} & t \geq T_s \end{cases} \tag{2.87}$$

and

$$\frac{\partial}{\partial a_2}r(t) \approx \frac{2r_0 t}{v_0} \quad \forall\ t \tag{2.88}$$

while the sensitivities of the spacecraft's along-track position at any time with respect to a_1 and a_2 are given by

$$\frac{\partial}{\partial a_1}s(t) \approx \begin{cases} -\frac{3}{2}t^2 & t < T_s \\ -3T_s\left(t - \frac{1}{2}T_s\right) & t \geq T_s \end{cases} \tag{2.89}$$

and

$$\frac{\partial}{\partial a_2}s(t) \approx -\frac{3}{2}t^2 \quad \forall\ t \tag{2.90}$$

Again, the relation

$$\frac{\partial}{\partial a_{1/2}}s(t) \approx r_0\frac{\partial}{\partial a_{1/2}}\theta(t) \tag{2.91}$$

is used. Figures 2-17 and 2-18 show the relationship between discrete changes in the spacecraft's position within the orbital plane versus discrete changes in a_1 and a_2 respectively. The changes in the spacecraft's position are normalized by their sensitivities in Eqs. 2.87 through 2.90 and random parameters for a_1, a_2, time, and initial orbital radius were used. In all of the plots, the data closely follows a line of slope one, indicating that the sensitivities in Eqs. 2.87 through 2.90 well-predict the actual sensitivities of the spacecraft's position in the orbital plane with respect to both a_1 and a_2.

2.7.3 Explanations for Numerical Trends

With the sensitivities of the spacecraft's position in the orbital plane with respect to the propulsive and atmospheric drag accelerations derived, potential explanations for some of the trends observed in the results of Section 2.6 can be provided. Here, the focus is on the two-acceleration case, and specifically on the sensitivities of the spacecraft's radial and along-track position in the orbital plane with respect to a_1, which was used to represent the propulsive acceleration.

The first trend to consider is from Figure 2-10 which shows that the posterior standard deviation of the distribution for the propulsive acceleration is independent of the true acceleration value. When inferring a distribution for the propulsive acceleration, the variance in the distribution will be determined based on the variance in the spacecraft's position from uncertainty in the inference parameters, modeling error, and measurement noise. Both the modeling error and measurement noise are independent of the acceleration value, and from Eqs. 2.87 and 2.89 it can be seen that any changes in the spacecraft's position due to changes in the propulsive acceleration are also independent of the acceleration value. Therefore, it is unsurprising that the posterior standard deviation of the distribution for the propulsive acceleration is independent of the true acceleration value; the observed variance in spacecraft position does not contain any information about the actual acceleration.

Trends of the standard deviation with maneuver duration and measurement interval are more difficult to intuitively explain due to the effect of modeling error. However, in the case where modeling error is not included, such as in Figure 2-13, potential explanations can be provided. The dependences of the sensitivities in Eqs. 2.87 and 2.89 with time indicate that the relative importance of the radial and along-track position will depend on measurement times. Since the sensitivity of the radial position scales linearly with time and the sensitivity of the along-track position scales quadratically with time, the sensitivity of the radial position dominate for shorter times (less than an orbital period) while the sensitivity of the along-track position will dominate for longer times. When each variable is dominant, the convergence of the posterior standard deviation should scale at a similar rate with maneuver duration. This is apparent in Figure 2-13 where the standard deviation scales

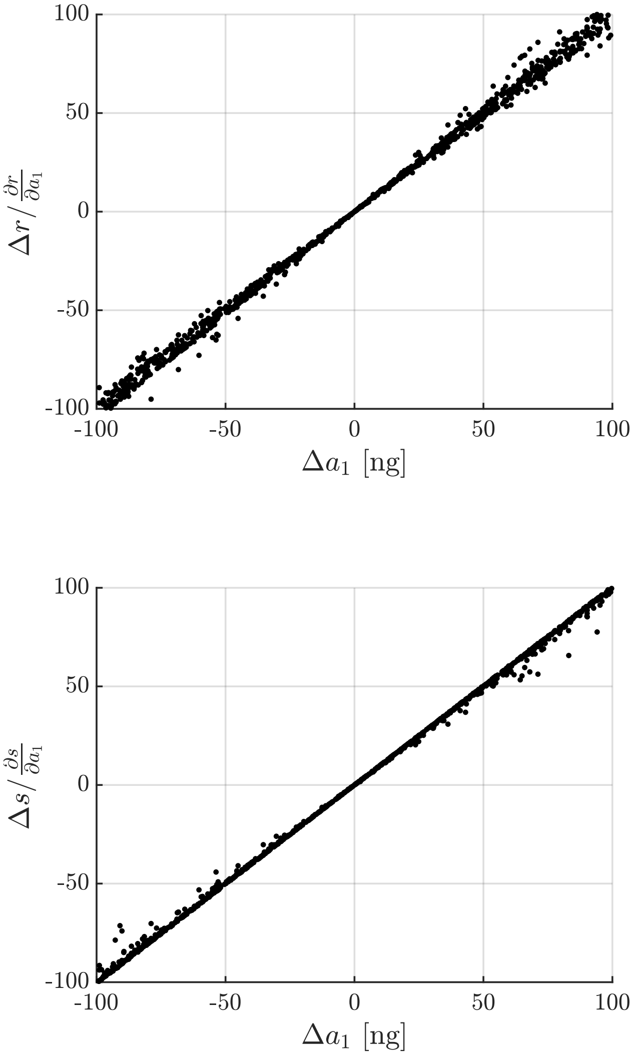

Figure 2-17: Relationship between discrete changes in the spacecraft's position within the orbital plane versus discrete changes in a_1. Top plot shows the radial position while the bottom plot shows the along-track position.

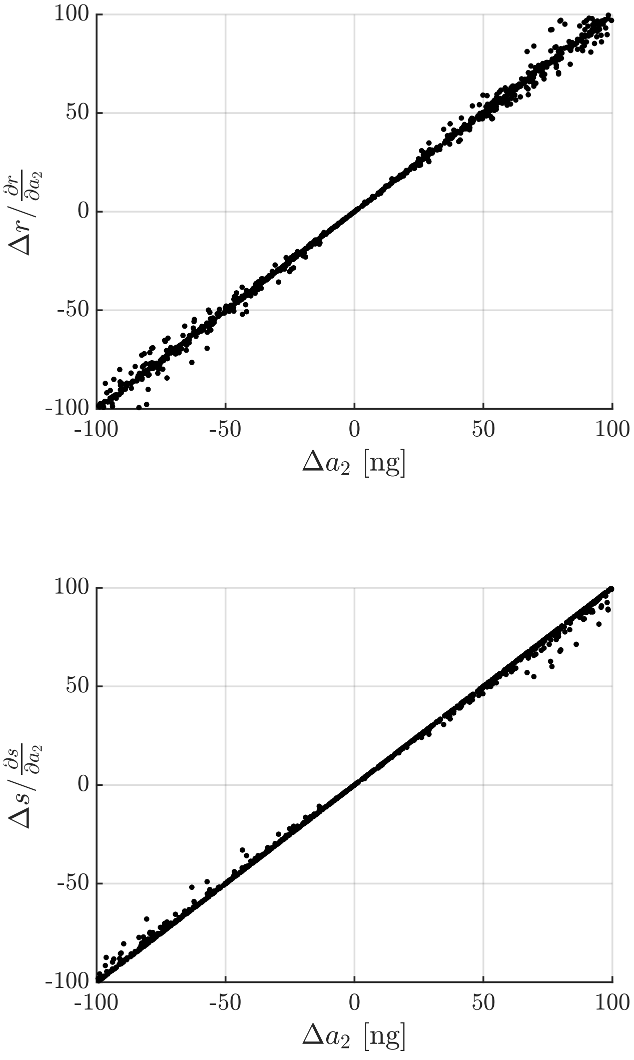

Figure 2-18: Relationship between discrete changes in the spacecraft's position within the orbital plane versus discrete changes in a_2. Top plot shows the radial position while the bottom plot shows the along-track position.

linearly for shorter maneuver durations and quadratically for longer maneuver durations.

Finally, the trend in posterior standard deviation with measurement interval can be explained from the likelihood probability. Since the measurement noise is assumed to be Gaussian, the likelihood probability in Eq. 2.2 is simply a product of many Gaussian probability densities, one for each state variable in each measurement. The product of N Gaussian probability densities is also Gaussian with standard deviation given by

$$\frac{1}{\sigma^2} = \sum_{i=1}^{N} \frac{1}{\sigma_i^2} \tag{2.92}$$

where σ_i is the standard deviation for the i^{th} probability density. For a maneuver with M measurement locations, M measurements for the spacecraft position along each axis are taken for a total of $3M$ measurements. The standard deviation of the likelihood probability density can then be calculated according to

$$\frac{1}{\sigma_L^2} = \sum_{i=1}^{3M} \frac{1}{\sigma_p^2} \tag{2.93}$$

where σ_p is the standard deviation of the measurement noise in position. Rearranging to solve for σ_L gives

$$\sigma_L = \frac{1}{\sqrt{3M}} \sigma_p \tag{2.94}$$

For a given maneuver length, increasing the measurement interval, Δt, will cause a proportional decrease in the number of measurements, which in turn will result in an increase of the standard deviation of the posterior distribution that scales with $\sqrt{\Delta t}$.

The introduction of modeling error will alter the expected trends of the standard deviation with maneuver duration and measurement interval discussed above. The modeling error causes an inflation of the measurement noise that increase with time, which likely is responsible for the observed reduction in convergence of the standard deviation with maneuver duration from quadratic to $T^{-0.8}$. In addition, the increase in measurement noise due to modeling error will be strongly correlated between different points in time. The strong correlation means that the introduction of additional measurement locations, through reducing the measurement interval, does not provide as much additional information as it did when modeling error was not included. This may be the cause of the negligible dependence of the posterior standard deviation with measurement interval observed in Figure 2-12. More rigorous explanations for the observed trends when modeling error is included are beyond the scope of this thesis, but may be explored in future work.

2.7.4 Numerical Comparison

With the sensitivity matrix relating small changes in the input parameters to small changes in the measurements derived, the Kalman gain can be analytically calculated from

$$K = PH^T \left(HPH^T + R\right)^{-1} \tag{2.95}$$

where P is the initial covariance of the input parameters and R is the covariance of the measurement noise. Given the Kalman gain, the change in the covariance of the input parameters after conditioning with the observed measurements can be predicted as

$$P = (I - KH)P \tag{2.96}$$

Figure 2-19 shows a comparison of numerical (through the ensemble Kalman update) and analytical predictions of the posterior standard deviation of the propulsive acceleration versus maneuver duration for an orbital altitude of 412 km. Importantly, no modeling error is considered in this initial comparison. In all cases the maneuver duration is split evenly in half with the propulsion system active for the first half of the maneuver and inactive for the second half of the maneuver. Measurements are taken at a constant interval with a total of 50 measurement locations throughout the maneuver duration. For the prior parameter covariance, the parameters are assumed to be independent with prior variance in the initial positions of $(3.33 \text{ m})^2$, prior variance in the initial velocities of $(33.3 \text{ mm/s})^2$, and prior variance in both accelerations of $(100 \text{ ng})^2$. Measurement noise is assumed to be independent for each measurement with variance of $(3.33 \text{ m})^2$. The numerical and analytical predictions align quite well except for a region close to a maneuver duration of 1.5 hours. This maneuver duration happens to correspond to the orbital period of the spacecraft, and may cause the observed discrepancy. Future work will be required in order to explore the cause of the discrepancy.

While 2.96 provides reliable predictions for the posterior standard deviation of the

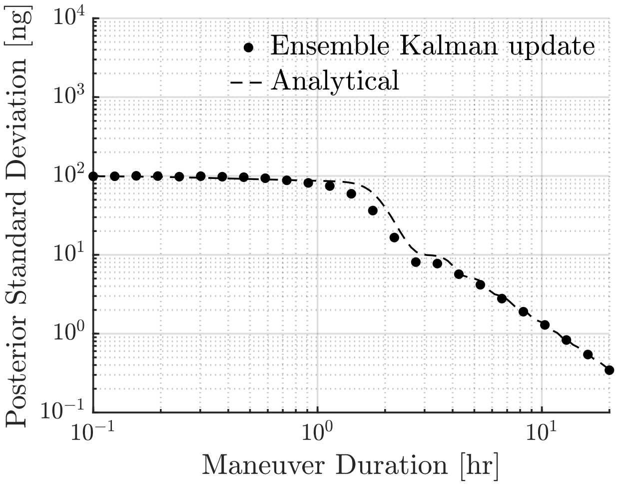

Figure 2-19: Comparison between the ensemble Kalman update prediction and analytical prediction of the marginal posterior standard deviation of the propulsive acceleration versus maneuver duration.

propulsive acceleration when there is no modeling error, it requires modification in order to make comparisons to the results seen in Section 2.6 where there is modeling error. In order to account for modeling error, first separate the measurement noise, ν, into two terms

$$\nu = \nu_{\text{modeling error}} + \nu_{\text{sensor noise}} \tag{2.97}$$

where $\nu_{\text{modeling error}}$ corresponds to measurement noise caused by modeling error and $\nu_{\text{sensor noise}}$ corresponds to measurement noise caused by sensor noise. By performing this separation, the covariance of the measurement noise can also be separated into two terms, again corresponding to the modeling error and sensor noise

$$R = R_{\text{modeling error}} + R_{\text{sensor noise}} \tag{2.98}$$

In order to account for modeling error, $R_{\text{modeling error}}$ needs to be calculated. Unfortunately, a direct calculation of $R_{\text{modeling error}}$ could not be found. However, several methods for approximating $R_{\text{modeling error}}$ are possible. The method taken in this work is to generate samples of the change in the radial and along-track position of the spacecraft caused by the modeling error. With a method to generate samples, the covariance matrix can be approximated by generating samples of the radial and along-track position change at the desired measurement locations and calculating the covariance of the samples. Alternative methods such as directly generating a polynomial approximation of the covariance matrix were explored but were found to be less reliable.

In order to generate samples of the change in the spacecraft's position caused by the modeling error, two steps are taken. First, the modeling error is caused by the process noise which is represented as three Gaussian processes, one for each axis. As such, a parameterization of the Gaussian process along each axis is developed through a truncated Karhunen-Loève expansion

$$K(t) = \mu(t) + \sum_{i=1}^{P} \sqrt{\lambda_i} \beta_i(t) \xi_i \tag{2.99}$$

where $K(t)$ is the output of the Gaussian process, $\mu(t)$ is the mean of the Gaussian process over time, λ_i are the P largest eigenvalues of the covariance matrix for the Gaussian process, and β_i are the corresponding eigenvectors. ξ_i are standard-normal random variables which are used to obtain realizations of the Gaussian process; by generating samples of ξ_i, different realizations of the Gaussian process can be generated.

With a truncated Karhunen-Loève expansion for the Gaussian process along each axis, the process noise can be parameterized by $3P$ standard-normal random variables. The second step in generating samples of the change in the spacecraft's position is to develop a polynomial chaos expansion which relates the standard-normal input parameters for the Karhunen-Loève expansion to changes in the radial and along-track position of the spacecraft caused by the modeling error. The polynomial chaos expansions for each axis can be expressed as

$$\Delta r(t, \xi_1, \cdots, \xi_n) \approx \sum_{\vec{\alpha} \geq \vec{0}} C^r_{\vec{\alpha}}(t) \Psi_{\vec{\alpha}}(\xi_1, \cdots, \xi_{3P}) \tag{2.100}$$

$$\Delta s(t, \xi_1, \cdots, \xi_n) \approx \sum_{\vec{\alpha} \geq \vec{0}} C^s_{\vec{\alpha}}(t) \Psi_{\vec{\alpha}}(\xi_1, \cdots, \xi_{3P}) \tag{2.101}$$

where $\vec{\alpha}$ is a multi-index, C^r and C^s are matrices of coefficients, and $\Psi(\xi_1, \ldots, \xi_{3P})$ are the multi-dimensional basis functions. Since all of the input parameters are standard-normal, the mutli-dimensional basis functions are simply a product of Hermite polynomials, one for each input parameter

$$\Psi_{\vec{\alpha}}(\xi_1, \cdots, \xi_{3P}) = \prod_{i=1}^{3P} \mathrm{He}_{\vec{\alpha}_i}(\xi_i) \tag{2.102}$$

The final step in generating the polynomial chaos expansion is solving for the coefficients, C^r and C^s. The approach taken in this work is to calculate the coefficients through a least-squares fit of the multi-dimensional basis functions to randomly-sampled data. Specifically, assuming that there are N total multi-dimensional basis functions and m samples to the input parameters are generated, a Vandermonde matrix can be formed

$$V = \begin{bmatrix} \Psi_{\vec{\alpha}_1}(\xi_1^1, \cdots, \xi_n^1) & \dots & \Psi_{\vec{\alpha}_N}(\xi_1^1, \cdots, \xi_n^1) \\ \vdots & \ddots & \vdots \\ \Psi_{\vec{\alpha}_1}(\xi_1^m, \cdots, \xi_n^m) & \dots & \Psi_{\vec{\alpha}_N}(\xi_1^m, \cdots, \xi_n^m) \end{bmatrix} \tag{2.103}$$

where each row corresponds to a random sample of the input parameters and each column corresponds to one of the basis functions. The coefficients can then be solved from

$$C^r_{\vec{\alpha}}(t) \approx \left(V^T V\right)^{-1} V^T f_r(t) \tag{2.104}$$

$$C^s_{\vec{\alpha}}(t) \approx \left(V^T V\right)^{-1} V^T f_s(t) \tag{2.105}$$

where f_r and f_s correspond to the observed changes in the spacecraft's radial and along-track position for each set of the input parameters

$$f_r(t) = \begin{bmatrix} \Delta r_1(t) \\ \vdots \\ \Delta r_m(t) \end{bmatrix} \qquad \text{and} \qquad f_s(t) = \begin{bmatrix} \Delta s_1(t) \\ \vdots \\ \Delta s_m(t) \end{bmatrix} \tag{2.106}$$

Given the polynomial chaos expansions, $R_{\text{modeling error}}$ can be approximated by generating samples of the input parameters, $\xi_1, \ldots, \xi_{3P}$, which allows samples to be generated for the change in the spacecraft's radial and along-track position. Given the samples for the change in the spacecraft's radial and along-track position, $R_{\text{modeling error}}$ can be approximated by calculating the covariance of the generated samples. Figure 2-20 shows a comparison of a semi-analytical prediction of the posterior standard deviation in the propulsive acceleration versus maneuver duration using a polynomial chaos expansion to approximate

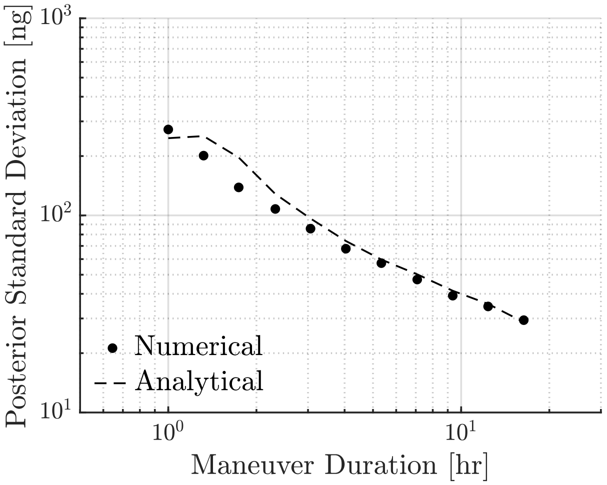

Figure 2-20: Comparison between the ensemble Kalman update prediction and analytical prediction of the marginal posterior standard deviation of the propulsive acceleration versus maneuver duration.

$R_{\text{modeling error}}$ and the data generated with an ensemble Kalman update in Figure 2-11. As in Figure 2-19, a discrepancy between the numerical and analytical predictions exists right around the orbital period of approximately 1.5 hours. However, for larger maneuver durations the semi-analytical approach provides a good prediction of the posterior standard deviation that would be obtained with the ensemble Kalman update.

2.8 Uncertainty Predictions

Given the ability to predict the posterior standard deviation of the propulsive acceleration with the analytically-derived linear measurement model and the semi-analytical approximation for $R_{\text{modeling error}}$ through a polynomial chaos expansion, rapid predictions for the posterior standard deviation can be made without the need for any numerical simulation. These predictions can be used to survey desired orbit and maneuver parameters during preliminary mission design in order to achieve a desired level of the posterior standard deviation. Figure 2-20 shows that the semi-analytical prediction closely matches a full numerical prediction with a slight discrepancy when the maneuver duration is close to the orbital period. Table 2.4 shows further comparisons between the numerical and analytical approaches for an orbital altitude of 400 km where the maneuver duration, measurement interval, and sensor noise are all varied. Again the numerical and analytical predictions agree quite closely,

Table 2.4: Comparison of numerical and analytical predictions of the posterior standard deviation in the propulsive acceleration for different maneuver parameters.

Firing Time [hr]	Measurement Interval [min]	3σ Sensor Noise [m]	1σ Acceleration Uncertainty		Diff. [%]
			Numerical [μm/s^2]	Analytical [μm/s^2]	
5	**10**	**100**	1.0076	1.0361	2.8
2	10	100	2.0836	2.3513	11.4
10	10	100	0.6640	0.6778	2.0
5	**5**	100	0.9840	1.0422	5.9
5	**20**	100	1.0294	1.0445	1.4
5	10	**10**	0.9426	0.9433	0.1
5	10	**1000**	1.7207	1.7691	2.8

except for when the maneuver duration is close to the orbital period.

Given that the numerical and analytical predictions of the posterior standard deviation agree quite well, the analytical predictions can be used to rapidly survey different types of maneuvers in order to provide an uncertainty map. Note from Eqs. 2.87 through 2.90 that the sensitivities of the spacecrafts radial and along-track position only depend on the orbital radius and various elements of time. Therefore, by picking an orbital radius the posterior standard deviation can be predicted for different values of the maneuver duration and measurement interval. Tables 2.5 and 2.6 show posterior standard deviation predictions for orbit altitudes of 410 km and 700 km respectively. These two orbit altitudes were selected in order to represent potential deployments either from the International Space Station and into a polar sun-synchronous orbit respectively, and provide a general guideline for the predicted posterior standard deviation. Once a particular firing time and measurement interval are selected, more-detailed analysis through numerical approaches can be used.

2.9 Measurement Timing Optimization

A final advantage of the analytical formulation for the linear measurement model is the ability to optimize the timing of measurements. In all the previous results, the measurements were assumed to be taken at a constant measurement interval. However, a constant measurement interval may not be the optimal measurement timing in terms of minimizing the posterior uncertainty in the propulsive acceleration. This section provides an initial analysis of minimizing the posterior uncertainty in the propulsive acceleration by altering the measurement timing.

Table 2.5: Predicted posterior standard deviation of the propulsive acceleration at a 410 km altitude orbit for different firing times and measurement intervals. Standard deviations are given in units of μm/s^2. Firing time is representative of half of the total maneuver duration.

	Firing Time [hr]									
Measurement Interval [min]	1	2	3	4	5	6	7	8	9	10
1	7.789	1.618	1.069	0.854	0.730	0.653	0.593	0.546	0.508	0.476
2	8.942	1.720	1.099	0.866	0.748	0.655	0.598	0.550	0.515	0.479
3	9.551	1.800	1.122	0.877	0.738	0.668	0.602	0.553	0.517	0.484
4	9.950	1.864	1.132	0.880	0.748	0.668	0.603	0.559	0.516	0.482
5	10.169	1.930	1.161	0.886	0.752	0.668	0.605	0.561	0.513	0.486
6	10.358	1.995	1.165	0.893	0.749	0.670	0.605	0.558	0.520	0.486
7	12.488	2.075	1.227	0.907	0.768	0.671	0.609	0.562	0.517	0.487
8	12.604	2.083	1.229	0.902	0.765	0.674	0.613	0.564	0.524	0.489
9	13.524	2.237	1.206	0.927	0.764	0.673	0.617	0.570	0.523	0.493
10	10.801	2.168	1.223	0.918	0.758	0.673	0.614	0.561	0.521	0.488
20	11.457	2.470	1.314	0.949	0.778	0.685	0.619	0.569	0.531	0.494
30	11.897	3.036	1.415	0.997	0.800	0.693	0.622	0.576	0.531	0.491

Table 2.6: Predicted posterior standard deviation of the propulsive acceleration at a 700 km altitude orbit for different firing times and measurement intervals. Standard deviations are given in units of μm/s^2. Firing time is representative of half of the total maneuver duration.

	Firing Time [hr]									
Measurement Interval [min]	1	2	3	4	5	6	7	8	9	10
1	8.249	0.682	0.308	0.193	0.148	0.125	0.112	0.103	0.093	0.087
2	9.714	0.892	0.385	0.224	0.162	0.132	0.116	0.105	0.096	0.088
3	10.442	1.047	0.443	0.249	0.174	0.139	0.119	0.106	0.098	0.090
4	10.930	1.173	0.492	0.271	0.185	0.144	0.122	0.109	0.099	0.091
5	11.176	1.279	0.533	0.290	0.195	0.149	0.126	0.111	0.100	0.092
6	11.385	1.371	0.570	0.307	0.203	0.154	0.130	0.113	0.102	0.092
7	13.461	1.481	0.644	0.329	0.219	0.161	0.131	0.115	0.102	0.094
8	13.571	1.529	0.667	0.337	0.225	0.163	0.135	0.116	0.104	0.094
9	14.371	1.687	0.659	0.373	0.231	0.168	0.139	0.118	0.104	0.095
10	11.857	1.656	0.683	0.362	0.233	0.173	0.139	0.119	0.105	0.095
20	12.359	2.118	0.861	0.450	0.285	0.204	0.159	0.131	0.113	0.100
30	13.555	3.010	0.980	0.509	0.325	0.231	0.175	0.140	0.119	0.105

As in the previous sections, a basic maneuver is considered where for an overall maneuver duration, T, the propulsion system is assumed to be turned on for $t < \frac{1}{2}T$ and off for $t \geq \frac{1}{2}T$. The specific question addressed in this section is given a maximum number of possible measurement locations M, when should each measurement be taken in order to minimize the posterior uncertainty of the propulsive acceleration? The linear measurement model allows such a question to be posed, since from Eq. 2.96 the posterior covariance of the parameter vector can be analytically computed for a given set of measurement times.

Define Σ_{a_1} as the component on the diagonal of the posterior covariance of the parameters that corresponds to the marginal variance of a_1, which physically represents the propulsive acceleration. The optimization problem is then

$$\begin{aligned} \min_{\tau} \quad & \Sigma_{a_1}(\tau) && (2.107) \\ \text{subject to} \quad & \tau_{i+1} - \tau_i \geq \Delta t_{\min} \quad \forall i \in \{1, \ldots, M-1\} && (2.108) \\ \text{and} \quad & \tau_M \leq T && (2.109) \end{aligned}$$

where τ is a $M \times 1$ vector corresponding to all of the measurement times. The constraint of Eq. 2.108 enforces a minimum time between successive measurements and that the measurement vector is ordered such that the first measurement corresponds to τ_1 and the last measurement corresponds to τ_M. The combination of Eq. 2.109 with Eq. 2.108 enforces that all measurements will occur within the maneuver period.

The optimization was tested for a maneuver at a 400 km altitude orbit with an overall duration of 10 hours, 50 measurement locations, and a minimum time between successive measurements of 5 minutes. Modeling error was not considered during this analysis. As reference, when the measurements are evenly distributed across the maneuver duration, the posterior standard deviation of the propulsive acceleration was 1.63 ng. The measurement vector was optimized using MATLAB's inbuilt `fmincon` function with the starting point being a measurement vector with measurements evenly distributed across the maneuver duration. Figure 2-21 shows a locally-optimized Kalman gain versus time for the radial and along-track position errors. The measurement locations have quite clearly clustered around the times where the Kalman gain for the along-track position errors is high. The posterior standard deviation for the propulsive acceleration with the locally-optimized measurement locations is 1.31 ng, representing a 20% decrease in the posterior standard deviation. Future

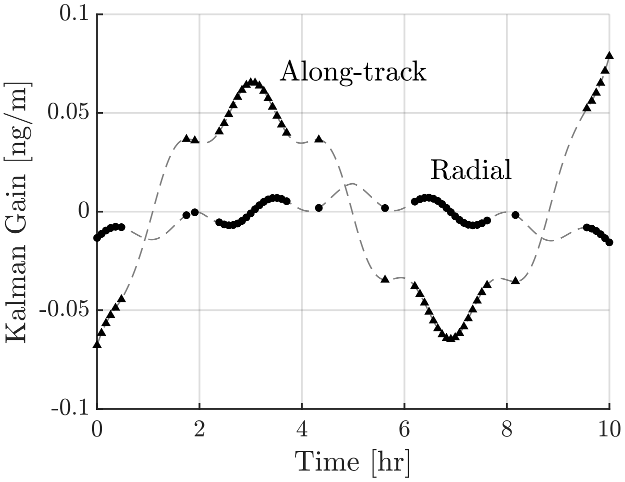

Figure 2-21: Kalman gain for the optimize measurement timings. Markers indicate measurement locations while dashed lines represent the underlying trend in the Kalman gain.

work will explore similar optimizations for cases with modeling error.

Chapter 3

Proximity Operations

Remote inspection of an in-space object allows for an assessment of the condition of the object's exterior and can be conducted with ground-based instruments or in proximity to the object. While not commonly used, remote inspection could be used to determine the health of high-value spacecraft, such as those with astronauts on board, or assess a piece of debris prior to attempting to capture it. As the probability of returning astronauts to the Moon or sending them to deep space increases, along with the advancement of technologies for active debris removal, the ability to perform remote inspection of in-space objects becomes more and more valuable.

Different methodologies for remote inspection can be compared based on their ability to provide coverage of the exterior surface of the target object, the spatial resolution which can be achieved, as well as their overall risk [68]. Of all the available methods, inspection with a free-flying small spacecraft is a highly attractive option due to its ability to provide good coverage and spatial resolution while not incurring significant risk in terms of cost or human involvement. These free-flying inspectors could either be launched from the target object, if for instance the target object is a spacecraft, or rendezvous with the target, if the target is a small near-Earth asteroid.

Although this thesis is concerned with proximity operations around a small asteroid, proximity operations around another spacecraft is a similar problem. Surveying an asteroid is similar to inspecting another spacecraft, in both cases the surveyor/inspector spacecraft needs to circumnavigate the target in order to visually inspect it. Landing on an asteroid is also similar to docking with another spacecraft. The only difference between the two cases is the greater gravitational acceleration in the asteroid case, but for small asteroids the gravitational acceleration can sometimes be neglected. In addition, the available literature for proximity operations around another spacecraft is considerably greater than that of proximity operations around an asteroid.

At the most basic level, remote inspection can be conducted with simple micro-spacecraft designed for short-term inspection of a target object. Passive CubeSats for spacecraft inspection have been proposed where the spacecraft contains no actuation system [68]. This method minimizes many of the risks associated with free-flying spacecraft such as plume impingement, but cannot provide good coverage of the entire exterior of the target object without requiring the use of multiple inspector spacecraft, has limited inspection time before it drifts too far away from the target, and is not applicable to uncooperative targets such as a near-Earth asteroid or a piece of debris.

A step above the passive approach is to outfit the inspector spacecraft with a simple cold-gas propulsion system. The high thrust density of cold-gas propulsion, relative to other miniaturized propulsion technologies such as electrospray propulsion, means that nozzles can be placed along each axis of the spacecraft in order to provide linear position dynamics. The guidance systems for these spacecraft are often quite straightforward and rely on the linear dynamics in order to simplify the control strategy. Point-to-point maneuvering, where the spacecraft simply regulates its position to a series of waypoints, is the most basic maneuvering strategy [69]. For targets around a large central body, such as Earth, the natural orbital dynamics can be leveraged in order to create trajectories based on a series of impulsive maneuvers [70]. Alternatively, the spacecraft can be forced into a circumnavigating trajectory around the target which costs more propellant, but allows for finer control over the maneuver [71]. More complex maneuvers that use both natural and forced motion can be devised that take into account further constraints such as maintaining illumination from the Sun on the solar panels [72].

These methodologies are appealing due to their simplicity. However, while maneuvers based in natural orbit motion leverage the dynamics to save fuel and avoid plume impingement, they are also at the mercy of those same natural dynamics. In particular, the period of the circumnavigating inspection trajectories will be the same as the orbital period of the target. For targets in low-Earth orbit this might be acceptable as orbital periods are around 90 minutes. However, in geostationary orbit the orbital period rises to a day and in deep space the orbital period is on the order of years. Clearly, for maneuvering strategies that are applicable to scenarios beyond low-Earth orbit such as surveying a small asteroid, forced motion is required. The forced circular motion of Ref. [71] is a promising start, but the range of developed maneuvers is limited and is constrained to fully-actuated systems.

Beyond the desire to increase the number of possible maneuvers, it may also be desired to use propulsion systems other than cold-gas propulsion. The low efficiency of cold-gas propulsion restricts its use to missions with low maneuvering requirements. In particular, cold-gas propulsion can not be used for a reconnaissance spacecraft that travels between multiple pieces of debris or for long-duration inspection missions where the inspector spacecraft is required to be active over the course of several months. While cold-gas propulsion dominates the list of CubeSat-compatible propulsion systems with flight heritage, other propulsion technologies are being developed that could resolve this issue [7]. One such example is microfabricated electrospray propulsion [22, 24, 30] which has the potential to provide relatively high thrust density while also not requiring significant amounts of power. These types of thrusters have also been demonstrated in a laboratory environment for control of a CubeSat-like test vehicle [25].

The use of propulsion systems other than cold-gas propulsion creates other challenges for the maneuvering of a free-flying inspector spacecraft, many of which are covered in Ref. [73]. The exhaust of chemical and electric propulsion systems can be reactive and contaminate any surfaces that they impinge on [74, 75]. Furthermore, due to low thrust density and challenges associated with placing thrusters along multiple axes, the thrust axis for the propulsion system is usually fixed with respect to the spacecraft body causing the spacecraft to be underactuated.[1] Therefore, maneuvering methodologies that are applicable to propulsion systems such as electrospray thrusters need to be able to handle plume impingement constraints as well as underactuated spacecraft.

For a more expansive set of maneuvers that can handle constraints such as plume impingement and underactuation, mathematical programming, where the trajectory planning process is expressed as a constrained optimization, is typically used. Mixed-integer linear

---

[1] For simplification of terminology, a spacecraft will be considered underactuated if the direction of its thrust vector is constrained by the spacecraft's attitude such that the direction of the thrust vector cannot be arbitrarily set. While limits on thrust magnitude also technically count as underactuation, all practical systems are underactuated in this manner. In addition, underactuation in terms of thrust direction places nonlinear constraints on the system dynamics while underactuation in terms of thrust magnitude only places linear constraints.

programming allows for a trajectory to be planned that can account for multiple different types of constraints such as plume impingement [76] or that the trajectory always be passively safe [77]. However, this formulation requires that the spacecraft not be underactuated in order to ensure that the dynamics remain linear. Methods that enable continuous constraint satisfaction have also been explored, but for impulsive maneuvers [78]. A model-predictive control approach has also been considered where the trajectory optimization through mathematical programming is used as a feedback controller. However, these cases again require linear dynamics [79] or that the control law for specific maneuvers be solved for on the ground [80]. Plume impingement has been considered as a soft constraint by including it in the cost function, but is omitted during the results as it added too much complexity to the optimization [81]. Underactuation has also been considered by placing a quadratic cost on changes to the desired thrust vector [82], but as a result also penalizes changes to the thrust magnitude in addition to changes in thrust direction.

Other techniques for planning trajectories that are, at least currently, less popular than mathematical programming include graph search [83], sample-based planning [84], and applications of the sequential gradient-restoration algorithm [85]. However, these solutions are too computationally expensive to be performed online, in their current form, by a small spacecraft and require a solution to be found on the ground. For all of these methods, including mathematical programming, there is a secondary cost that is usually not considered. Typically, the goal of the optimization is to minimize propellant cost of the trajectory, thereby implicitly maximizing the available mass for payload or the number of maneuvers that can be accomplished. However, the computational cost of performing nonlinear optimization is beyond the capabilities of current small spacecraft computers. As such, in order to implement these methods, more powerful computers are required which in turn requires more power and a larger power system as well as better thermal control and a larger thermal management system. Therefore, it is very likely that the increase for better computation, power, and thermal systems will outweigh any propellant savings gained by optimization.

Specifically related to plume impingement, alternative methods, outside of trajectory planning, have been used. For human-in-the-loop maneuvers, the maximum thrust output of the thrusters facing the target spacecraft was reduced in an attempt to minimize the effects of plume impingement [86]. Alternative actuation methods such as electromagnetic forces have also been suggested [87] where any chance of plume impingement is eliminated.

These approaches are not applicable for this work. Reducing the thrust output can reduce structural loads created by plume impingement but does not prevent surface contamination. Electromagnetic actuation does show some promise for formation flight, but requires all parties involved to be cooperative, a situation that is not necessarily true for spacecraft inspection and is certainly not true for asteroid surveying.

Proximity operations around asteroids differs from that of around other spacecraft due to the presence of a notable gravitational field. All asteroids that have so far been visited are relatively large and therefore have strong enough gravitational pull that a spacecraft can enter into orbit. However, because of their small size and therefore weak gravitational pull, relative to planets, asteroids have irregular, non-spherical shapes leading to orbit trajectories that are non-periodic and sometimes unstable. As such, most of the prior research for proximity operations around small asteroids has focused on station-keeping in order to maintain orbit stability.

The simplest approach to station keeping is to hover, where the spacecraft is stationary either in the inertial frame or in a frame rotating with the asteroid. Stability criteria for hovering near irregularly-shaped asteroids has been studied [88] and a dead-band controller for state regulation was developed [89]. Both of these solutions require that the spacecraft is fully actuated as they opt for an impulsive dead-band controller. Underactuation has also been considered for hovering where the underactuation is caused by the loss of thrust along one axis [90]. Hovering was successfully implemented during the Hayabusa mission [91], allowing the spacecraft to approach near to the asteroid's surface.

Solutions other than hovering attempt to maintain periodic orbits. A nonlinear feedback control law has been devised that regulates the orbit of a spacecraft around an irregularly-shaped asteroid to any circular orbit [92] and has application to hovering [93]. However, this solution controls the orbit geometry and not the actual spacecraft state. While it is useful for ensuring that coverage is provided to certain regions of the asteroid, it cannot be used to provide continuous measurements above specific points of the asteroid. A model-predictive controller has also been considered for binary asteroid systems [94], but requires a fully-actuated spacecraft and assumes that propulsive input to the spacecraft is applied impulsively.

Outside of surveying, landing on the asteroid is the other major maneuver that might be performed during proximity operations. Of all of the asteroids that have been visited by a spacecraft, only four have been physically contacted by a spacecraft. The Near-Earth Asteroid Rendezvous (NEAR) Shoemaker spacecraft conducted an improvised landing on Eros, the Hayabusa and Hayabusa2 spacecraft peformed surface sample collection on the asteroids Itokawa and Ryugu respectively, and the Origins, Spectral Interpretation, Resource Identification, Security, Regolith Explorer (OSIRIS-REx) spacecraft collected a surface sample from the asteroid Bennu.

For the most part, landing strategies that have been implemented were essentially controlled free fall. The landing trajectory of the NEAR Shoemaker spacecraft consisted of a series of pre-timed braking maneuvers designed to minimize impact velocity [95] as well as provide time to capture high-resolution images of the surface of Eros [96]. The Hayabusa missions followed a similar strategy [91, 97], except during the sample collection the spacecraft performed touch-and-go maneuvers. In all cases, the descent trajectories relied in the spacecraft being fully actuated, in order to maintain controllability, and that the contamination from plume impingement on the surface would not be significant. Both Hayabusa missions also carried small rovers which were deployed above the asteroid and allowed to fall to the surface with no braking maneuvers. However, this method carries a lot of risk, and the Micro-Nano Experimental Robot Vehicle for Asteroid (MINERVA) lander deployed by Hayabusa bounced off of the surface with sufficient energy to escape the gravitational pull of the asteroid [91].

More advanced landing strategies have been studied academically by solving for point solutions with calculus of variations [98], using sliding surfaces [99], or using invariant manifolds [100]. However, these methods either rely on an analytical representation of the gravitational field of the asteroid [98, 99] or at least a very accurate model [100]. Estimation of an asteroid's gravitational field is a difficult problem and may approaches rely on reconstruction of the field based on large amounts of flight data. In addition, these more advanced techniques do not improve on the controlled free fall techniques employed by NEAR Shoemaker and the Hayabusa missions significantly enough to warrant their added complexity.

3.1 Research Gap

A comparison of the maneuvering methods designed for actual spacecraft and maneuvering methods developed in theory show that a technology gap exists between the two. The former are compatible with spacecraft computers but lack applicability for more complex maneuvering or underactuated spacecraft architectures while the latter expand the possible maneuvers and architectures but are incompatible with spacecraft computers. Methodologies that are able to bridge this gap are required in order to open up the use of high-efficiency propulsion, such as electrospray propulsion, for use during autonomous remote inspection.

This work presents an analytical library for maneuvering of an underactuated spacecraft around a target object for remote inspection. An analytical maneuver library allows for a wider range of inspection missions to be accomplished while avoiding the secondary costs associated with numerical optimization, thereby permitting their implementation on small spacecraft. These trajectories will allow underactuated spacecraft to be considered as viable platforms for missions in proximity operations and enable the move towards more autonomous spacecraft that do not rely on communications with Earth for trajectory design. The contents of this chapter have been published in Ref. [101].

3.2 Spacecraft Controllability

Figure 3-1 shows a notional spacecraft which operates in a two-dimensional world. The spacecraft has a propulsion system capable of producing thrust in the positive y_b direction and a reaction wheel capable of producing torques along the z axis. The dynamics of the spacecraft are given by

$$\ddot{x} = \frac{F}{m}\sin\phi \tag{3.1}$$

$$\ddot{y} = -\frac{F}{m}\cos\phi \tag{3.2}$$

$$\ddot{\phi} = \frac{\tau}{I} \tag{3.3}$$

where F is the thrust produced by the propulsion system, m is the spacecraft's mass, ϕ is the spacecraft's heading measured anti-clockwise from the negative-y direction, τ is the torque produced by the reaction wheel, and I is the rotational inertia of the spacecraft about the z axis.

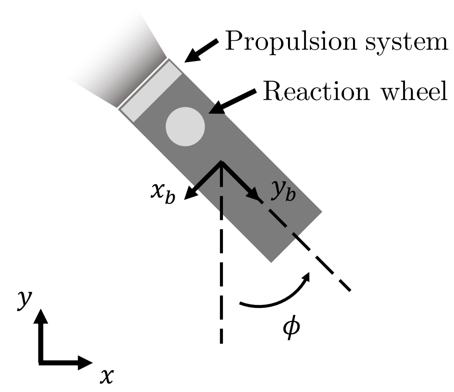

Figure 3-1: Notional spacecraft.

Defining

$$v_x \equiv \ddot{x}; \quad v_y \equiv \ddot{y}; \quad \omega \equiv \ddot{\phi} \tag{3.4}$$

then equilibrium in the inertial frame is given by $v_x = v_y = 0$ and $\omega = 0$ as well as zero control input, $F = 0$ and $\tau = 0$. Linearizing the system about a heading, ϕ_0, then the linearized dynamics are given by

$$\begin{bmatrix} \dot{x} \\ \dot{y} \\ \dot{v}_x \\ \dot{v}_y \\ \dot{\phi} \\ \dot{\omega} \end{bmatrix} = \begin{bmatrix} 0 & 0 & 1 & 0 & 0 & 0 \\ 0 & 0 & 0 & 1 & 0 & 0 \\ 0 & 0 & 0 & 0 & 0 & 0 \\ 0 & 0 & 0 & 0 & 0 & 0 \\ 0 & 0 & 0 & 0 & 0 & 1 \\ 0 & 0 & 0 & 0 & 0 & 0 \end{bmatrix} \begin{bmatrix} x \\ y \\ v_x \\ v_y \\ \phi \\ \omega \end{bmatrix} + \begin{bmatrix} 0 & 0 \\ 0 & 0 \\ \frac{\sin\phi_0}{m} & 0 \\ -\frac{\cos\phi_0}{m} & 0 \\ 0 & 0 \\ 0 & \frac{1}{I} \end{bmatrix} \begin{bmatrix} F \\ \tau \end{bmatrix} \tag{3.5}$$

The controllability matrix for this system, M_c, is given by

$$M_{\mathrm{c}} = \begin{bmatrix} B & AB & A^2B & \cdots & A^5B \end{bmatrix} \tag{3.6}$$

$$= \begin{bmatrix} 0 & 0 & \frac{\sin\phi_0}{m} & 0 & 0 & \cdots & 0 \\ 0 & 0 & -\frac{\cos\phi_0}{m} & 0 & 0 & \cdots & 0 \\ \frac{\sin\phi_0}{m} & 0 & 0 & 0 & 0 & \cdots & 0 \\ 0 & -\frac{\cos\phi_0}{m} & 0 & 0 & 0 & \cdots & 0 \\ 0 & 0 & 0 & \frac{1}{I} & 0 & \cdots & 0 \\ 0 & \frac{1}{I} & 0 & 0 & 0 & \cdots & 0 \end{bmatrix} \tag{3.7}$$

Since the controllability matrix only has four independent columns, it is rank deficient and the linearized system is not controllable. Intuitively, the spacecraft cannot respond to any disturbances along the x_{b} axis as neither modulating the propulsion system thrust nor rotating the spacecraft will produce a force along the x_{b} axis on their own. It is worth noting that modulating the thrust and rotating the spacecraft simultaneously would produce a force along the x_{b} axis but is not a linear response.

The system as defined has further complications beyond just being uncontrollable along the x_{b} axis. Since the propulsion system is unable to produce negative thrust, the spacecraft will not be able to respond to disturbances in the positive y_{b} direction. Both the controllability and negative thrust problems would be solved if in the equilibrium state the propulsion system is required to produce a positive thrust. This is possible if the spacecraft uses its propulsion system to place itself in a circular orbit around the target as shown in Figure 3-2. In this case, the spacecraft orbits around the target with constant radius r and angular frequency Ω with the required centripetal acceleration, $r\Omega^2$, being provided by the propulsion system.

The position dynamics for a frame centered on the target, instantaneously aligned with the inertial frame, but rotating with constant angular frequency $\vec{\Omega}$ can be calculated from

$$\vec{a}_i = \vec{a}_r + 2\vec{\Omega} \times \vec{v}_r + \vec{\Omega} \times \left(\vec{\Omega} \times \vec{r}_r\right) \tag{3.8}$$

where $\vec{a}$ is acceleration, $\vec{v}$ is velocity, and $\vec{r}$ is position. Subscript i corresponds to coordinates in the instantaneously-aligned inertial frame while subscript r corresponds to coordinates in the rotating frame. The rotational dynamics of the spacecraft are unaffected by the

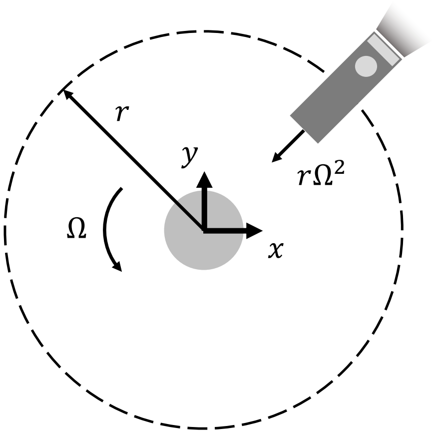

Figure 3-2: Circular orbit used to allow for position control of the underactuated spacecraft with linear control methods.

coordinate transformation.

Assuming that the only accelerations in the inertial frame are from the propulsion system

$$\vec{a}_i = \frac{F}{m}\begin{bmatrix} \sin\phi \\ -\cos\phi \\ 0 \end{bmatrix} \tag{3.9}$$

and that the angular frequency of the rotating frame is in the positive z direction

$$\vec{\Omega} = \begin{bmatrix} 0 \\ 0 \\ \Omega \end{bmatrix} \tag{3.10}$$

with constant magnitude Ω, then the dynamics in the x-y plane of the rotating frame are

$$\ddot{x}_r = \Omega^2 x_r + 2\Omega v_{y,r} + \frac{F}{m}\sin\phi \tag{3.11}$$

$$\ddot{y}_r = \Omega^2 y_r - 2\Omega v_{x,r} - \frac{F}{m}\cos\phi \tag{3.12}$$

$$\ddot{\phi} = \frac{\tau}{I} \tag{3.13}$$

Equilibrium in this rotating frame is again given by $v_{x,r} = v_{y,r} = 0$ and $\omega = 0$ along with $\tau = 0$. However, for a given position in the rotating frame, the equilibrium input thrust is now

$$F^* = m\Omega^2\sqrt{x_r^2 + y_r^2} \tag{3.14}$$

with equilibrium heading

$$\phi^* = \tan^{-1}\left(-\frac{x_r}{y_r}\right) \tag{3.15}$$

Picking the equilibrium position to be $x_r = 0$ and $y_r = r_\mathrm{d}$ where r_d is the desired orbital radius, then the equilibrium thrust is $F^* = mr_\mathrm{d}\Omega^2$ with corresponding heading $\phi^* = 0$. Linearizing the system at this equilibrium point gives the linearized dynamics

$$\begin{bmatrix} \dot{x} \\ \dot{y} \\ \dot{v}_x \\ \dot{v}_y \\ \dot{\phi} \\ \dot{\omega} \end{bmatrix} = \begin{bmatrix} 0 & 0 & 1 & 0 & 0 & 0 \\ 0 & 0 & 0 & 1 & 0 & 0 \\ \Omega^2 & 0 & 0 & 2\Omega & r_\mathrm{d}\Omega^2 & 0 \\ 0 & \Omega^2 & -2\Omega & 0 & 0 & 0 \\ 0 & 0 & 0 & 0 & 0 & 1 \\ 0 & 0 & 0 & 0 & 0 & 0 \end{bmatrix} \begin{bmatrix} x \\ y \\ v_x \\ v_y \\ \phi \\ \omega \end{bmatrix} + \begin{bmatrix} 0 & 0 \\ 0 & 0 \\ 0 & 0 \\ -\frac{1}{m} & 0 \\ 0 & 0 \\ 0 & \frac{1}{I} \end{bmatrix} \begin{bmatrix} F \\ \tau \end{bmatrix} \tag{3.16}$$

The controllability matrix for this new system, $M_{c,r}$, is given by

$$M_{c,r} = \left[\begin{array}{cccccccc} 0 & 0 & 0 & 0 & -\frac{2\Omega}{m} & 0 & & \\ 0 & 0 & -\frac{1}{m} & 0 & 0 & 0 & & \\ 0 & 0 & -\frac{2\Omega}{m} & 0 & 0 & \frac{r\Omega^2}{I} & \text{dependent} & \\ -\frac{1}{m} & 0 & 0 & 0 & \frac{3\Omega^2}{m} & 0 & \text{columns} & \\ 0 & 0 & 0 & \frac{1}{I} & 0 & 0 & & \\ 0 & \frac{1}{I} & 0 & 0 & 0 & 0 & & \end{array}\right] \tag{3.17}$$

The first six columns of this new controllability matrix are independent, meaning that the controllability matrix is full rank and that the system is controllable. Therefore, linear control techniques can be applied in order to regulate the spacecraft's position to the equilibrium state in the rotating frame. While this analysis was conducted in two dimensions, for clarity in the equations, the same results will occur in three dimensions. The spacecraft will be uncontrollable at the equilibrium state of the inertial frame but is controllable at the equilibrium state of the rotating frame.

3.3 Baseline Orbit

The proposed baseline motion of the spacecraft during proximity operations is the circular orbit shown in Figure 3-2. This circular motion allows linear control methods to be applied to regulate the spacecraft's position and allow it to reject external disturbances. This orbit also has the bonus of implicitly avoiding plume impingement on the central target. Since the spacecraft has to thrust inwards, towards the target, in order to provide the necessary centripetal acceleration, the plume of the propulsion system will always be directed away from the target. In addition, the side of the spacecraft opposite from the propulsion system will always be pointed towards the target, providing a convenient location for cameras for visual inspection or other scientific instruments.

While the circular motion allows for linear position control and avoids plume impingement, it does require a constant acceleration to be provided by the propulsion system, creating two potential downslides to this strategy. First, the propulsion system needs to be able to produce the necessary centripetal acceleration in order to maintain the circular motion. This is indirectly a constraint on the overall time for any inspection maneuvers as the required acceleration can be made arbitrarily small by decreasing the orbit frequency, at the cost of slower maneuvers. Second, even in a scenario with zero external disturbances, the spacecraft will constantly be using propellant. However, the low required centripetal acceleration and high efficiency of electrospray propulsion mean that the propellant cost is negligible, even for long-term inspection.

As an example scenario, consider a 3U CubeSat inspector spacecraft with a mass, m, of 4 kg and an electrospray propulsion system capable of producing a thrust, F, of 100 μN. If the desired inspection radius, r, is 10 m, then the maximum orbit frequency that can be maintained is

$$\Omega_{\text{max}} = \sqrt{\frac{F}{mr}} \tag{3.18}$$

and is 1.6 mrad/s. The period of the inspection orbit is therefore 66 minutes, which is still faster than the 90-minute inspection period that would be allowed by natural orbital dynamics in low-Earth orbit. Assuming that the propellant mass is negligible relative to the overall mass of the spacecraft, the required propellant per orbit can be approximated from

$$m_{\mathrm{p}} = \frac{F}{I_{\mathrm{sp}} g} \frac{2\pi}{\Omega_{\max}} = \frac{2\pi\sqrt{Fmr}}{I_{\mathrm{sp}} g} \tag{3.19}$$

where I_{sp} is the specific impulse of the propulsion system and g is the standard gravitational acceleration. Typical specific impulses for electrospray thrusters are approximately 1000 s. In this scenario, the spacecraft would use 41 mg of propellant per orbit and could perform almost 25 inspection orbits before using a single gram of fuel. Comparatively, for a cold-gas propulsion system with a specific impulse of 80 s, the propellant used per orbit would be approximately 506 mg and would allow for almost 2 orbits per gram of fuel.

3.4 Maneuver Library

In order to make use of the baseline orbit for remote inspection, several maneuvers need to be designed. Most importantly, the spacecraft needs to be able to join the circular orbit from a stationary position as well as leave the circular orbit back to a stationary position. Both joining and leaving the circular orbit are the same process just executed in opposite directions in time, and therefore will be considered a single maneuver. Next, the spacecraft needs to be able to change the radius of the circular orbit. With these two maneuvers, joining/leaving the circular orbit and changing the orbit's radius, the spacecraft will be able to perform point-to-point maneuvering through a series of waypoints in three dimensions, circumnavigation maneuvers, as well as landing on or docking to a rotating target.

The remaining maneuvers in the library do not add additional functionality, but rather simplify the overall mission design. Changing the frequency of the orbit could be accomplished by leaving the initial orbit and then joining a new orbit of the desired new frequency. However, it is relatively simple to design maneuvers to increase or decrease the orbital frequency within the framework developed here. Similarly, translating the orbital plane along its normal vector could be achieved by a convoluted set of maneuvers, but it is relatively simple to design a single maneuver to accomplish this task.

All maneuvers are designed by leveraging the differential flatness of the underactuated spacecraft. In particular, by defining a subset of the spacecraft's state as well as control inputs, the entire state of the spacecraft can be determined including the spacecraft's heading and rotational velocity with respect to the rotating frame. An additional consideration for simplifying the maneuver design is to constrain the coordinate frame such that the x and y axes always lie in the orbit plane and that the frequency of the rotating frame, Ω, always points in the positive-z direction.

For dynamic consistency, any maneuvers that start or end on the circular trajectory need to have a nadir-pointing attitude such that there are no discontinuities between the spacecraft's heading at the boundaries of each maneuver and the baseline circular orbit. In addition, the rotational velocity of the spacecraft in the rotating frame needs to be zero at the beginning and end of all maneuvers for the same reason. Figure 3-3 shows the spacecraft in the rotating frame with the heading of the spacecraft, ϕ, defined as anti-clockwise rotation relative to a nadir-pointing attitude. For maneuver, design it is assumed that the spacecraft is on the positive-y axis of the rotating frame such that $x = 0$ and $y > 0$, and that the magnitude of the frequency of the rotating frame, Ω, is varied in order to maintain $x = 0$. The dynamics in the rotating frame for a variable frequency are

$$\vec{a}_i(t) = \vec{a}_r(t) + 2\vec{\Omega}(t) \times \vec{v}_r(t) + \dot{\vec{\Omega}}(t) \times \vec{r}_r(t) + \vec{\Omega}(t) \times \left(\vec{\Omega}(t) \times \vec{r}_r(t)\right) \tag{3.20}$$

Assuming that $\vec{\Omega}$ still points purely in the positive-z direction with magnitude Ω, then the dynamics in the x-y plane are

$$\ddot{x}(t) = \Omega^2(t)x(t) + 2\Omega(t)\dot{y}(t) + \dot{\Omega}(t)y(t) + a_x(t) \tag{3.21}$$

$$\ddot{y}(t) = \Omega^2(t)y(t) - 2\Omega(t)\dot{x}(t) - \dot{\Omega}(t)x(t) + a_y(t) \tag{3.22}$$

Under the condition that $x = 0$ for all time, then the dynamics become

$$0 = 2\Omega(t)\dot{y}(t) + \dot{\Omega}(t)y(t) + a_x(t) \tag{3.23}$$

$$\ddot{y}(t) = \Omega^2(t)y(t) + a_y(t) \tag{3.24}$$

Given a particular input acceleration of $a_x(t)$ along the x axis and $a_y(t)$ along the y axis, the heading of the spacecraft can be calculated from

$$\tan\phi(t) = -\frac{a_x(t)}{a_y(t)} \tag{3.25}$$

In situations in which the spacecraft needs to have a nadir-pointing attitude this confirms

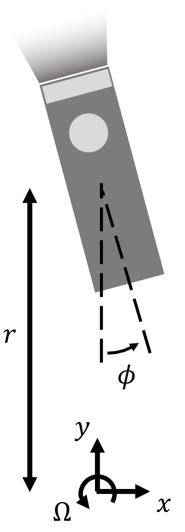

Figure 3-3: Spacecraft in the rotating frame.

the intuition that $a_x = 0$ and $a_y < 0$, or that the spacecraft is producing an acceleration towards the center of the circular orbit. The spacecraft's rotational velocity, ω, can be calculated by taking the time derivative of both sides of Eq. 3.25 and solving for ω as

$$\omega(t) = \frac{d}{dt}\phi(t) = \frac{1}{a_x^2(t) + a_y^2(t)} \left(a_x(t)\frac{d}{dt}a_y(t) - a_y(t)\frac{d}{dt}a_x(t) \right) \tag{3.26}$$

Therefore, one way to ensure that $\omega = 0$ at the beginning and end of each maneuver is to enforce the constraints

$$a_x(t) = 0 \qquad \text{or} \qquad \frac{d}{dt}a_y(t) = 0 \tag{3.27}$$

and

$$a_y(t) = 0 \qquad \text{or} \qquad \frac{d}{dt}a_x(t) = 0 \tag{3.28}$$

3.4.1 Joining Orbit from Rest

The goal of the joining-orbit maneuver is to transition the spacecraft from a static position in the inertial frame to a circular orbit around the target of a desired radius r_d and frequency Ω_d. Since the spacecraft does not start this maneuver on the circular orbit, it is not required to have a nadir-pointing attitude and can start the maneuver in any desired attitude.

The approach for designing the joining-orbit maneuver is to constrain the radial position of the spacecraft to be constant at the desired radial position, r_d. Under this condition, the dynamics from Eqs. 3.23 and 3.24 become

$$0 = \dot{\Omega}(t) r_\mathrm{d} + a_x(t) \tag{3.29}$$

$$0 = \Omega^2(t) r_\mathrm{d} + a_y(t) \tag{3.30}$$

By selecting the correct profile for $a_x(t)$, $\Omega(t)$ is driven from zero to the desired frequency, Ω_d. After solving for $\Omega(t)$, $a_y(t)$ can then be solved for from Eq. 3.30 as

$$a_y(t) = -\Omega^2(t) r_\mathrm{d} \tag{3.31}$$

Consider a polynomial profile for $a_x(t)$ of the form

$$a_x(t) = -a_1 \left(1 - \frac{t}{t_{\mathrm{p},1}}\right)^n \tag{3.32}$$

where a_1 is a positive constant, $t_{\mathrm{p},1}$ is the overall time of the maneuver profile, and n is a free parameter that sets the degree of the profile. By design, $a_x(t_{\mathrm{p},1}) = 0$ as long as $n \neq 0$. Additionally, since

$$\dot{a}_x(t) = \frac{n a_1}{t_{\mathrm{p},1}} \left(1 - \frac{t}{t_{\mathrm{p},1}}\right)^{n-1} \tag{3.33}$$

then $\dot{a}_x(t_{\mathrm{p},1}) = 0$ as long as $n > 1$. Therefore, the rotational velocity of the spacecraft in the rotating frame will be zero at the end of the trajectory. As the maneuver will be constructed such that $\Omega(t_{\mathrm{p},1}) = \Omega_\mathrm{d}$, then the spacecraft will also have a nadir-pointing attitude at the end of the trajectory since from Eq. 3.31, $a_y(t_{\mathrm{p},1}) = -\Omega_\mathrm{d}^2 r_\mathrm{d}$.

The frequency of the orbit over time can be solved for as

$$\Omega(t) = -\frac{1}{r_\mathrm{d}} \int_0^t a_x(\tau) d\tau \tag{3.34}$$

$$= \frac{a_1 t_{\mathrm{p},1}}{(n+1) r_\mathrm{d}} \left[1 - \left(1 - \frac{t}{t_{\mathrm{p},1}}\right)^{n+1}\right] \tag{3.35}$$

which, based on Eq. 3.31, gives an acceleration along the y-axis of

$$a_y(t) = -\frac{a_1^2 t_{\mathrm{p},1}^2}{(n+1)^2 r_{\mathrm{d}}} \left[1 - \left(1 - \frac{t}{t_{\mathrm{p},1}}\right)^{n+1}\right]^2 \tag{3.36}$$

At the beginning of the trajectory, it can be seen that $a_y(0) = 0$. In addition,

$$\dot{a}_y(t) = -\frac{2a_1^2 t_{\mathrm{p},1}}{(n+1) r_{\mathrm{d}}} \left[1 - \left(1 - \frac{t}{t_{\mathrm{p},1}}\right)^{n+1}\right] \left(1 - \frac{t}{t_{\mathrm{p},1}}\right)^{n} \tag{3.37}$$

so $\dot{a}_y(0) = 0$. Therefore, at the beginning of the trajectory the rotational velocity of the spacecraft in the rotating frame will be zero. Since the rotating frame will have a rotational frequency of zero at the beginning of the trajectory, this also means that the rotational velocity of the spacecraft in the inertial frame will also be zero.

The trajectory needs to be correctly sized, by setting a_1 and $t_{\mathrm{p},1}$, such that $\Omega(t_{\mathrm{p},1}) = \Omega_{\mathrm{d}}$. From Eq. 3.35

$$\Omega(t_{\mathrm{p},1}) = \frac{a_1 t_{\mathrm{p},1}}{(n+1) r_{\mathrm{d}}} \tag{3.38}$$

Therefore, the choice of a_1 and $t_{\mathrm{p},1}$ must satisfy

$$a_1 t_{\mathrm{p},1} = (n+1) r_{\mathrm{d}} \Omega_{\mathrm{d}} \tag{3.39}$$

An additional constraint could be that the required acceleration magnitude does not exceed the maximum acceleration output of the propulsion system

$$a^2(t) = a_x^2(t) + a_y^2(t) \leq \left(\frac{F_{\mathrm{max}}}{m}\right)^2 \qquad \forall\ t \in [0, t_{\mathrm{p},1}] \tag{3.40}$$

From the set profiles for $a_x(t)$ and $a_y(t)$

$$a^2(t) = a_1^2 \left(1 - \frac{t}{t_{\mathrm{p},1}}\right)^{2n} + \frac{a_1^4 t_{\mathrm{p},1}^4}{(n+1)^4 r_{\mathrm{d}}^2} \left[1 - \left(1 - \frac{t}{t_{\mathrm{p},1}}\right)^{n+1}\right]^4 \tag{3.41}$$

To find the maximum acceleration magnitude, the critical points need to be solved for from

$$\frac{d}{dt} a^2(t) = 0 \tag{3.42}$$

where

$$\frac{d}{dt}a^2(t) = -\frac{2na_1^2}{t_{\mathrm{p},1}}\left(1-\frac{t}{t_{\mathrm{p},1}}\right)^{2n-1} + \frac{4a_1^4t_{\mathrm{p},1}^3}{(n+1)^3r_{\mathrm{d}}^2}\left(1-\frac{t}{t_{\mathrm{p},1}}\right)^{n}\left[1-\left(1-\frac{t}{t_{\mathrm{p},1}}\right)^{n+1}\right]^3 \tag{3.43}$$

Acknowledging that a critical point exists for $t = t_{\mathrm{p},1}$, then the remaining critical points can be found by solving

$$\left(1-\frac{t}{t_{\mathrm{p},1}}\right)^{n-1} = \frac{2a_1^2t_{\mathrm{p},1}^4}{n(n+1)^3r_{\mathrm{d}}^2}\left[1-\left(1-\frac{t}{t_{\mathrm{p},1}}\right)^{n+1}\right]^3 \tag{3.44}$$

Using the substitutions

$$u = 1-\frac{t}{t_{\mathrm{p},1}} \qquad \text{and} \qquad A = \frac{2a_1^2t_{\mathrm{p},1}^4}{n(n+1)^3r_{\mathrm{d}}^2} \tag{3.45}$$

then Eq. 3.44 can be written as

$$u^{n-1} = A\left[1-u^{n+1}\right]^3 \tag{3.46}$$

There exists exactly one solution to this equation for the range $0 < u < 1$ since on this range the left-hand side is monotonically increasing from 0 to 1 and the right-hand side is monotonically decreasing from A to 0. Therefore, on the range $0 < t < t_{\mathrm{p},1}$ there is only a single critical point. Furthermore,

$$\frac{d}{dt}a^2(0) = -\frac{2na_1^2}{t_{\mathrm{p},1}} < 0 \tag{3.47}$$

which indicates that the critical point cannot be a maxima. If it were a maxima, then just before the critical point the acceleration magnitude must be increasing. However, for this to be possible, a local minima must have occurred earlier on in the profile since the acceleration magnitude is initially decreasing. If this were the case, then the maxima is at least the second critical point. Since there can only exist a single critical point, no local maxima can exist.

Since there are no local maxima on the range $0 < t < t_{\mathrm{p},1}$, then the maximum acceleration magnitude of the profile occurs on the boundary: either $t = 0$ or at $t = t_{\mathrm{p},1}$. The maximum acceleration is therefore

$$\max\left(\sqrt{a^2(t)}\right) = a_1 \qquad \text{or} \qquad \max\left(\sqrt{a^2(t)}\right) = \Omega_{\mathrm{d}}^2 r_{\mathrm{d}} \tag{3.48}$$

By design, it has to be that

$$\Omega_{\mathrm{d}}^2 r_{\mathrm{d}} \leq \frac{F_{\max}}{m} \tag{3.49}$$

otherwise the spacecraft would not be able to maintain the desired circular orbit. Therefore, the trajectory can be correctly sized by setting

$$a_1 = \frac{F_{\max}}{m} \tag{3.50}$$

Combining Eq. 3.50 with Eq. 3.39, then the total time of the maneuver profile is also set as

$$t_{\mathrm{p},1} = \frac{(n+1) r_{\mathrm{d}} \Omega_{\mathrm{d}}}{F_{\max}/m} \tag{3.51}$$

The last remaining state to be solved for is the angular position of the spacecraft in the orbital plane over time. The change in angular position is

$$\Delta\theta(t) = \int_0^t \Omega(\tau) d\tau \tag{3.52}$$

$$= -\frac{a_1 t_{p,1}^2}{(n+1) r_{\mathrm{d}}} \left(\frac{1}{n+2} \left[1 - \left(1 - \frac{t}{t_{p,1}} \right)^{n+2} \right] - \frac{t}{t_{p,1}} \right) \tag{3.53}$$

which gives a total angular change of the spacecraft over the course of the maneuver of

$$\Delta\theta(t_{p,1}) = \frac{a_1 t_{p,1}^2}{(n+2) r_{\mathrm{d}}} = \frac{(n+1)^2}{n+2} \frac{\Omega_{\mathrm{d}}^2 r_{\mathrm{d}}}{F_{\max}/m} \tag{3.54}$$

3.4.2 Changing Orbital Radius

Once the spacecraft is on the desired circular orbit, it needs to be able to change the radius of the circular orbit in order to enable point-to-point maneuvering. The ability to change the orbit's radius could also be used to land on or dock to a rotating target by slowly lowering the orbit's radius until it matches the radius of the central target.

The changing-radius maneuver can be designed starting from the dynamics given by Eqs.

3.23 and 3.24, and assuming that the frequency of the rotating frame is held constant at some desired value, Ω_{d}, throughout the maneuver. This result in the dynamics

$$0 = 2\Omega_{\mathrm{d}}\dot{y}(t) + a_x(t) \tag{3.55}$$

$$\ddot{y}(t) = \Omega_{\mathrm{d}}^2 y(t) + a_y(t) \tag{3.56}$$

For this maneuver, the strategy is to pick $a_y(t)$ in order to drive $y(t)$, the radius of the orbit, from the initial radius to the desired radius. Once $y(t)$ has been solved for, the required profile for $a_x(t)$ can be solved for from Eq. 3.55, which will hold the frequency of the orbit constant throughout the maneuver.

Consider a profile for $a_y(t)$ of the form

$$a_y(t) = -\Omega_{\mathrm{d}}^2 y(t) + a_2 t(t - t_{\mathrm{p},2})(t - 0.5t_{\mathrm{p},2}) \tag{3.57}$$

where a_2 is a constant and $t_{\mathrm{p},2}$ is the overall time of the maneuver. With this profile, the radial dynamics become

$$\ddot{y}(t) = a_2 t(t - t_{\mathrm{p},2})(t - 0.5t_{\mathrm{p},2}) \tag{3.58}$$

which results in a radial velocity of

$$\dot{y}(t) = \int_0^t \ddot{y}(\tau)d\tau \tag{3.59}$$

$$= \frac{1}{4}a_2 t^2 \left(t - t_{\mathrm{p},2}\right)^2 \tag{3.60}$$

and a radial position of

$$y(t) = y(0) + \int_0^t \dot{y}(\tau)d\tau \tag{3.61}$$

$$= y(0) + \frac{1}{120}a_2 t^3 \left(6t^2 - 15t_{\mathrm{p},2}t + 10t_{\mathrm{p},2}^2\right) \tag{3.62}$$

Therefore, for a desired change in radius, Δr, the parameters a_2 and $t_{\mathrm{p},2}$ need to be set such that

$$a_2 t_{\mathrm{p},2}^5 = 120\Delta r \tag{3.63}$$

The acceleration profile along each axis is then

$$a_x(t) = -2\Omega_\mathrm{d}\dot{y}(t) \tag{3.64}$$

$$= -\frac{1}{2}a_2\Omega_\mathrm{d}t^2(t - t_{\mathrm{p},2})^2 \tag{3.65}$$

and

$$a_y(t) = -\Omega_\mathrm{d}^2 y(t) + a_2 t(t - t_{\mathrm{p},2})(t - 0.5t_{\mathrm{p},2}) \tag{3.66}$$

$$= -\Omega_\mathrm{d}^2\left[y_0 + \frac{a_2}{120}t^3\left(6t^2 - 15t_{\mathrm{p},2}t + 10t_{\mathrm{p},2}^2\right)\right] + a_2 t(t - t_{\mathrm{p},2})(t - 0.5t_{\mathrm{p},2}) \tag{3.67}$$

where y_0 is the initial orbital radius. At the boundaries of the trajectory it is quite clear from Eqs. 3.65 and 3.67 that $a_x(0) = a_x(t_{\mathrm{p},2}) = 0$, $a_y(0) = -\Omega_\mathrm{d}^2 y_0$, and $a_y(t_{\mathrm{p},2}) = -\Omega_\mathrm{d}^2(y_0 + \Delta r)$ which indicate that the spacecraft will have a nadir-pointing attitude at the beginning and end of the trajectory. The derivative of the acceleration along the x axis is,

$$\dot{a}_x(t) = -2a_2\Omega_\mathrm{d}t(t - t_{\mathrm{p},2})(t - 0.5t_{\mathrm{p},2}) \tag{3.68}$$

which gives $a_x(0) = a_x(t_{\mathrm{p},2}) = 0$ and indicates that the spacecraft will have zero rotational velocity in the rotating frame at the beginning and end of the trajectory.

As with the joining-orbit maneuver, the acceleration profile should be further constrained such that the maximum acceleration magnitude required for the profile is less than the maximum acceleration output of the propulsion system. This would amount to finding the critical points of the acceleration magnitude by solving

$$\frac{d}{dt}(a_x^2(t) + a_y^2(t)) = 0 \tag{3.69}$$

To the author's knowledge, these critical points cannot be solved for analytically. Therefore, an alternative approach to bounding the maximum acceleration magnitude is used. The maximum magnitude of the acceleration along the x axis is

$$\max_{t\in[0,t_{\mathrm{p},2}]}\left|-\frac{1}{2}a_2\Omega_\mathrm{d}t^2(t - t_{\mathrm{p},2})^2\right| = \frac{1}{32}\Omega_\mathrm{d}|a_2|t_{\mathrm{p},2}^4 \tag{3.70}$$

The acceleration along the y axis can be broken into two components. The first is the centripetal acceleration which has a maximum magnitude of

$$\max_{t\in[0,t_{\mathrm{p},2}]} |a_{y,\mathrm{centripetal}}| = \Omega_{\mathrm{d}}^2 \max(y_0, y_0 + \Delta r) \tag{3.71}$$

The second component is the cubic function added on-top of the centripetal acceleration in order to change the orbit's radius. This component has a maximum magnitude of

$$\max_{t\in[0,t_{\mathrm{p},2}]} |a_2 t(t - t_{\mathrm{p},2})(t - 0.5t_{\mathrm{p},2})| = \frac{1}{12\sqrt{3}}|a_2| t_{\mathrm{p},2}^3 \tag{3.72}$$

Therefore, the maximum magnitude of the acceleration is bounded by

$$\max_{t\in[0,t_{\mathrm{p},2}]} \sqrt{a_x^2(t) + a_y^2(t)} \leq \frac{1}{32}\Omega_{\mathrm{d}}|a_2| t_{\mathrm{p},2}^4 + \Omega_{\mathrm{d}}^2 \max(y_0, y_0 + \Delta r) + \frac{1}{12\sqrt{3}}|a_2| t_{\mathrm{p},2}^3 \tag{3.73}$$

which means that by setting

$$\frac{1}{32}\Omega_{\mathrm{d}}|a_2| t_{\mathrm{p},2}^4 + \Omega_{\mathrm{d}}^2 \max(y_0, y_0 + \Delta r) + \frac{1}{12\sqrt{3}}|a_2| t_{\mathrm{p},2}^3 = \frac{F_{\max}}{m} \tag{3.74}$$

the maximum acceleration required for the maneuver will be guaranteed to be lower than the maximum acceleration output of the propulsion system. From Eq. 3.63 it must be that

$$|a_2| = \frac{120|\Delta r|}{t_{\mathrm{p},2}^5} \tag{3.75}$$

which when substituted into Eq. 3.74 results in a profile time of

$$t_{\mathrm{p},2} = \frac{\frac{15}{4}\Omega_{\mathrm{d}}|\Delta r| + \sqrt{\frac{225}{16}\Omega_{\mathrm{d}}^2 \Delta r^2 + \frac{40}{\sqrt{3}}\left[F_{\max}/m - \Omega_{\mathrm{d}}^2 \max(y_0, y_0 + \Delta r)\right]|\Delta r|}}{2\left[F_{\max}/m - \Omega_{\mathrm{d}}^2 \max(y_0, y_0 + \Delta r)\right]} \tag{3.76}$$

While this profile time does guarantee that the maximum acceleration required will be within the capabilities of the propulsion system, it is possible for $a_y(t) > 0$ during some parts of the maneuver. In those cases the plume of the propulsion system starts to be directed radially inwards, towards the target. The fact that $a_y(t) > 0$ for some range of the maneuver does not necessarily mean that plume impingement will occur, but without any bound on the value of $a_y(t)$ it cannot be guaranteed that plume impingement will be avoided. For this reason, it is worth developing an alternative setting of the parameters a_2 and $t_{\mathrm{p},2}$ in order to bound $a_y(t)$. The most convenient bound is to ensure that $a_y(t) \leq 0$ for the entire maneuver and develop guarantees for avoiding plume impingement based on this constraint. Such a bound will also match the characteristics of the joining-orbit maneuver where $a_y(t) \leq 0$ for the entire trajectory.

A simple way to guarantee $a_y(t) \leq 0$ is to ensure that the maximum magnitude of the cubic portion of $a_y(t)$ does not exceed the minimum value of the centripetal portion

$$\max_{t\in[0,t_{\mathrm{p},2}]} |a_2 t(t - t_{\mathrm{p},2})(t - 0.5t_{\mathrm{p},2})| \leq \min_{t\in[0,t_{\mathrm{p},2}]} |a_{y,\mathrm{centripetal}}| \tag{3.77}$$

which can be ensured by solving

$$\frac{1}{12\sqrt{3}}|a_2|t_{\mathrm{p},2}^3 \leq \Omega_{\mathrm{d}}^2 \min(y_0, y_0 + \Delta r) \tag{3.78}$$

Solving for the resulting profile time gives

$$t_{\mathrm{p},2} = \sqrt{\frac{10|\Delta r|}{\sqrt{3}\Omega_{\mathrm{d}}^2 \min(y_0, y_0 + \Delta r)}} \tag{3.79}$$

Given the two possible settings for the profile time from Eqs. 3.76 and 3.79, the larger of the two possible profile times is selected for a given scenario. This ensures that the maximum acceleration of the propulsion system will not be exceeded and that the radial acceleration will never be positive. In most cases Eq. 3.79 will constrain the profile time, however in cases where

$$F_{\max}/m \approx \Omega_{\mathrm{d}}^2 \max(y_0, y_0 + \Delta r) \tag{3.80}$$

then Eq. 3.76 will be the applicable constraint.

3.4.3 Changing Orbital Frequency

Changing the orbit's rotational frequency is similar to joining the orbit from rest, only that the spacecraft initial starts on the circular orbit. Starting from the dynamics given by Eqs. 3.23 and 3.24 then the goal is to pick a profile for $a_x(t)$ to drive the frequency of the orbit from some initial frequency, Ω_0, to a desired frequency, Ω_{d}, while maintaining a constant radius of r_{d}. Since the spacecraft starts and ends on a circular orbit, the profile must have a nadir-pointing attitude at the beginning and end of the trajectory. The radial acceleration at the beginning and end of the trajectory is known, $a_y(0) = -\Omega_0^2 r_\mathrm{d}$ and $a_y(t_{\mathrm{p},3}) = -\Omega_\mathrm{d}^2 r_\mathrm{d}$ where $t_{\mathrm{p},3}$ is the overall length of the maneuver. Therefore, to ensure a nadir-pointing attitude it must be that $a_x(0) = a_x(t_{\mathrm{p},3}) = 0$. In addition, to ensure that the spacecraft will have zero rotational velocity in the rotating frame at the beginning and end of the trajectory it must be that $\dot{a}_x(0) = \dot{a}_x(t_{\mathrm{p},3}) = 0$. All of this can be accomplished with a quartic profile

$$a_x(t) = -a_3 t^2 (t - t_{\mathrm{p},3})^2 \tag{3.81}$$

where a_3 is a constant. From inspection it is clear that $a_x(0) = a_x(t_{\mathrm{p},3}) = 0$. The time derivative of the x-axis acceleration is

$$\dot{a}_x(t) = -2a_3 t (t - t_{\mathrm{p},3})^2 - 2a_3 t^2 (t - t_{\mathrm{p},3}) \tag{3.82}$$

Again, from inspection it is clear that $\dot{a}_x(0) = \dot{a}_x(t_{\mathrm{p},3}) = 0$.

With the quartic profile for $a_x(t)$, the change in orbit frequency is given by

$$\begin{aligned} \Delta\Omega(t) &= -\frac{1}{r_\mathrm{d}} \int_0^t a_x(\tau) d\tau && (3.83) \\ &= \frac{a_3 t^3}{30 r_\mathrm{d}} \left(6t^2 - 15 t t_{\mathrm{p},3} + 10 t_{\mathrm{p},3}^2\right) && (3.84) \end{aligned}$$

which gives a total change in orbit frequency over the entire maneuver of

$$\Delta\Omega(t_{\mathrm{p},3}) = \frac{1}{30} \frac{a_3 t_{\mathrm{p},3}^5}{r_\mathrm{d}} \tag{3.85}$$

Therefore, for a given initial frequency of Ω_0 and a final frequency of Ω_d, the parameters a_3 and $t_{\mathrm{p},3}$ must be selected in order to satisfy

$$a_3 t_{\mathrm{p},3}^5 = 30 r_\mathrm{d} (\Omega_\mathrm{d} - \Omega_0) \tag{3.86}$$

The profile for $a_y(t)$ can then be solved for from Eq. 3.24 as

$$a_y(t) = -r_\mathrm{d} \left[\Omega_0 + \frac{a_3 t^3}{30 r_\mathrm{d}} \left(6t^2 - 15 t t_{\mathrm{p},3} + 10 t_{\mathrm{p},3}^2\right)\right]^2 \tag{3.87}$$

As before, the final constraint on the maneuver parameters is to ensure that the maximum magnitude of the acceleration is within the propulsion system's capabilities. The square of the total acceleration magnitude is

$$\begin{aligned} a^2(t) &= a_x^2(t) + a_y^2(t) && (3.88) \\ &= a_3^2 t^4 (t - t_{\mathrm{p},3})^4 + r_\mathrm{d}^2 \left[\Omega_0 + \frac{a_3 t^3}{30 r_\mathrm{d}} \left(6t^2 - 15 t t_{\mathrm{p},3} + 10 t_{\mathrm{p},3}^2 \right) \right]^4 && (3.89) \end{aligned}$$

Taking its time derivative to solve for the critical points gives

$$\begin{aligned} \frac{d}{dt} a^2(t) = 4a_3^2 t^3 (t - t_{\mathrm{p},3})^4 + 4a_3^2 t^4 (t - t_{\mathrm{p},3})^3 \\ + 4 a_3 r_\mathrm{d} t^2 (t - t_{\mathrm{p},3})^2 \left[\Omega_0 + \frac{a_3 t^3}{30 r_\mathrm{d}} \left(6t^2 - 15 t t_{\mathrm{p},3} + 10 t_{\mathrm{p},3}^2 \right) \right]^3 \quad (3.90) \end{aligned}$$

Acknowledging the two critical points at $t = 0$ and two further critical points at $t = t_{\mathrm{p},3}$, then the remaining critical points can be found by solving

$$a_3 t (t - t_{\mathrm{p},3})(2t - t_{\mathrm{p},3}) = -r_\mathrm{d} \left[\Omega_0 + \frac{a_3 t^3}{30 r_\mathrm{d}} \left(6t^2 - 15 t t_{\mathrm{p},3} + 10 t_{\mathrm{p},3}^2 \right) \right]^3 \quad (3.91)$$

As with the orbital radius change, an analytical expression for the remaining critical points of the overall acceleration magnitude could not be found. However, the right-hand side of Eq. 3.91 is simply $-r_\mathrm{d}\Omega^3(t)$ which is bounded by $-r_\mathrm{d}\Omega_0^3$ and $-r_\mathrm{d}\Omega_\mathrm{d}^3$, and the left-hand side is a cubic function with roots at $t = 0$, $t = 0.5t_{\mathrm{p},3}$ and $t = t_{\mathrm{p},3}$. The maximum magnitude of the left-hand side is

$$\max_{t \in [0, t_{\mathrm{p},3}]} |a_3 t (t - t_{\mathrm{p},3})(2t - t_{\mathrm{p},3})| = \frac{1}{6\sqrt{3}} a_3 t_{\mathrm{p},3}^3 \quad (3.92)$$

If the maneuver is designed such that there are no solutions to Eq. 3.91, then there cannot be any local maxima on the range $t \in (0, t_{\mathrm{p},3})$ and the maximum acceleration magnitude will occur either at $t = 0$ or $t = t_{\mathrm{p},3}$. One simple way of ensuring this is to set

$$\frac{1}{6\sqrt{3}} a_3 t_{\mathrm{p},3}^3 < r_\mathrm{d} \min\left(\Omega_0^3, \Omega_\mathrm{d}^3 \right) \quad (3.93)$$

However, this bound is quite conservative, and better bounds can be found. Note from Eq. 3.86 that $a_3 > 0$ when $\Omega_\mathrm{d} > \Omega_0$. In Eq. 3.91, if $a_3 > 0$ then the left-hand side will be positive for $t \in (0, 0.5t_{\mathrm{p},3})$ and negative for $t \in (0.5t_{\mathrm{p},3}, t_{\mathrm{p},3})$. The right-hand side of Eq. 3.91 will always be negative since it is equal to $-r_\mathrm{d}\Omega^3(t)$ and the problem is constructed such that $\Omega(t) > 0$. Therefore, the only portion of the profile where it is possible for Eq. 3.91 to have any solutions is on the range $t \in (0.5t_{\mathrm{p},3}, t_{\mathrm{p},3})$. Similarly, from Eq. 3.86, $a_3 < 0$ when $\Omega_{\mathrm{d}} < \Omega_0$. In this case, the left-hand side of Eq. 3.91 will be negative for $t \in (0, 0.5t_{\mathrm{p},3})$ and positive for $t \in (0.5t_{\mathrm{p},3}, t_{\mathrm{p},3})$. Therefore, the only portion of the profile where it is possible for Eq. 3.91 to have any solutions is on the range $t \in (0, 0.5t_{\mathrm{p},3})$.

This situation is shown graphically in Figure 3-4 for arbitrary maneuver parameters. When $\Omega_{\mathrm{d}} > \Omega_0$ both sides of Eq. 3.91 have the same sign when $t \in (0.5t_{\mathrm{p},3}, t_{\mathrm{p},3})$, and when $\Omega_{\mathrm{d}} < \Omega_0$ both sides of Eq. 3.91 have the same sign when $t \in (0, 0.5t_{\mathrm{p},3})$. The byproduct of this result is that better bounds than that of Eq. 3.93 can be found in order to ensure that Eq. 3.91 does not have any solutions. In particular, note that whenever both sides of Eq. 3.91 share the same sign, the magnitude of the right-hand side is always larger than what it is at $t = 0.5t_{\mathrm{p},3}$. Therefore, by setting

$$\frac{1}{6\sqrt{3}} a_3 t_{\mathrm{p},3}^3 = -r_{\mathrm{d}} \Omega^3(t_{\mathrm{p},3}/2) \tag{3.94}$$

it can be guaranteed that Eq. 3.91 does not have any solutions which in turn guarantees that there are no local maxima for the total acceleration magnitude on the range $t \in (0, t_{\mathrm{p},3})$. Based on the derived profile for $\Omega(t)$

$$\Omega(t_{\mathrm{p},3}/2) = (\Omega_0 + \Omega_d)/2 \tag{3.95}$$

Combining this result with Eq. 3.86 gives the parameter settings

$$a_3 = \frac{9}{160} \frac{r_{\mathrm{d}}(\Omega_{\mathrm{d}} + \Omega_0)}{\Omega_{\mathrm{d}} - \Omega_0} \left[\frac{1600}{3} \frac{(\Omega_{\mathrm{d}} - \Omega_0)^2}{(\Omega_{\mathrm{d}} + \Omega_0)^6} \right]^{-1/4} \tag{3.96}$$

and

$$t_{\mathrm{p},3} = \left[\frac{1600}{3} \frac{(\Omega_{\mathrm{d}} - \Omega_0)^2}{(\Omega_{\mathrm{d}} + \Omega_0)^6} \right]^{1/4} \tag{3.97}$$

which guarantee that

$$\max_{t \in [0, t_{\mathrm{p},3}]} a(t) = r_{\mathrm{d}} \max\left(\Omega_0^2, \Omega_{\mathrm{d}}^2\right) \tag{3.98}$$

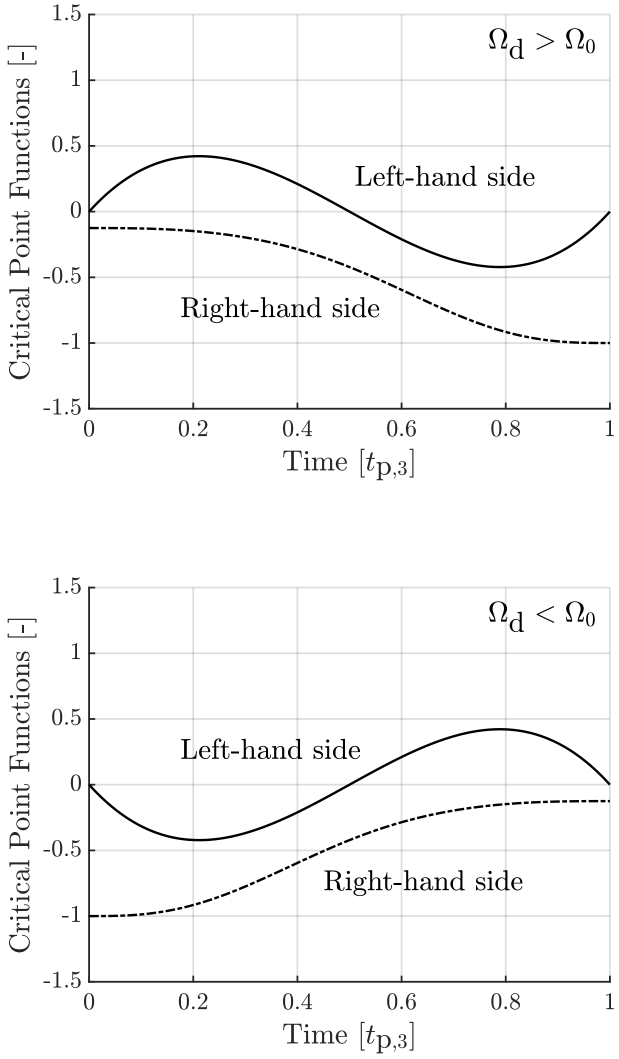

Figure 3-4: Graphical representation of functions for determining the critical points of the changing-frequency maneuver.

Finally, the angular position of the spacecraft throughout the maneuver is given by

$$\Delta\theta(t) = \int_0^t \Omega(\tau) d\tau \tag{3.99}$$

$$= \Omega_0 t_{\mathrm{p},3} + \frac{1}{60}\frac{a_3 t^4}{r_{\mathrm{d}}}\left(2t^2 - 6t_{\mathrm{p},3}t + 5t_{\mathrm{p},3}^2\right) \tag{3.100}$$

which gives an overall angular change of the spacecraft for the maneuver of

$$\Delta\theta(t_{\mathrm{p},3}) = \frac{1}{2}t_{\mathrm{p},3}(\Omega_0 + \Omega_{\mathrm{d}}) \tag{3.101}$$

3.4.4 Changing Orbital Plane

Changing the orbital plane could have two different goals. The first would be to rotate the orbital plan around some axis, analogous to an inclination change in orbital dynamics. The second is to translate the orbital plane along its normal vector. Rotating the orbital plane is most-easily accomplished by leaving the current circular orbit at the intersection point between the current orbital plane and the desired orbital plan (the ascending or descending node) and then joining a new circular orbit in the desired orbital plane. Translating the orbital plane cannot be accomplished as easily and requires a separate maneuver.

Conveniently, in the chosen coordinate system the z-axis dynamics are decoupled from the in-plane dynamics

$$\ddot{z}(t) = a_z(t) \tag{3.102}$$

In order to ensure that the spacecraft's attitude is nadir-pointing and that the rotational velocity of the spacecraft in the rotating frame is zero at the beginning and end of the trajectory, it must be that $a_z(0) = a_z(t_{\mathrm{p},4}) = 0$ and $\dot{a}_z(0) = \dot{a}_z(t_{\mathrm{p},4}) = 0$ where $t_{\mathrm{p},4}$ is the overall time of the maneuver profile. An additional requirement of $\dot{z}(0) = \dot{z}(t_{\mathrm{p},4}) = 0$ is needed to ensure dynamic consistency for the z-axis motion of the spacecraft. All of this can be accomplished with a quintic acceleration profile

$$a_z(t) = -a_4 t^2 (t - t_{\mathrm{p},4})^2 (t - 0.5t_{\mathrm{p},4}) \tag{3.103}$$

where a_4 is a constant. From inspection it can be seen that $a_z(0) = a_z(t_{\mathrm{p},4}) = 0$. The time derivative of the z-axis acceleration is

$$\dot{a}_z(t) = -2a_4 t(t - t_{\mathrm{p},4})^2(t - 0.5t_{\mathrm{p},4}) - 2a_4 t^2(t - t_{\mathrm{p},4})(t - 0.5t_{\mathrm{p},4}) - a_4 t^2(t - t_{\mathrm{p},4})^2 \tag{3.104}$$

Again, from inspection in can be seen that $\dot{a}_z(0) = \dot{a}_z(t_{\mathrm{p},4}) = 0$.

The chosen acceleration profile results in a z-axis velocity of

$$\begin{aligned} \dot{z}(t) &= \int_0^t a_z(\tau)d\tau && (3.105) \\ &= -\frac{1}{6}a_4 t^3(t^3 - 3t_{\mathrm{p},4}t^2 + 3t_{\mathrm{p},4}^2 t - t_{\mathrm{p},4}^3) && (3.106) \end{aligned}$$

which demonstrates that $\dot{z}(0) = \dot{z}(t_{\mathrm{p},4}) = 0$. The change in z-axis position is

$$\begin{aligned} \Delta z(t) &= \int_0^t \dot{z}(\tau)d\tau && (3.107) \\ &= -\frac{1}{840}a_4 t^4(20t^3 - 70t_{\mathrm{p},4}t^2 + 84t_{\mathrm{p},4}^2 t - 35t_{\mathrm{p},4}^3) && (3.108) \end{aligned}$$

The parameters a_4 and $t_{\mathrm{p},4}$ need to be selected in order to change the spacecraft's z-axis position by a desired amount, $\Delta z(t_{\mathrm{p},4}) = \Delta z_{\mathrm{d}}$

$$\Delta z(t_{\mathrm{p},4}) = \frac{1}{840}a_4 t_{\mathrm{p},4}^7 \tag{3.109}$$

which places the requirement that

$$a_4 t_{\mathrm{p},4}^7 = 840\Delta z_{\mathrm{d}} \tag{3.110}$$

The maximum magnitude acceleration can be analytically solved for. The maximum magnitude of the z-axis acceleration is

$$\max_{t\in[0,t_{\mathrm{p},4}]} |a_z(t)| = \frac{1}{50\sqrt{5}}a_4 t_{\mathrm{p},4}^5 \tag{3.111}$$

while the acceleration in the x-y plane is held constant at $\Omega_{\mathrm{d}}^2 r_{\mathrm{d}}$. Therefore, the maximum magnitude of the acceleration can be correctly constrained by solving

$$\Omega_{\mathrm{d}}^4 r_{\mathrm{d}}^2 + \frac{1}{12500}a_4^2 t_{\mathrm{p},4}^{10} = (F_{\max}/m)^2 \tag{3.112}$$

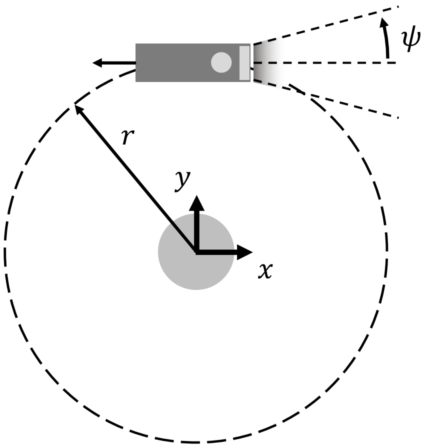

Figure 3-5: Worst-case scenario for plume impingement where the radial component of the acceleration vector is zero.

which results in a profile time of

$$t_{\mathrm{p},4} = \sqrt{\frac{84}{5\sqrt{5}}}\left[\frac{\Delta z_{\mathrm{d}}^{2}}{(F_{\mathrm{max}}/m)^{2} - \Omega_{\mathrm{d}}^{4} r_{\mathrm{d}}^{2}}\right]^{1/4} \tag{3.113}$$

3.5 Plume Impingement

All maneuvers were designed such that the radial component of the acceleration vector is never positive. This allows for guarantees regarding plume impingement to be developed. In the worst-case scenario, the radial component of the acceleration vector is zero, as it is at the very beginning of the joining-orbit maneuver. Figure 3-5 shows this scenario for a propulsion system that has a plume half-angle of ψ. Assuming that it is desired for the plume to never intersect a sphere of radius R around the target, then limits on the minimum radius that the spacecraft is allowed to operate in can be developed. This minimum radius can be solved for from geometry as

$$r_{\mathrm{min}} = \frac{R}{\cos\psi} \tag{3.114}$$

As long as the desired baseline circular orbit of the spacecraft has a radius of $r > r_{\mathrm{min}}$ and the sphere of radius R is appropriately selected in order to fully encompass the target (such as a circumscribing sphere), plume impingement will be avoided.

3.6 Example Applications

This section shows examples of the analytical maneuver library being used for basic mission segments. Specifically, point-to-point maneuvering between any two points in space is shown including situations where the central target is cylindrical and translating the orbit along its normal vector may be advantageous. In addition, the use of changing the orbit frequency and changing orbit radius is demonstrated for landing on or docking to a rotating target.

In all cases, the construction of the full maneuver from individual maneuvers in the library is the same. First, the necessary maneuvers are selected including the addition of a "coast" maneuver where the spacecraft simply maintains its current circular motion. The maneuvers are then stitched together at their boundaries in order to form the full maneuver and the "coast" maneuver is used in order to fill in any necessary gaps in angular position. Since all maneuvers, with the exception of joining or leaving the circular orbit, were designed to start and end with a nadir-pointing attitude and with zero rotational velocity in the rotating frame, stitching different maneuvers from the library together is as simple as ensuring that they have the same radial and angular position within the orbital plane.

3.6.1 Point-to-Point Maneuvering

Figure 3-6 shows an example of a basic point-to-point maneuver between two waypoints. The full maneuver is composed of joining the circular orbit, coasting, changing the orbital radius, and finally leaving the circular orbit. The ordering of coasting and changing orbital radius can change depending on if the end waypoint is at a greater or lower radius than the start waypoint. The acceleration required to maintain a circular orbit of a given frequency increases with orbit radius, so coasting should usually occur at as low of an orbital radius as possible. In the scenario in Figure 3-6 since the end waypoint is at a greater radius than the start waypoint, coasting is conducted before increasing the orbit radius.

Figure 3-7 shows the total acceleration magnitude throughout the maneuver. The acceleration magnitude stays within the capabilities of the propulsion system for the entire maneuver, and only reaches the maximum acceleration output of the propulsion system at the beginning of joining the circular orbit and at the end of leaving the circular orbit. Figure 3-8 shows the spacecraft's heading and rotational velocity in the rotating frame throughout the maneuver. At the boundaries between individual maneuvers, the spacecraft always

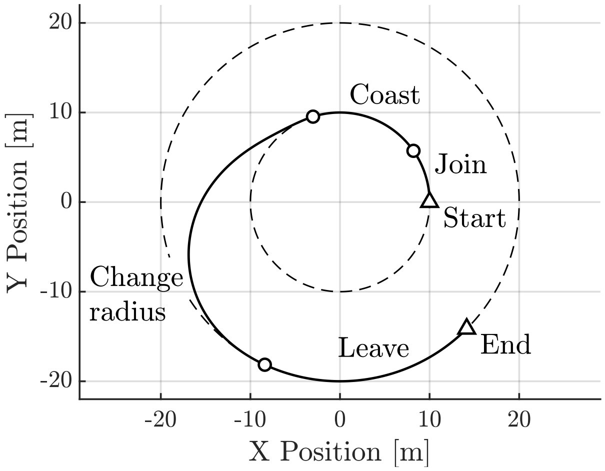

Figure 3-6: Basic point-to-point maneuver.

returns to a nadir-pointing attitude with zero rotational velocity which makes stitching together the individual maneuvers quite simple. In addition, the spacecraft's heading in the rotating frame always remains between ±90° which means that the spacecraft's thrust vector never points radially outwards.

Since the spacecraft's heading in the rotating frame remains between ±90°, the conditions under which plume impingement is guaranteed to be avoided can be determined based on Eq. 3.114. The lowest radius of the spacecraft is 10 m, the radius of the start waypoint, which means that for an assumed plume half-angle of 45°, Eq. 3.114 gives that the plume will never enter a sphere of radius 7.07 m around the central target. Figure 3-9 shows a plume impingement map for the maneuver. Regions on the map that would experience plume impingement at any point during the maneuver are shaded. Darker shading corresponds to regions that would experience plume impingement for a greater duration of time, while regions that are unshaded would not experience plume impingement at any point during the maneuver. Since the thrust vector of the propulsion system predominantly points towards the center, in order to provide the necessary centripetal acceleration, most of the shading is on regions that are radially outward from the spacecraft's trajectory. A circle of radius 7.07 m is marked on the plot, and it can be seen that the plume of the propulsion system does not enter this circle at any point during the maneuver.

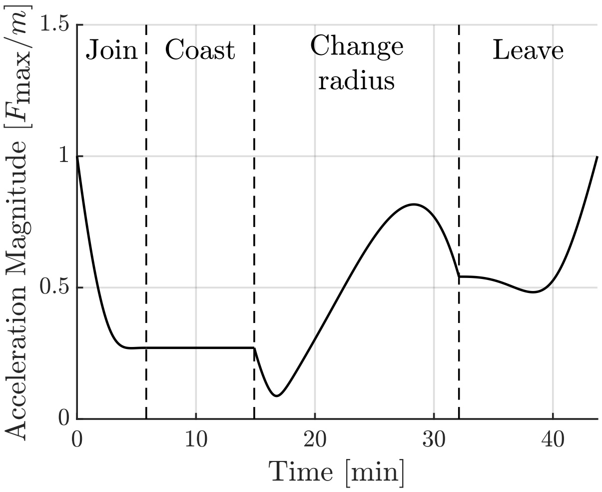

Figure 3-7: Total acceleration magnitude normalized by the maximum acceleration of the propulsion system throughout a basic point-to-point maneuver.

3.6.2 Cylindrical Point-to-Point Maneuvering

For cylindrical targets, such as the upper-stage of a booster, the use of the changing-height maneuver might be advantageous. Although passively-safe trajectories are not explicitly addressed in this work, around a more spherical target if the propulsion system of the spacecraft were to fail while the spacecraft is maintaining its circular motion, the spacecraft would simply drift away from the target with no risk of collision. Around a cylindrical target, if the normal vector of the orbit is not parallel to the long axis of the target, it is possible for the orbit to intersect the target. For this reason, it may be better to maintain circular orbits with their normal vector parallel to the long axis of the target, and use the changing-height maneuver to move along the target.

Figure 3-10 demonstrates one such application. Although it is possible to connect the start and end waypoints with a circular trajectory, the circle will end up intersecting the target, posing a potential collision risk. By using the changing-height maneuver, the spacecraft can move from the start waypoint to the end waypoint on an entirely passively-safe trajectory; if the propulsion system were to fail at any point of the trajectory, the spacecraft would drift away from the target with no risk of collision.

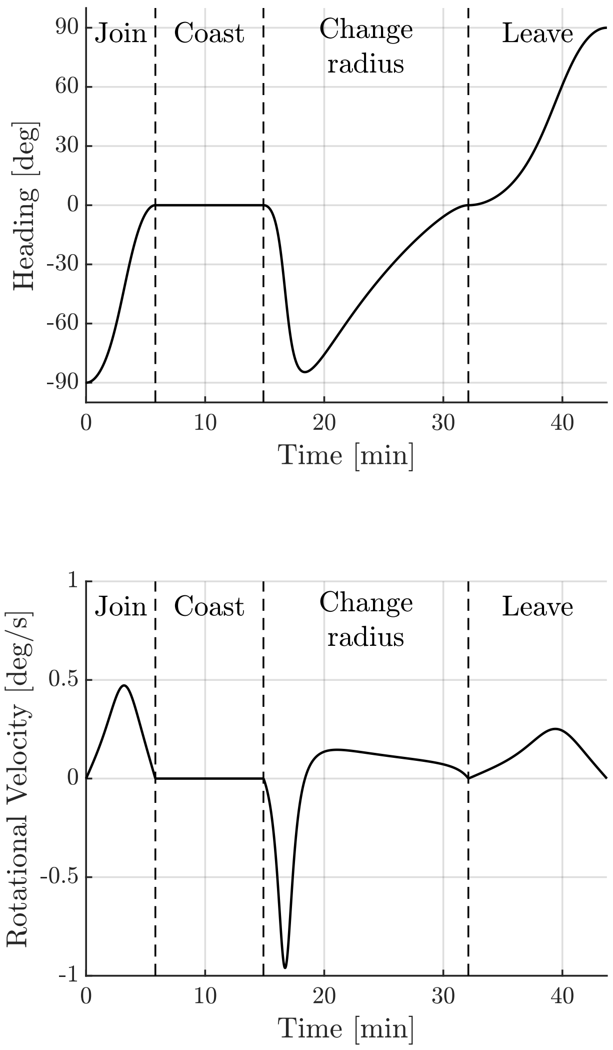

Figure 3-8: Heading and rotational velocity of the spacecraft in the rotating frame throughout a basic point-to-point maneuver.

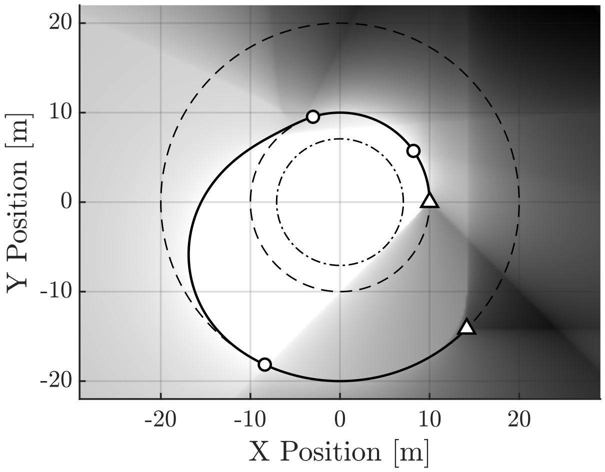

Figure 3-9: Plume impingement map throughout a basic point-to-point maneuver. Shaded regions are those that would experience plume impingement with darker regions corresponding the greater plume impingement.

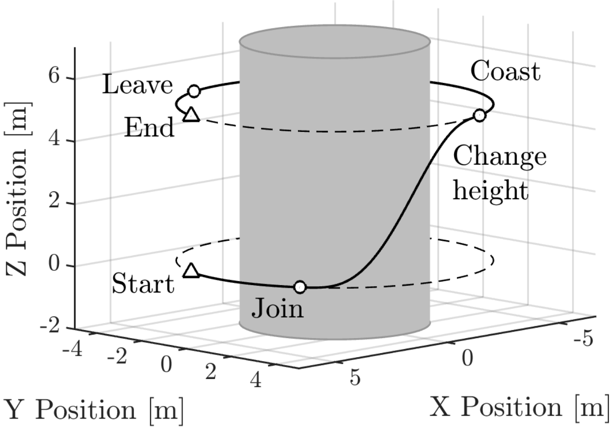

Figure 3-10: Basic point-to-point maneuvering around a cylindrical target.

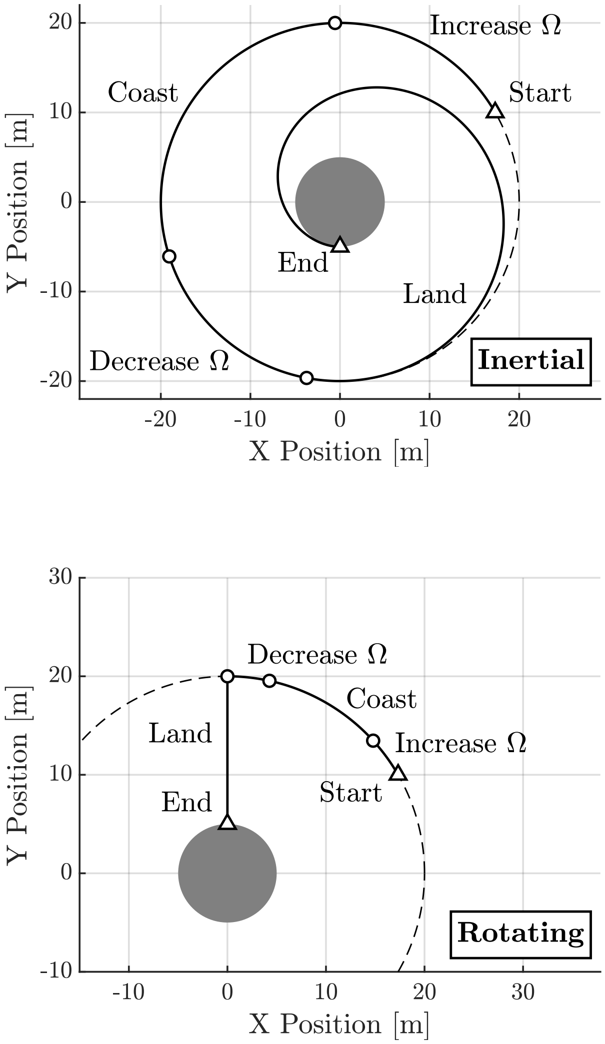

Figure 3-11: Landing on or docking to a rotating target in both the inertial and rotating frames. The rotating frame rotates with the target which is assumed to be in a flat spin.

3.6.3 Landing on/Docking to a Rotating Target

The changing orbital frequency and changing orbital radius maneuvers can be used to land on or dock to a rotating target in a flat spin. Figure 3-11 shows an example of such a maneuver in both the inertial frame and in a frame that rotates with the target. It is assumed that the spacecraft starts in a circular orbit with frequency equal to the rotational frequency of the target, such that in the rotating frame the spacecraft is initially stationary.

The spacecraft initially starts 30° behind its desired landing/docking point. Therefore, before landing it must first increase its own orbit frequency in order to catch up with the landing/docking point. This is conducted in three steps. First, the spacecraft increases its orbital frequency to some value larger than the target's rotational frequency. Next, the spacecraft coasts in order to allow itself to catch up with the desired landing/docking point. Finally, the spacecraft decreases its orbital frequency back down to the rotational frequency of the target such that it is hovering directly above the desired landing/docking point. At this point the spacecraft can lower its orbital radius such that it soft lands on/docks to the target. Since the maneuver for changing orbital radius was constrained to maintain a constant orbital frequency, the landing/docking maneuver appears as a straight line in the rotating frame.

Figure 3-12 shows the total acceleration magnitude throughout the maneuver. As intended, the acceleration magnitude remains within the capabilities of the propulsion system for the entire maneuver. Figure 3-13 shows the spacecraft's heading and rotational velocity in the rotating frame through the maneuver. Again, the spacecraft returns to a nadir-pointing attitude with zero rotational velocity in the rotating frame at the boundary between each segment of the maneuver. Finally, Figure 3-14 shows a plume impingement map in the rotating frame throughout the maneuver. Since the spacecraft's final orbital radius is equal to the radius of the target, there are no guarantees regarding plume impingement unless the propulsion system's plume has zero width. However, by increasing the profile time beyond those specified by Eqs. 3.76 and 3.79 plume impingement can still be avoided, as shown in Figure 3-14.

3.7 Conclusion

This work demonstrates that an underactuated spacecraft can be controlled with linear control methods and that an analytical maneuver library can be developed in order to maneuver the spacecraft around a central target without resorting to numerical optimization. In addition, constraints such as maximum acceleration magnitude as well as plume impingement can be directly embedded into the maneuver library. The maneuver library developed in this work is only one possible library that could be created. Other formulations for the basic trajectories, such as the use of trigonometric functions instead of polynomial functions, would allow for other libraries to be generated.

An analytical maneuver library could enable the use of high-efficiency but low-thrust propulsion systems, such as electrospray thrusters, for free-flying small spacecraft inspec-

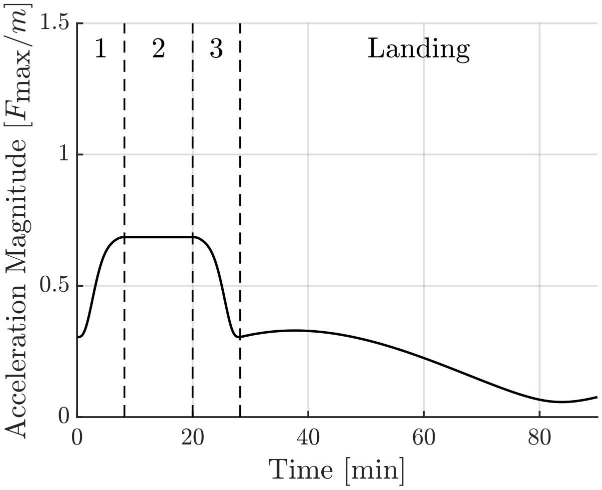

Figure 3-12: Total acceleration magnitude normalized by the maximum acceleration of the propulsion system throughout landing on or docking to a rotating target. Region 1 corresponds to increasing orbit frequency, region 2 corresponds to coasting, and region 3 corresponds to decreasing orbit frequency.

tors. Such spacecraft could be used for long-duration inspection of a target or a single spacecraft could be used to inspect multiple targets. While the maneuvers in the library are suboptimal, the degree of sub-optimality is marginal and the trajectories can be computed at a significantly lower computational cost relative to methods that require numerical optimization.

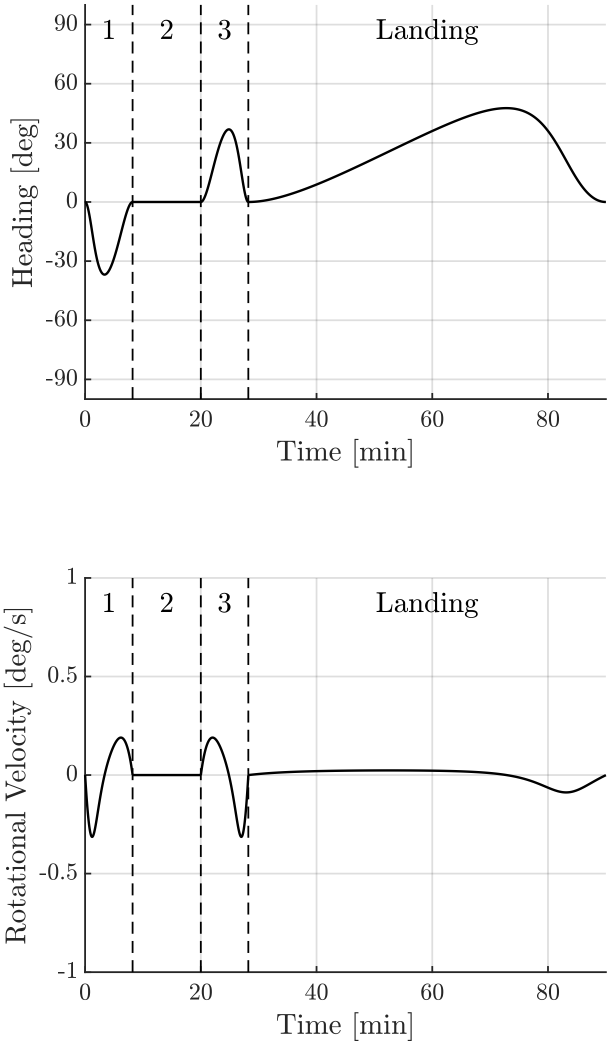

Figure 3-13: Heading and rotational velocity of the spacecraft in the rotating frame throughout landing on or docking to a rotating target. Region 1 corresponds to increasing orbit frequency, region 2 corresponds to coasting, and region 3 corresponds to decreasing orbit frequency.

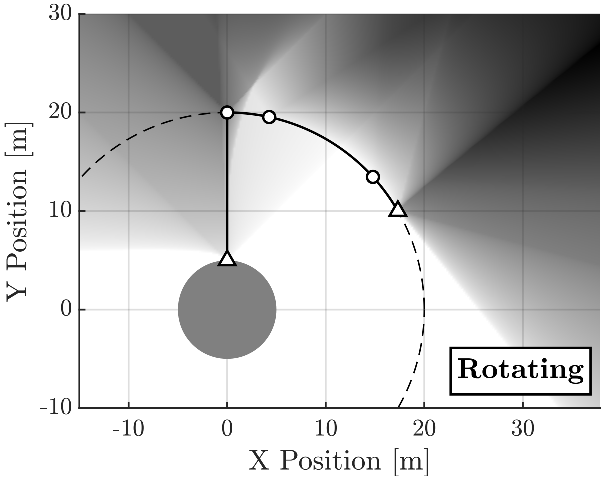

Figure 3-14: Plume impingement map throughout landing on or docking to a rotating target. Shaded regions are those that would experience plume impingement with darker regions corresponding the greater plume impingement.

Chapter 4

Surface Operations

Under most conditions, an electrically isolated surface exposed to a plasma will accumulate a negative charge. Assuming a Maxwellian distribution of the particles, the particle flux across a plane is given by

$$\Gamma = n\sqrt{\frac{kT}{2\pi m}} \tag{4.1}$$

where n is the particle number density, k is the Boltzmann constant, T is the temperature, and m is the particle mass. In a plasma, the number density of particles is near-equal for ions and electrons. The temperature of the ions may differ from the temperature of the electrons, but the main difference between the particle fluxes is that the mass of the ions is at least three orders of magnitude greater than the mass of the electrons. Therefore, more electrons will arrive at the surface than ions initially, charging the surface negatively. The surface will continue to charge negatively until the ion and electron fluxes are equal.

Asteroids, or any atmosphere-less planetary body, lack a strong charge dissipation mechanism. When exposed to a plasma, provided by the solar wind, the surface of the asteroid will charge. Complicating the picture is the possibility of photoelectric emission of electrons. Incoming photons, from the Sun, can excite electrons to the point that they are emitted from the surface [102]. The photoelectric emission of electrons charges surfaces positively and competes with the surface charging from the surrounding plasma. On the Sun-facing surfaces of atmosphere-less planetary bodies, the photoelectric emission is found to be dominant and the surfaces charge positively [103]. On the night-side of these bodies, due to the lack of photoelectric emission, the surface charges negatively.

An additional form of surface charging could be caused by ion bombardment. When bombarded with positive ions, a surface will lose electrons due to Auger neutralization of the incoming ions. The potential well created by the incoming ions allows electrons to escape from the surface and tunnel to the ion, neutralizing it. In addition to the electron lost for neutralization, further electrons can be lost as secondary emission due to potential ejection; as the neutralization electron tunnels to the incoming ion, it gives its extra energy to other electrons in the atom. It is possible for these other electrons to receive sufficient energy such that they are ejected from the surface. Kinetic ejection, where the kinetic energy from the incoming ion causes secondary emission, is also possible but is hypothesized to be less important than potential ejection [104]. This hypothesis is supported by the observation that secondary emission mostly depends on the ionization energy of the incoming ions and not their kinetic energy [105]. Negative ions cannot be neutralized from Auger neutralization but still deposit their charge and cause the emission of secondary electrons. It is likely that these processes are kinetic, at least for relatively high-energy ions.

For simple modeling, it is fairly safe to assume that incoming ions, whether positive or negative, will deposit their charge on the surface through some process. Secondary electrons will be emitted at some ratio depending on the various properties of the ions and the surface. For positive ion bombardment, since the surface will charge positively and secondary electrons have fairly low emission energies, the secondary electrons will be attracted back to the surface and not contribute to the overall charging allowing surfaces to charge close to the energy of the incoming ions [106]. However, for negative ion bombardment, since the surface will charge negatively, the secondary electrons will be repelled from the surface and attenuate the surface charging. The ratio of secondary electrons to incoming negative ions can exceed one and therefore prevent the surface from charging significantly. This observation has led to the proposal of using negative ion bombardment during various processes specifically to avoid surface charging [107].

As mentioned previously, the interaction between the surfaces of atmosphere-less planetary bodies, such as the Moon and asteroids, and the surrounding plasma and radiation environment can induce surface charging. Due to the low plasma density, this surface charging allows for electric fields extending up to tens of meters away from the surface. Analysis of the data from the Suprathermal Ion Detector Experiment on the Apollo missions [108] and the Electron Reflectometer from the Lunar Prospector mission [109] both confirm the presence of surface charging on the Moon and resulting electric fields on the order of 10 V/m. This electric field is large enough to levitate the regolith on the surface of the Moon, and the Surveyor landers observed $\sim$10 μm grains of dust levitating 10s of centimeters above the surface [110].

Although these experiments were conducted on the Moon, surface charging will occur on any planetary body without a sufficiently strong charge-dissipation mechanism such as an atmosphere or internal charge dissipation. Theoretical calculations predict surface electric fields on the order of 10-20 V/m on the Sun-facing surfaces of asteroids in the main asteroid belt [111]. It is believed that this surface charging is responsible for the transport of dust on atmosphere-less planetary bodies, which could explain phenomena such as the unusually smooth surface of Atlas [112], "ponds" of dust on Eros as seen by the NEAR Shoemaker mission [113], degradation of optical devices on the Moon [114], porosity on the surfaces of asteroids [115], and emission and redistribution of particles on the comet Churyumov-Gerasimenko [116, 117]

To support this theory, laboratory experiments have been able to demonstrate the electrostatic transportation of dust particles on dusty surfaces under ultraviolet illumination or exposure to plasmas [118]. Dust is observed to shed from a conductive sphere when exposed only to a plasma [119], but required a plasma and electron beam when the dust was placed on an insulating surface [120, 121]. Other experiments attempted to quantify the charging on dust particles when exposed to a plasma environment [122]. In experiments more representative of asteroid surfaces, shadow boundaries, like what might be seen at the terminator between the day and night sides of an asteroid, were found to increase dust transport [123], and the use of ultraviolet illumination in combination with an ambient plasma was found to induce dust charging and transport [124].

From the observation of the levitation of dust particles, an electrostatic glider concept was proposed in order to utilize this natural surface charging to provide maneuverability around a small asteroid [125] including hovering [126]. The electrostatic glider deploys Mylar wings in order to increase its capacitance such that electrostatic levitation can be achieved. However, the set of planetary bodies that can be explored with such a concept is limited to small asteroids due to the relatively low surface electric field. To resolve the issues associated with low natural surface charging and enable electric levitation on larger planetary bodies, this work proposes the use of ionic-liquid ion sources to charge the spacecraft body as well

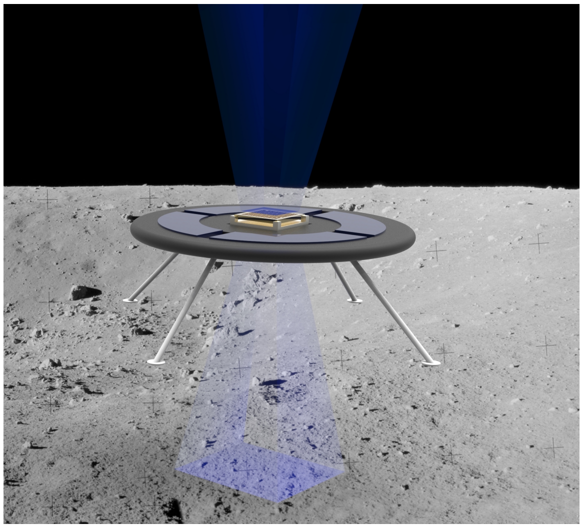

Figure 4-1: Concept image of an electrically-levitated rover on the surface of the Moon.

as to artificially increase the local surface charge of the planetary body's surface beyond the natural limit.

To artificially increase the charging of the planetary body's surface, an ionic-liquid ion source could be used to irradiate the surface with ions and increase the local surface charging. Such a strategy would allow for surface electric fields well in excess of the natural ∼10 V/m on the Sun-facing surface of the planetary body. In this concept, one ion source ejects negative ions upward from the vehicle to charge it positively while a second first positive ions downwards into the surface in order to charge the local surface positively and increase the local electric field. Additional sources, in the form of electrospray thrusters, could be included to provide translational maneuverability. Since electrospray thrusters are solid-state devices, such a system could allow for a vehicle that can achieve levitation and translational movement across and planetary body's surface with no moving parts. In addition, as the vehicle is levitating, it has no physical contact with the planetary body's surface, potentially allowing it to more easily explore uneven surfaces relative to traditional wheeled, legged, or hopping vehicles which struggle in such environments [127]. Figure 4-1 shows a concept image of such a rover.

4.1 Research Gap

Charging of space vehicles as a means of actuation has largely been ignored as most approaches have tried to minimize spacecraft charging during operations. However, recent studies linking natural surface charging to the transport of dust particles across the surfaces of atmosphere-less planetary bodies raises the question of if such an effect could be used for actuation of a small vehicle. Prior work has considered the use of an electrically-charged glider for proximity operations around small asteroids that leverages the natural surface charging. However, this approach is limited due to the relatively low magnitude of the natural surface charging. An alternative approach would be to supplement that natural surface charging through ion bombardment, but has yet to be analyzed in any form.

This work is an initial feasibility study on the use of ionic-liquid ion sources for electric actuation for a small vehicle on the surfaces of atmosphere-less planetary bodies. An important distinction between the concept developed here and that of Ref. [125], is that the vehicle is assumed to be deployed directly on the surface of the planetary body, analogous to a rover, rather than in proximity operations. A low-fidelity analytical model of the charging process is developed in order to estimate requirements on vehicle and surface charging for anchoring and levitation on various planetary bodies along with theoretical bounds on translational velocity and levitation height. In addition, laboratory experiments demonstrate the capability for ionic-liquid ion sources to induce surface charging on a metal plate and artificially create a local surface electric field. Measurements of the resulting electric force show that the experimental results are in reasonable agreement with the low-fidelity model that describes the fundamental physics of this concept. The contents of this chapter have been published in Ref. [128].

4.2 Vehicle Charging

Vehicle charging is caused by a net current flow in or out of the vehicle. For spacecraft, this net current is often from an imbalance in particle flux between electrons and ions in the surrounding plasma environment, which will cause the spacecraft to charge negatively, or from photoelectron emission, which will cause the spacecraft to charge slightly positive. However, the use of electric propulsion devices introduces a new current in the form of emitted ions. Most electric propulsion devices eject positive ions at currents much greater than that of the particle flux or photoelectron emission, causing the parent spacecraft to charge negatively. If this negative charging is left unchecked, the spacecraft will charge such that all of the emitted ions are attracted back to the body of the spacecraft and no thrust will be produced.

To prevent spacecraft charging, neutralizers such as hollow cathodes [129] are used to both limit the net current flow out of the spacecraft and to neutralize the thruster plume. Because ionic-liquid electrospray thrusters can emit both positive and negative ions, they can act as their own neutralizer. Typical operation involves bipolar operation of pairs of thrusters where one emits positive ions and the other emits negative ions. Ideally, the two thrusters would emit equal currents. However, small differences in thruster performance mean that some level of spacecraft charging is unavoidable. Fortunately, the presence of low-energy ions in electrospray thruster plumes due to fragmentation processes [130] limits the subsequent spacecraft charging [131] and allows for operation of electrospray thrusters in a bipolar configuration without the need for an external neutralizer.

In the concept explored in this work, vehicle charging is intentionally introduced by the use of a single ionic-liquid ion source emitting either positive or negative ions. As the vehicle charges, lower-energy ions will begin to return to the vehicle, lowering the overall net current. However, due to the lack of any neutralization scheme, the vehicle will charge close to the potential of the ions with the highest energy. Figure 4-2 shows a typical energy distribution for ions in the emitted ion beam of an ionic-liquid ion source measured with a retarding potential analyzer. Current, normalized by the total current in the beam, is measured versus retarding potential, normalized by the applied source potential. As the retarding potential increases beyond the energy of certain ions in the plume, those ions will no longer be able to reach the detector, and therefore, the measured current will drop. Distinct steps can be seen in the plot due to low-energy ions created from fragmentation processes external to the thruster. However, almost half of the ions in the beam have energy close to the source potential, meaning that the vehicle will charge close to the source potential in free space. Additionally, even with the presence of external plasma and photoelectron currents, the output current of an electrospray thruster is approximately 150 μA [24], which is several orders of magnitude greater than the predicted ~100 nA of photoelectron current for a small vehicle with diameter of 10 cm [132], which in turn is large relative to the predicted plasma current on a planetary body such as the Moon [133]. As such, equilibrium in the presence

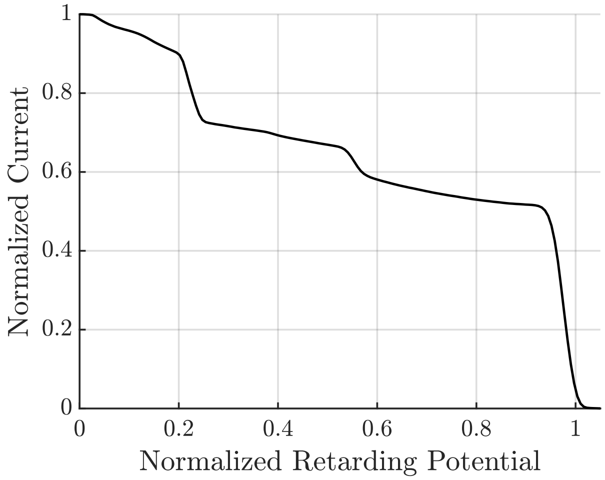

Figure 4-2: Typical energy distribution of ions in the the emitted ion beam from an ionic-liquid ion source [130].

of external plasma and photoelectron currents will still require that the vast majority of the ion beam returns to the vehicle, implying that the vehicle will still charge close to the source potential.

Assuming that the vehicle charges close to the source potential, then the charge on the vehicle, q_{v}, can be calculated from

$$q_{\mathrm{v}} \approx C_{\mathrm{v}} V_{\mathrm{sc}} \tag{4.2}$$

where C_{v} is the capacitance of the vehicle relative to infinity and V_{sc} is the source potential. The capacitance of a small vehicle with characteristic dimension of 10 cm is on the order of 10 pF. It is assumed here that the vehicle is operating directly on the surface of the planetary body, and therefore cannot deploy wings to increase its capacitance, as is considered in Ref. [125]. Typical source potentials of ionic-liquid ion sources are on the order of 1-3 kV; however, the beam could be further accelerated through the use of additional electrodes in order to increase this value to the order of 10 kV or more. Therefore, the expected charge of the vehicle is on the order of 100 nC. Electric levitation can be achieved if the electric force is equal to the weight of the vehicle

$$m_{\mathrm{v}} g \approx q_{\mathrm{v}} E \tag{4.3}$$

Table 4.1: Vehicle and planetary body parameters.

Parameter	Value
Vehicle mass	1 kg
Vehicle dimension	10 cm
Thruster potential	10 kV
Surface electric field	10 V/m
Planetary body mass density	3.34 g/cm^3

where m_{v} is the mass of the vehicle, g is the local gravitational acceleration, and E is the local electric field. For an assumed vehicle mass of 1 kg and local electric field of 10 V/m, the local gravitational acceleration needs to be on the oder of 1 μm/s^2 or lower for levitation to be possible.

Such a small gravitational acceleration is restricted to very small planetary bodies. Assuming a spherical planetary body of radius R and uniform mass density ρ, the gravitational acceleration on the surface is given by

$$g \approx \frac{4}{3} G \pi \rho R \tag{4.4}$$

where G is the universal gravitational constant. Assuming a mass density of 3.34 g/cm^3, the average mass density of the Moon, the approximate order of magnitude for the largest planetary body where levitation could be achieved with the natural surface charging on the sun-facing surface is 1 m. Levitation on larger planetary bodies could be achieved on the night side or at the terminator due to the greater electric field. However, operation on the night side would be heavily limited by the ability of the vehicle to generate power, and operation at the terminator restricts the area of the planetary body the vehicle can explore.

Figure 4-3 shows an estimate of the maximum planetary body radius on which levitation could be achieved versus source potential for the same vehicle and planetary body parameters as before, summarized in Table 4.1. A source potential of 1 MV would be required to achieve levitation on a planetary body with a radius of 120 m. Even for planetary bodies with significant porosity such that their mass density is closer to 1 g/cm^3, such as the asteroid 2011 MD [134], the required source potential for levitation will still be of the same order. These magnitudes would be very challenging to achieve, especially on a compact vehicle.

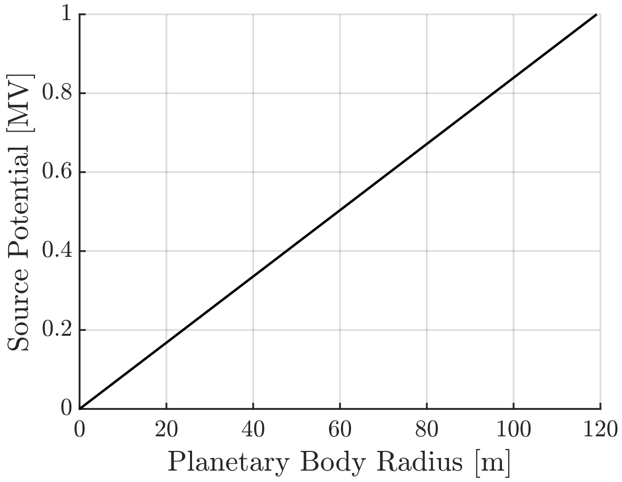

Figure 4-3: Required source potential in order to achieve levitation versus planetary body radius when leveraging the natural surface charging.

4.3 Surface Charging

In order to enable electric levitation for such a small vehicle without requiring impractically high thruster potentials, the local surface electric field of the planetary body would need to be artificially increased. Ionic-liquid ion sources could be used to irradiate the surface directly below the vehicle with ions to charge it, thereby modifying the magnitude of the local electric field. Initially, with the vehicle at rest on the surface of the planetary body, ions can be emitted from the vehicle directly into the surface, thereby charging both the vehicle and the local surface. As with the vehicle charging analysis, the current of an electrospray thruster is expected to dominate any external currents. Therefore, plasma and photoelectron currents are neglected during this analysis.

Because the vehicle starts on the surface of the planetary body, it is assumed that all of the emitted ions either reach the surface or return to the vehicle. In this case, the charge of the vehicle will be equal but opposite to the charge on the surface

$$-q_{\mathrm{v}} \approx q_{\mathrm{s}} \approx q \tag{4.5}$$

where q_{s} is the charge on the surface. The surface charge densities on the vehicle and surface are therefore

$$\sigma_{\text{v}} \approx -\frac{q}{A_{\text{v}}} \qquad \text{and} \qquad \sigma_{\text{s}} \approx \frac{q}{a_{\text{s}}} \tag{4.6}$$

where A_{v} and A_{s} are the surface are of the vehicle and charged surface respectively. The surface are of the vehicle will typically be the surface area of the body of the vehicle, while the surface are of the charged surface will depend on what area is irradiated by the ion beam. This analysis assumes that the charge is evenly distributed on the body of the vehicle. In reality, the charge distribution will be uneven and depend on the shape of the vehicle. Because this effect will be unique to different vehicles, it is neglected here.

Approximating the distance between the vehicle and the surface as small with respect to the extent of A_{v} and A_{s}, and the geometry of the vehicle and surface charge to be that of a flat plate, then the magnitude of the electric field between the vehicle and the surface is approximately

$$E \approx \frac{q}{2\epsilon_0 A_{\text{s}}} + \frac{q}{2\epsilon_0 A_{\text{v}}} \tag{4.7}$$

where ϵ_0 is the permittivity of free space. The vehicle and surface will continue to charge until the potential difference between the vehicle and surface is equal to the source potential

$$Eh \approx \frac{qh}{2\epsilon_0}\left(\frac{1}{A_{\text{s}}} + \frac{1}{A_{\text{v}}}\right) \approx V_{\text{sc}} \tag{4.8}$$

where h is the distance between the vehicle and the surface. Once this condition is met, no ions will be able to reach the surface and will all return back to the vehicle. The resulting equilibrium charge is

$$q \approx \frac{2\epsilon_0 V_{\text{sc}}}{h}\left(\frac{A_{\text{s}} A_{\text{v}}}{A_{\text{s}} + A_{\text{v}}}\right) \tag{4.9}$$

which produces a local electric field from the surface of

$$E \approx \delta(h)\frac{q}{2\epsilon_0 A_{\text{s}}} \approx \delta(h)\frac{V_{\text{sc}}}{h}\left(\frac{A_{\text{v}}}{A_{\text{s}} + A_{\text{v}}}\right) \tag{4.10}$$

where $\delta(h) \in (0, 1]$ accounts for a reduction in the electric field due to 3-D effects. Approximating the local surface charging as a disk, then the electric field along its center axis is

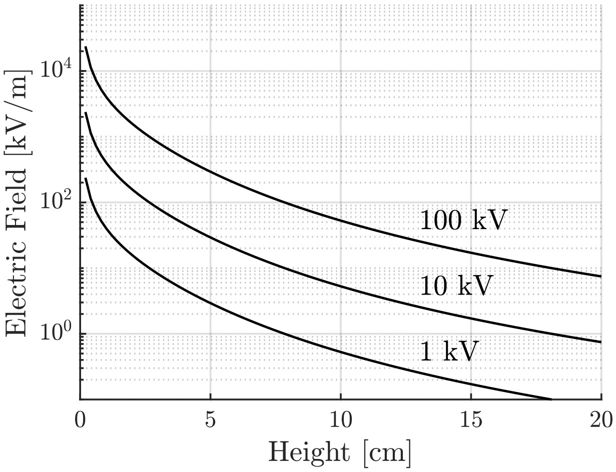

Figure 4-4: Artificially-created electric field versus vehicle height for different source potentials. Charging areas are assumed to be circular with radius of 5 cm.

given by

$$E_{\mathrm{s}}(h) \approx E_{\mathrm{s},0}\left(1 - \frac{h}{\sqrt{h^2 + r_{\mathrm{s}}^2}}\right) \tag{4.11}$$

where $E_{\mathrm{s},0}$ is the electric field of an infinite flat plate and r_{s} is the radius of the charged area. The reduction factor, $\delta(h)$, can then be estimated as

$$\delta(h) \approx 1 - \frac{h}{\sqrt{h^2 + r_{\mathrm{s}}^2}} \tag{4.12}$$

which gives an electric field at the height of the vehicle of

$$E(h) \approx \delta(h)\frac{V_{\mathrm{sc}}}{h}\left(\frac{A_{\mathrm{v}}}{A_{\mathrm{s}} + A_{\mathrm{v}}}\right) \tag{4.13}$$

Figure 4-4 shows the resulting electric field for different source potentials and vehicle heights. For calculating the charging areas, A_{s} and A_{v}, it is assumed that the areas are circular with radius of 5 cm. Note that in all cases the electric field that is created is far greater than the natural 10 V/m; for a potential of 10 kV and height of 10 cm the resulting electric field is approximately 5 kV/m. This increase in the local electric field is what will enable electric actuation to be a viable option for surface anchoring as well as levitation.

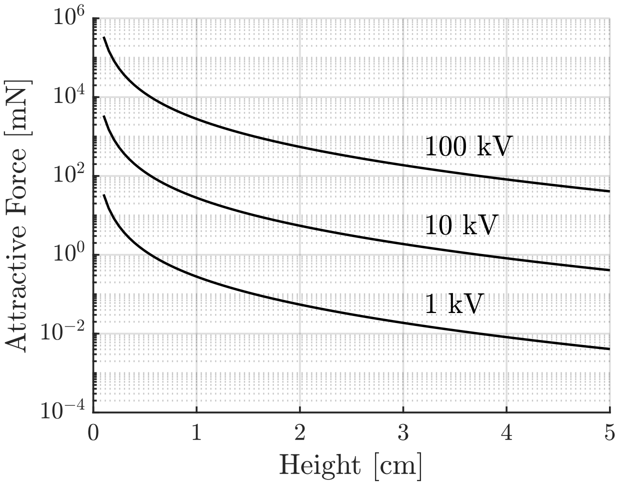

Figure 4-5: Attractive force versus height for different source potentials. Charging areas are assumed to be circular with radius of 5 cm.

4.4 Surface Anchoring

When the local electric field is artificially increased by irradiating the surface with ions, an attractive electric force is created between the vehicle and the surface due to the residual charge left behind on the vehicle. This attractive force could be used to anchor the vehicle to the planetary body's surface. The attractive electric force is given by

$$F_{\mathrm{a}} \approx q E_{\mathrm{s}}(h) \tag{4.14}$$

where q is determined from Eq. 4.9 and $E_{\mathrm{s}}(h)$ is determined from Eq. 4.13 to give

$$F_{\mathrm{a}} \approx \delta(h) \frac{2\epsilon_0 V_{\mathrm{sc}}^2}{h^2} \left(\frac{A_{\mathrm{s}} A_{\mathrm{v}}^2}{(A_{\mathrm{s}} + A_{\mathrm{v}})^2} \right) \tag{4.15}$$

Figure 4-5 shows the resulting attractive force for different source potentials and vehicle heights. Again, the charging areas are assumed to be circular with radius of 5 cm. Due to the strong dependence on source potential and vehicle height in Eq. 4.15, a wide range of attractive forces can be created. As an example case, for a source potential of 10 kV and a vehicle height of 1 cm, the attractive force is approximately 30 mN. While this may not seem like a notable amount of force, particularly in the context of terrestrial applications, 30 mN can be a considerably useful force in low-gravity environments such as operating on the surface of a small asteroid.

One application could be the use of the attractive force for anchoring to the surface of a rotating asteroid. Known asteroids in the solar system that have been characterized for their approximate radius and spin rate can be found in a lightcurve database [135]. Given a radius and spin rate then the required forced in order to anchor a vehicle to the surface of the asteroid can be approximated from

$$F_{\text{anchor}} \approx mR\Omega^2 \tag{4.16}$$

where m is the vehicle mass, R is the asteroid's radius, and Ω is the asteroids rotational frequency. Figure 4-6 shows the approximate anchoring force for a small, 1 kg, vehicle on the surface of several asteroids in the lightcurve database. Each marker on the plot represents a known asteroid in the solar system. The lower dashed line labeled as "Gravity" represents an estimate of the gravitational force on the asteroid's surface assuming that the mass density of the asteroid is equal to the mass density of S-type asteroids (2.71 g/cm^3 [136]). The mass density for S-type asteroids is assumed as the vast majority of small asteroids ($R \sim 10$ m) in the lightcurve database are S-type. The apparent dearth of C-type asteroids, which are the largest family of asteroids in the solar system, may be due to their low albedo, relative to S-type asteroids, which when combined with the small size of the asteroids surveyed here makes them difficult to observe [137].

Notably, asteroids with radius greater than 100 m almost always seem to have sufficient gravitational force in order to enable anchoring on their surfaces. This observation has led to the conclusion that these asteroids are likely rubble-pile asteroids held together by gravitational force alone while smaller asteroids with required anchoring force larger than the surface gravitational force are likely monolithic [138]. For these small asteroids, anchoring may be possible through the use of electric actuation. The dashed line labeled "Electric" in Figure 4-6 represents the 30 mN anchoring force calculated previously. For the vast majority of asteroids, this 30 mN electric force would be sufficient to anchor the vehicle to the asteroid's surface. While some asteroids would require larger anchoring forces, likely due to anomalously high rotational frequencies, the electric force could be increased by using larger source potentials or larger charging areas.

As specific example cases, consider the asteroids 2006 RH$_{120}$ [139], 2011 MD [134], and three fast-rotating asteroids 1999 TY$_2$, 1999 SF$_{10}$, and 1998 WB$_2$ [140]. Both 2006 RH$_{120}$

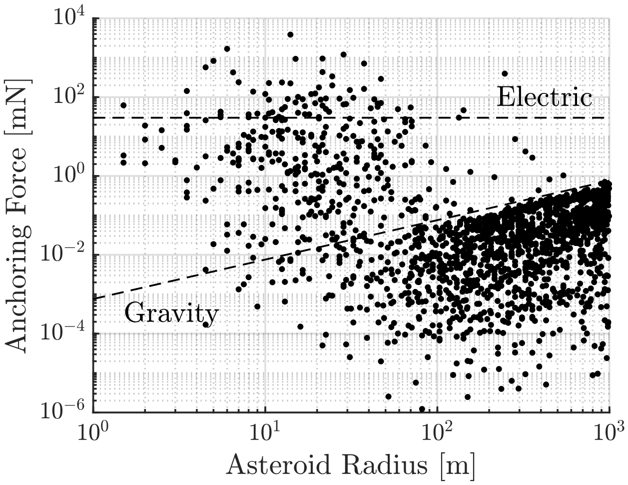

Figure 4-6: Estimated force required for anchoring to the surfaces of known asteroids in the solar system versus asteroid radius.

Table 4.2: Required source potential in order to anchor a small, 1 kg, vehicle to the surfaces of different asteroids. Charging areas are assumed to be circular with radius of 5 cm.

Asteroid Name	Radius	Rotational Period	Required Potential
2006 RH_{120}	1.5 m	2.7 min	2.8 kV
2011 MD	3.5 m	11.6 min	1.0 kV
1999 TY_2	40 m	7.3 min	5.4 kV
1999 SF_{10}	30 m	2.5 min	13.7 kV
1998 WB_2	60 m	18.8 min	2.5 kV

and 2011 MD have been identified as easily-retrievable objects [141] which could be brought to the L_1 or L_2 Lagrange points in the Sun-Earth system at low-Δv cost. Such objects are attractive targets for future asteroid redirection missions as they could easily be redirected to locations near Earth for further study. Table 4.2 shows the source potential required to anchor a 1 kg vehicle to the surfaces of these asteroids. As before, charging areas are assumed to be circular with radius of 5 cm. For an asteroid such as 2011 MD, which is relatively small and has a relatively low rotational frequency, a source potential of only 1.0 kV is required in order to anchor the vehicle. Asteroids such as 1999 SF_{10} which are slightly larger but have relatively high rotational frequency require larger source potentials, but even in the case of 1999 SF_{10} the required source potential is only 13.7 kV. Such a source potential is higher than typically used for ionic-liquid ion sources in propulsive applications, but is still a feasible source potential.

4.5 Levitation

In order to achieve levitation, the vehicle needs to be charged to the same polarity as the surface. This can be achieved in a two-step process. First the surface is charged by irradiating the surface with ions in order to create an electric field given by Eq. 4.13. Then ions the vehicle emits ions away from the surface, thereby charging the vehicle but not affecting the surface charge. The magnitude of the vehicle charge will be given by Eq. 4.2 which results in a repulsive electric force of

$$F_\mathrm{r} \approx \delta(h) \frac{C_\mathrm{v} V_\mathrm{sc}^2}{h} \left(\frac{A_\mathrm{v}}{A_\mathrm{s} + A_\mathrm{v}} \right) \tag{4.17}$$

For levitation, the electric force needs to overcome the local gravitational force

$$F_\mathrm{r} \geq m_\mathrm{v} g \tag{4.18}$$

which can be solved for the required source potential

$$V_\mathrm{sc} \approx \sqrt{\frac{m_\mathrm{v} g h}{C_\mathrm{v} \delta(h)} \left(\frac{A_\mathrm{s} + A_\mathrm{v}}{A_\mathrm{v}} \right)} \tag{4.19}$$

Figure 4-7 shows the required source potential in order to achieve levitation versus surface gravitational acceleration for vehicle and planetary body parameters given by Table 4.1, a distance between the vehicle and surface of 2 cm, and assuming that the radius of the surface charging is equal to the radius of the vehicle. The thruster potential is shown both for the case where the natural surface charging is used and for the case where the surface charging is artificially increased through ion bombardment. As found previously, achieving levitation with only the natural surface charging would be infeasible; for an object such as the Moon the required source potential would be approximately 10 GV. The use of ion bombardment to artificially increase the surface charging causes the required source potentials to become feasible. For objects such as Phobos with gravitational accelerations on the order of 1 mm/s^2, source potentials of a few kV are required, a level that has already been demonstrated with electrospray thrusters in space. Moving to slightly larger objects such as Psyche with gravitational accelerations on the order of 1 cm/s^2, source potentials on the order of 10s of kV are required which are still feasible with current electrospray thrusters.

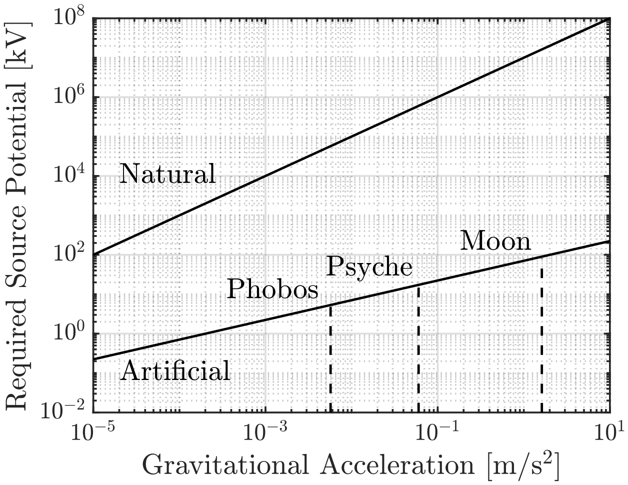

Figure 4-7: Required source potential in order to achieve levitation versus surface gravitational acceleration when leveraging the natural surface charging and when artificially increasing the natural surface charging through ion bombardment.

Finally, even for objects as large as the moon with gravitational accelerations on the order of 1 m/s^2, source potentials on the order of 100s of kV are required. These source potentials are beyond our current capabilities, but may be possible in the near future.

Once levitation has been achieved, the vehicle can modify its charge in order to control its altitude. However, it is likely that the vehicle will also have to maintain the local surface charging in order to counter any slow charge dissipation to the surrounding plasma environment or into the bulk of the planetary body. As such, the maximum operational levitation height of the vehicle will be limited. If the vehicle levitates too high, then the potential difference between the vehicle and the surface will be larger than the source potential and ions will not be able to reach the surface in order to maintain the surface charge. In addition, as the vehicle traverses across the surface it will have to charge any new, uncharged, surface it encounters. Therefore, the translational speed of the vehicle will be limited by the time-scale at which the local surface can be charged to the required surface charge density for levitation.

4.5.1 Levitation Height

The local surface electric field which enables vehicle levitation also repels ions used to charge the surface. For a given maximum ion energy, set by the source potential, if the levitation height is too large then ions will be unable to reach the surface, preventing the required surface charging from being maintained in the presence of plasma currents and photoelectron emission. While the vehicle is not strictly unable to levitate beyond this height, it could momentarily increase its own body charge in order to levitate higher, it would lose the ability to control the local surface charge. As such, it is likely that during operations, the vehicle will maintain a levitation height such that it can control the local surface charge.

The electric field between the vehicle and the surface is a superposition of the electric field from the vehicle and the electric field from the surface. The magnitude of the surface electric field required for levitation is given by

$$E_{\mathrm{s}} \approx \frac{m_{\mathrm{v}} g}{C_{\mathrm{v}} V_{\mathrm{sc}}} \tag{4.20}$$

Approximating the vehicle as a disk with uniform charge distribution on the top and bottom surfaces, then its surface charge density is given by

$$\sigma_{\mathrm{v}} \approx \frac{C_{\mathrm{v}} V_{\mathrm{sc}}}{2\pi r_{\mathrm{v}}^2} \tag{4.21}$$

where r_{v} is the radius of the vehicle. This surface charge density produces an electric field with magnitude of

$$E_{\mathrm{v}} \approx \frac{\sigma_{\mathrm{v}}}{\epsilon_0} \approx \frac{C_{\mathrm{v}} V_{\mathrm{sc}}}{2\epsilon_0 \pi r_{\mathrm{v}}^2} \tag{4.22}$$

and will have direction opposite to the surface electric field.

In order for ions to reach the surface, the potential difference between the vehicle and the surface needs to be less than the highest-energy ions emitted by the source. Ions used to charge the surface will be repelled by the surface and the vehicle. However, repulsion away from the vehicle aids in “pushing” the ions towards the surface. Therefore, the height of the vehicle at which ions, accelerated through a source potential of V_{sc}, will no longer be able to reach the surface is given by

$$h^* \approx \frac{V_{\mathrm{sc}}}{E_{\mathrm{s}} - E_{\mathrm{v}}} \tag{4.23}$$

For cases in which $E_{\mathrm{s}} \leq E_{\mathrm{v}}$ there is no limitation on the levitation height. However, this analysis assumes that the levitation height is small relative to the extent of the local surface charging and the characteristic dimension of the vehicle, and will be invalid for large levitation heights due to three-dimensional effects of the electric fields. Substituting in the surface and vehicle electric fields gives a maximum levitation height of

$$h^* \approx = \frac{2\pi\epsilon_0 r_\mathrm{v}^2 C_\mathrm{v} V_\mathrm{sc}^2}{2\pi\epsilon_0 m_\mathrm{v} g r_\mathrm{v}^2 - C_\mathrm{v}^2 V_\mathrm{sc}^2} \tag{4.24}$$

Approximating the capacitance of the vehicle as that of a finite disk with uniform charge distribution [142], then

$$C_\mathrm{v} \approx 2\pi\epsilon_0 r_\mathrm{v} \tag{4.25}$$

which allows the maximum operational levitation height to be reduced to

$$h^* \approx \frac{2\pi\epsilon_0 r_\mathrm{v} V_\mathrm{sc}^2}{m_\mathrm{v} g - 2\pi\epsilon_0 V_\mathrm{sc}^2} \tag{4.26}$$

and leads to a non-dimensional maximum levitation height

$$\bar{h} = \frac{h^*}{r_\mathrm{v}} \approx \frac{2\pi\epsilon_0 V_\mathrm{sc}^2}{m_\mathrm{v} g - 2\pi\epsilon_0 V_\mathrm{sc}^2} \tag{4.27}$$

normalized by the vehicle characteristic dimension.

Figure 4-8 shows the non-dimensional maximum levitation height versus surface gravitational acceleration for vehicle and planetary body parameters given by Table 4.1 including a thruster potential of 50 kV. For 10 kV, the normalized levitation height for planetary bodies with surface gravitational acceleration similar to Psyche is around 0.1, potentially enabling the vehicle to traverse across the surface. If the thruster potential is increased to 50 kV, similar levitation heights could be maintained on planetary bodies as large as the Moon. More detailed analysis of the electric field between the vehicle and the surface is required to fully capture the three-dimensional effects. However, per this initial analysis, maintaining electric levitation with ionic-liquid ion source should be achievable with current technology.

Plasma shielding due to the surrounding plasma environment will also limit the levitation height of the vehicle. However, theoretical predictions of the smallest Debye length, due to photoemission on the Sun-facing surface of the planetary body, are 50+ cm [111]. Therefore, for levitation heights of a few tens of centimeters, the vehicle will be operating within a Debye

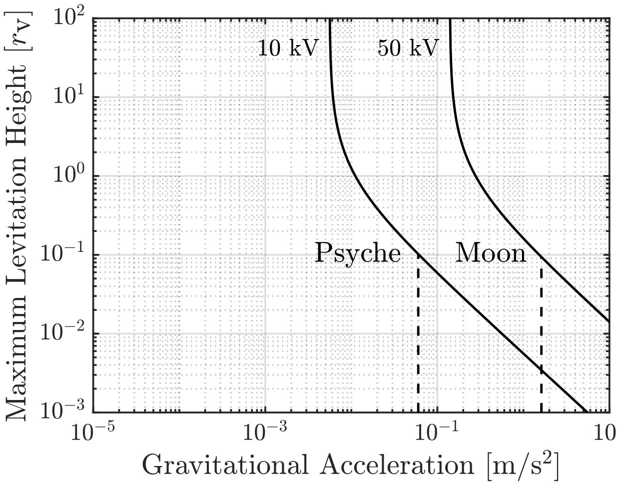

Figure 4-8: Maximum levitation height normalized by the vehicle's characteristic dimension at which the local surface charge can be controlled versus surface gravitational acceleration for source potentials of 10 kV and 50 kV and assumed vehicle mass of 1 kg.

length of the surface and the surface electric field should not be significantly attenuated. In addition, the strong surface charging created by ion bombardment should serve to extend the plasma sheath and further mitigate the effects of plasma shielding.

4.5.2 Translational Speed

As the vehicle traverses across the planetary body surface, any new, uncharged surface it encounters needs to be charged to the required surface charge density for levitation. If the required surface charge density is too high, then the vehicle's translational speed will be limited in order to ensure proper surface charging is achieved. Assuming that all the current, I_{sc}, emitted by the ion source goes into charging the surface below the vehicle, then the time required to achieve a local charge density is given by

$$t_{\text{c}} \approx \frac{\pi r_{\text{s}}^2 \sigma_{\text{s}}}{I_{\text{sc}}} \approx \frac{2\pi\epsilon_0 r_{\text{s}}^2 E_{\text{s}}}{I_{\text{sc}}} \tag{4.28}$$

Typical currents for ionic-liquid electrospray thrusters are 100-200 μA [24]. Figure 4-9 shows the surface charging time if the ion source used to charge the surface is operated at 100 μA versus surface gravitational acceleration for vehicle and planetary body parameters given by Table 4.1. Even for planetary bodies as large as the Moon, the required surface charging time is less than 100 ms. This means that the vehicle will not be significantly

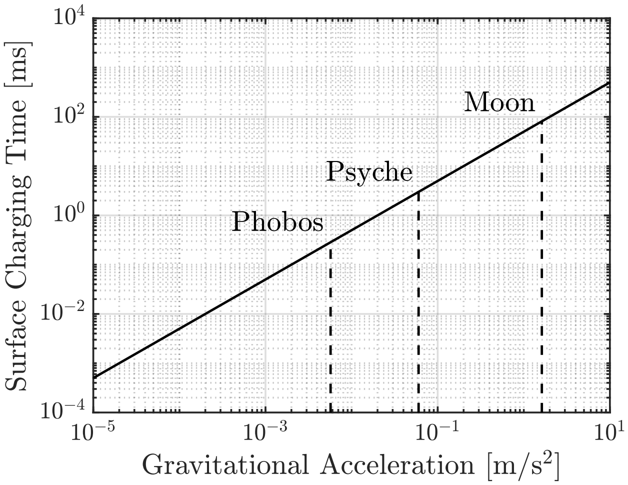

Figure 4-9: Required charging time for vehicle levitation versus surface gravitational acceleration. A charging current of 100 μA is assumed for a 1 kg, 10 cm vehicle with capacitance equal to that of a finite disk with uniform charge distribution.

limited in its ability to traverse across the surface.

The characteristic speed that the vehicle will be able to traverse across the surface while maintaining the required surface charge density for levitation will scale with

$$u = \frac{r_\mathrm{s}}{t_\mathrm{c}} \tag{4.29}$$

For the Moon, the characteristic speed is approximately 1.2 m/s, which is comparable to that of the crewed Lunar Roving Vehicle [143] and two orders of magnitude greater than that of the Lunokhood rovers [144]. For smaller planetary bodies such as Psyche, the characteristic speed increases to approximately 33 m/s. While the vehicle would not be operated at such speeds due to other limitations, such as the navigation system or for collision avoidance, the magnitude of the characteristic speed demonstrates that the surface charging would not be the limiting factor for the actual operational speed of the vehicle.

The assumption that all of the emitted current will go into charging the planetary body's surface is the main unknown for such a concept. The surface charging will depend not only on the ion flux from the ion source, but also on the properties of the surface materials, which can vary between planetary bodies and control secondary charge emission and charge dissipation. Nevertheless, even if only 10% of the emitted current goes into charging the surface, the characteristic speed of the vehicle on the Moon would be 0.12 m/s and still

Table 4.3: Summary of derived parameters for a 1 kg, 10 cm vehicle with capacitance equal to that of a finite disk with uniform charge distribution. It is assumed that a source current of 100 μA is used to charge the planetary body surface.

Parameter	Psyche (0.06 m/s^2)	Moon (1.62 m/s^2)
Required source potential	10 kV	50 kV
Maximum levitation height	1 cm	1 cm
Surface charging time	3 ms	81 ms
Characteristic vehicle speed	33 m/s	1.2 m/s

allow for efficient surface exploration comparable to that of wheeled rovers.

Also of importance is the time required to charge the vehicle body. Assuming that 200 μA of current is emitted away from the planetary surface, so as to charge the vehicle but not the surface, then the new current leaving the vehicle, taking into account the 100 μA of current used to charge the surface, is 100 μA. The self-capacitance of the vehicle is approximately 10 pF giving a theoretical charging rate of 10 MV/s. Therefore, the vehicle body can be charged to the required 10 kV potential in ~50 μs, faster than the time required to charge the surface until objects smaller than Phobos ($g \leq 6$ mm/s^2) are considered. However, unlike surface charging, charging of the vehicle body only needs to be done once, assuming minimal charge loss, as the vehicle traverses across the surface.

Table 4.3 summarizes the vehicle characteristic speed as well as previously derived parameters for a 1 kg, 10 cm vehicle operating on planetary bodies similar to Psyche and the Moon, with surface gravitational accelerations of 0.06 m/s^2 and 1.62 m/s^2 respectively. The required source potential is taken to be the minimum source potential at which the rover would be able to levitate to 0.1 its characteristic dimension, 1 cm in this case, under the assumption that the charge distribution on the vehicle can be approximated as that of a uniformly charged flat disk and that the extent of the surface charging is larger than the characteristic dimension of the vehicle. The vehicle could levitate to greater heights with larger source potentials, but more detailed analysis of the charge distribution and three-dimensional effects are required. Surface charging times and characteristic vehicle speeds were calculated under the assumption of a source current of 100 μA, representative of current electrospray thruster capabilities.

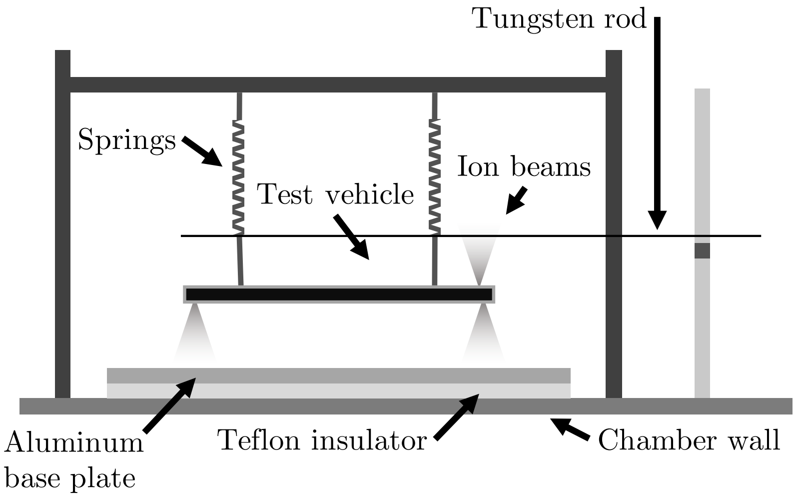

Figure 4-10: Notional diagram of the experimental setup.

Table 4.4: Experimental setup parameters.

Parameter	Value
Test vehicle mass	60 g
Test vehicle radius	75 mm
Test vehicle thickness	30 mm
Source potential	1.9-2.4 kV
Source current	100-300 nA
Hovering height	10-15 mm
Equivalent spring constant	10 N/m
Deflection under gravitational load	59 mm

4.6 Experimental Setup

The goal of the experiment was to demonstrate the feasibility of using ionic-liquid ion sources for combined vehicle and surface charging, and to validate the analytical model. Figure 4-10 shows a diagram of the test setup used in a vacuum chamber operated at pressures of around 10 μTorr and at room temperature. A test vehicle, wrapped in aluminum foil to distribute charge over the surface and ensure constant potential, is suspended by two springs over an aluminum base plate. The setup is electrically isolated from the vacuum chamber walls by a teflon sheet. A tungsten rod is attached at the ends of the springs such that any vertical movement of the test vehicle due to external forces can be measured as a displacement of the tungsten rod relative to a marker. Relevant parameters from the experimental setup are summarized in Table 4.4.

The test vehicle is a hexagon of mass 60 g, average radius 7.5 cm, and thickness 3 cm and has five tungsten single-tip ionic liquid ion sources. Four of the sources point downwards towards the aluminum base plate and can emit positive ions while the last source points upwards away from the base plate and can emit negative ions. For testing, single-tip source were used as opposed to fully microfabricated electrospray thrusters in order to simplify the test setup. Single-tip sources have similar potential characteristics to electrospray thrusters so experimental results will be indicative of expected performance with full thrusters. For theoretical analysis, the shape of the test vehicle is approximated as a hollow disk with radius 7.5 cm and thickness 3 cm.

The ion sources were fabricated from tungsten wire according to Ref. [21] and used 1-Ethyl-3-methylimidazolium tetrafluoroborate (EMI-BF_4) as the ionic liquid. The source potential was provided by two PICO Electronics 5AV1500 high-voltage DC-DC converters operated in series to allow source potentials from 0-3 kV and the current was measured through a 1 ± 0.1 MΩ shunt resistor. As the actual source potential could not be measured during the experiment, the output of the converters at different input potentials was calibrated to within ±10 V prior to the experiment. The source potential could then be inferred based on the input potential to the high-voltage converter. The input potential to the high-voltage converter was controlled with an LM317 voltage regulator to attenuate any noise and allow gradual application of the potential in order to avoid any droplet emission during the emission startup transient. Both the test vehicle and base plate are electrically isolated in order to allow their respective potentials to float in response to emitted current from the ion sources.

During experiments, the sources allows for a limited range of potentials to be tested. The lower limit of this range is given by the starting potential, which is approximated by

$$V_{\text{start}} \approx \sqrt{\frac{\gamma R_{\text{c}}}{\epsilon_0}} \left(\frac{4l}{R_{\text{c}}} \right) \tag{4.30}$$

where γ is the surface tension of the ionic liquid, R_{c} is the radius of curvature of the tungsten emitter tip, and l is the distance from the tip to the extractor grid [145]. For the ionic-liquid ion sources used in this work, the starting potential is approximately 1.9 kV. The upper limit of the thruster potential range occurs at approximately 2.4 kV, where electrical shorts between the emitter tip and extractor start to be observed.

Given a test vehicle mass of 60 g and a thruster potential of 2 kV, Eq. 4.27 gives an expected levitation height of around 7×10^{-4} times the characteristic dimension of the test vehicle which corresponds to levitation heights on the order of 5 μm. This requires that the base of the test vehicle be suspended 5 μm above the base plate, severely constraining the test and measurement systems. Therefore, the use of springs to offload the gravitational force is necessary to get clear measurements of the electrostatic force. Two springs, with spring constants of 5 N/m and each carrying half of the test vehicle's weight, are used to balance the test vehicle's rotation and suspend it parallel to the base plate. The weight of the test vehicle and expected electric force are within the limits of the linear regime for the springs used during experiment.

The displacement of the tungsten rod was measured with a Dino-Lite 720p digital microscope with resolution and magnification such that each pixel corresponded to less than 1 μm of displacement. At this resolution, errors in determining the displacement of the tungsten rod due to pixel error will be two orders of magnitude lower than the expected displacement due to the electric force (of order 100 μm) and correspond to errors in the measured electric force of 10 μN. Figure 4-11 shows a diagram of the measurement process. With the thrusters off, the tungsten rod rests at an equilibrium displacement from the marker. When the ion sources facing the base plate are fired, the test vehicle and base plate charge to opposite polarities resulting in the test vehicle being attracted towards the base plate. The emitter firing away from the base plate can also be fired in order to charge the test vehicle and base plate to the same polarity, resulting in the test vehicle being repelled from the base plate. The displacement of the tungsten rod, d, is measured and related to the electric force, F_{e}, through the spring constant, k, as

$$\|F_{\mathrm{e}}\| = kd \tag{4.31}$$

4.7 Experimental Results

Figure 4-12 shows an example of the measured attractive electric force over time when the ion sources facing the base plate are fired. In this particular example, a positive potential of 2.07 kV is applied to the emitters facing the base plate. The resulting current charges the test vehicle negatively and the base plate positively resulting in the test vehicle being

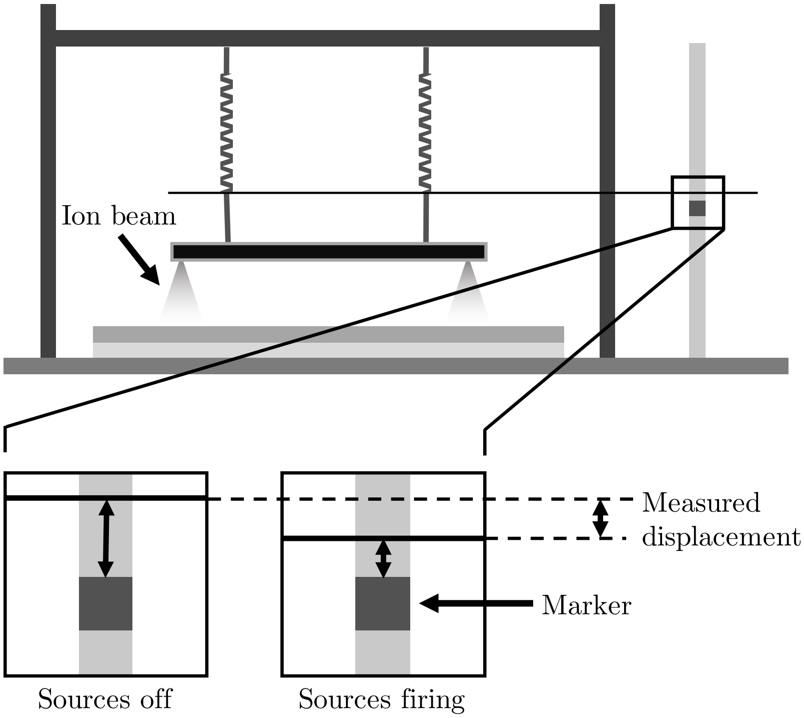

Figure 4-11: Diagram of the measurement principle for estimating electric force through deflection of the tungsten rod.

attracted to the base plate. The measured electric force, represented by the solid line, is approximately 0.96 mN. The filled region corresponds to the expected attractive force based on Eq. 4.15 and the parameters of the test setup. Due to the geometry of the test vehicle, the initial distance between the test vehicle and the base plate is estimated to be 14-15 mm and causes uncertainty in the estimated force. Therefore, the expected force is shown as a fill region rather than a single line. Taking the value of the expected force closest to the measured force gives an expected attractive force of 1.13 mN. Therefore, Eq. 4.15 slightly over-predicts the attractive force by 0.17 mN (18%). Given the simplicity of the model used to develop Eq. 4.15, this is quite a remarkable result; the model is fully analytical and neglects many effects such as the actual distribution of charge on the test vehicle and surface as well as the possibility for secondary electron emission and other effects.

Figure 4-13 shows an example of the measured repulsive electric force over time when the ion source facing away from the base plate is fired. The accumulated charge on the base plate from the attractive force case in Figure 4-12 is left alone and only the test vehicle's charge is modified. In this particular example, a negative potential of magnitude 1.8 kV

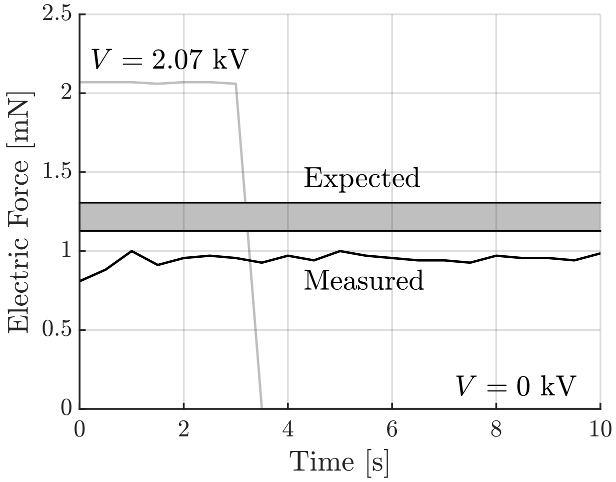

Figure 4-12: Comparison of theoretical prediction and experimental measurement for the attractive force.

is applied to the emitter facing away from the base plate, charging the vehicle positively. Since the base plate retains its positive charge, this results in the test vehicle being repelled away from the base plate with an observed repulsive force of approximately 0.29 mN. The expected force from Eq. 4.17 is again shown as a fill region due to uncertainty in the initial test vehicle height. The capacitance of the test vehicle is estimated to be that of a finite disk with uniform charge distribution

$$C_{\mathrm{v}} \approx 2\pi\epsilon_0 r_{\mathrm{v}} \tag{4.32}$$

Taking the expected force closest to the measured force gives an expected repulsive force of 0.31 mN. As in the attractive force case, Eq. 4.17 slightly over-predicts the resulting force magnitude, this time with an error of 0.018 mN (6%). However, the model well predicts the approximate magnitude of the repulsive force and is also able to capture the expected asymmetry between the attractive and repulsive forces.

Figure 4-14 shows the measured attractive force as the source potential is varied along with the expected relationship from Eq. 4.15. For these experiments, the initial distance between the test vehicle and base plate is estimated to be 11-12 mm. Again the model over-predicts the attractive force relative to the experimental data. This discrepancy could be due to further three-dimensional effects from the charge on the test vehicle being spread out over the vehicle's surface or the effect of secondary electrons. As ions return to the test vehicle,

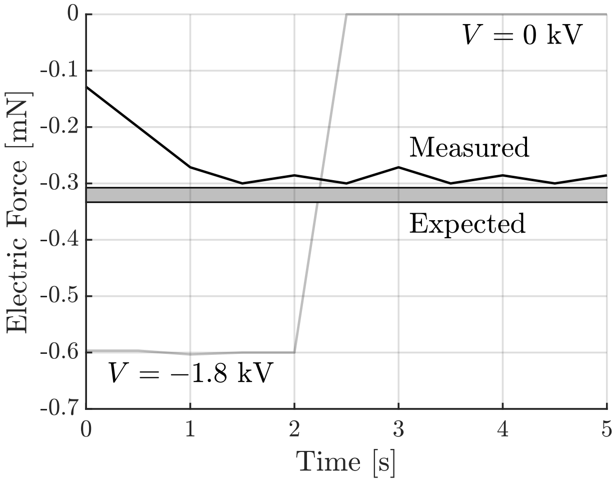

Figure 4-13: Comparison of theoretical prediction and experimental measurement for the repulsive force.

they can emit secondary electrons. If the test vehicle is charged negatively, as it is during the attractive force experiments, the secondary electrons can escape the vehicle and be attracted to the base plate, reducing the overall charge level of both the test vehicle and base plate and resulting in a corresponding decrease in the electrostatic force. Detailed analysis of the effects of secondary electron emission requires knowledge of the energy distribution of the emitted ions, which can vary significantly between different sources and propellants. However, the low-fidelity model still captures the approximate magnitude of the expected force and provides insight into the expected trends in the force with parameters such as the source potential. Such insight would be difficult to obtain with purely numerical models.

Another potential source of error in the test setup is charge leakage to the environment, either internal to the vacuum chamber or externally along the electronics connections. However, it is believed that this effect in negligible. Figure 4-15 shows the average measured electric force over time after the ion sources have been turned off for three different test runs. Error bars correspond to one standard deviation. The electric force clearly drops over time which is indicative of charge, either on the test vehicle or base plate, leaking to the environment. Based on Figure 4-14, the reduction in electric force over 60 s corresponds to a potential drop on the test vehicle of approximately 400 V. Given the estimated capacitance of the test vehicle, 4.2 pF, this corresponds to an average leakage current of 28 pA, well bellow the 100-300 nA of current provided by the ion sources. Coincidentally, the ratio of source current to leakage current (100 nA/28 pA = 3571) is of the same order of magnitude

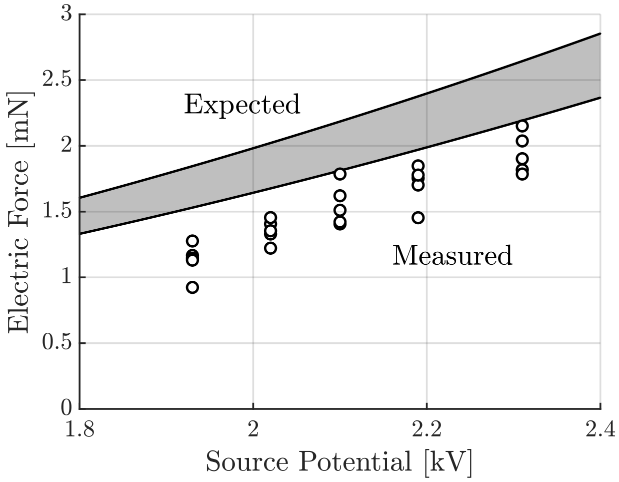

Figure 4-14: Attractive electric force versus source potential along with the expected relationship based on the low-fidelity model.

as the expected ratio of a full electrospray thruster current to plasma and photoelectron currents (100 μA/100 nA = 1500) allowing the leakage current observed during experiment to simulate the effects of plasma and photoelectron currents.

Finally, it is worth comparing the electric force observed during this experiment to the use of propulsion systems in a traditional manner where reactive forces are generated through mass ejection in order to demonstrate the efficiency of the electric actuation concept. The electric force in Figure 4-14 is approximately 1.25 mN for a source potential of 2 kV and is generated through only around 100 nA of current. The mass of the cation of the ionic liquid 1-Ethyl-3-methylimidazolium tetrafluoroborate is 111.2 Da which gives a total mass flow during the experiments of approximately 1.2×10^{-10} g/s. Therefore, in order to produce a force of 1.25 mN with the exact same mass flow, a traditional propulsion system would need a specific impulse on the order of 10^9 s. Such a specific impulse would be infeasible for a couple of reasons. First, the exhaust velocity of the emitted ions would have to be 33 times the speed of light. Second, even if you could miraculously emit ions at such a speed, the power it would take to operate such a system would be approximately 6 MW which is far beyond the capabilities of small space vehicles. However, when using electric actuation, the 1.25 mN force is created with only 0.2 mW of power.

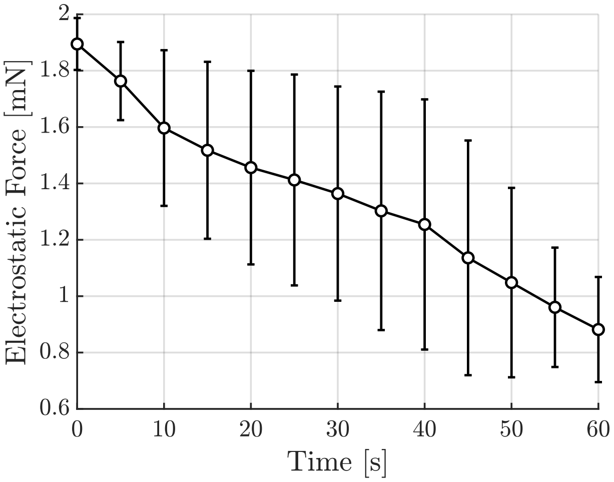

Figure 4-15: Average measured electric force over time after ion sources have been turned off demonstrating slow charge leakage. Error bars correspond to one standard deviation.

4.8 Conclusion

The use of ionic-liquid ion sources for electric levitation on atmosphere-less planetary bodies is analyzed and theoretical predictions on the relationship between electrostatic force and source potential are experimentally verified. A low-fidelity model predicts that levitation heights of approximately 0.1 the characteristic dimension of a 1 kg vehicle would be possible with a 10 kV ion source on a planetary body the size of Psyche and with a 50 kV ion source on a planetary body the size of the Moon, potentially enabling surface maneuverability. Experimental results confirm the qualitative predictions of the low-fidelity model and demonstrate that a 1.25 mN electrostatic force can be created through charge transport while only using 0.2 mW of input power.

A metallic base plate is used during experiments in order to allow the angular distribution of the ionic-liquid ion source plume to be ignored. The surfaces of many planetary bodies will be highly resistive and further experiments will be required to demonstrate similar performance with insulating base plates. However, it is expected that performance should not differ significantly as the insulating surface will allow charge to more easily accumulate and the angular distribution of the source plume can be tuned in order to achieve a desired surface charge distribution. In addition, as the surface directly below the ion sources charges, it will cause the plume to spread and charge much of the surface below the vehicle.

The analytical model developed in this work is low fidelity and ignores effects such as the charge distribution of the vehicle and the surface, photoelectron and plasma current, and secondary electron emission. Of these effects, the distribution of charge is expected to be dominant. Both the photoelectron and plasma currents will be several orders of magnitude lower than the current produced by an ionic liquid ion source for a vehicle of the size considered here (∼10 cm). The effects of secondary electron emission are also expected to be small as the positively charged surface will prevent them from escaping. Since the distribution of charge is unique to the vehicle, it cannot be considered here analytically but will be considered in future work.

Future work will also analyze the interaction of the ion beam with the surface of the planetary body. While the transfer of charge from the ion beam to the surface has been demonstrated here, it is unknown what other interactions there may be. It is possible that mass may be deposited on the surface, or that the ion beam will etch the top layer of the surface and have a cleaning effect. These effects are worth studying in order to ensure that there is not any potential contamination of the planetary body's surface due to irradiation with the ion beam.

Despite the low fidelity of the model, its close prediction (under 20% error) of the experimental results provides confidence that electrostatic levitation with ionic liquid ion sources is a feasible concept. Electrostatic levitation aided by ion sources could be used to provide maneuverability for a spacecraft during proximity operations around a small asteroid as in Ref. [125] or to develop solid-state surface rovers that can traverse across a planetary body's surface with no moving parts. The prospect of a rover that can maneuver across a surface without any physical contact could allow for easier exploration of uneven surfaces relative to traditional wheeled and hopper robots. Wheeled mechanisms struggle with overly rough terrain which is abundant on planetary bodies in the form of rocks, craters, subterranean tunnels, and other steep terrain. These regions of rough terrain are often also regions of scientific interest and the ability to access these areas could greatly increase the science return of future missions.

This work demonstrates, from an actuation standpoint, that such a rover could be possible with current technology. For planetary bodies with surface gravitation acceleration of 0.06 $\mathrm{m/s^2}$ (representative of a planetary body the size of the asteroid Psyche), a 1 kg rover could levitate to heights several times its characteristic dimension with ion source potentials on the order of 25 kV. More detailed analysis of the limits on levitation height are required for cases where the flat-plate assumption for the local electric field breaks down or when plasma shielding becomes significant. In addition, design of both the altitude and attitude controllers for such a rover is required, particularly for cases where the terrain is not perpendicular to the local gravitational field.

In the case of spacecraft, particularly landers, the use of electric levitation could be used to re-position the spacecraft after landing, broadening the potential area of the surface that the lander could analyze. In addition, the electric force could serve to anchor the spacecraft to the surface of the planetary body. Current methods, such as the harpoon used in the Philae lander [146], require intricate mechanisms whose performance can depend on the material composition of the planetary body. The use of ionic-liquid ion sources, such as electrospray thrusters, could allow for a mechanically-simple anchoring system whose performance does not vary significantly with surface composition.

Chapter 5

Conclusion

This thesis addresses three technical challenges associated with the exploration of planetary bodies with electrospray thrusters: inference of the propulsion system thrust output, guidance and control of an underactuated spacecraft in proximity operations, and the use of electric charging for actuation on the surface of an atmosphere-less planetary body. While these challenges were addressed within the context of using electrospray thrusters for asteroid missions, the solutions do have broader applications. The developed methodologies for thrust inference will be applicable to any propulsion system operated in orbit around any planetary body. The guidance and control methods for operating in proximity to a small asteroid can also be used for operation in proximity to another spacecraft. Finally, the charged-particle sources used for charge transfer on the surfaces of atmosphere-less planetary bodies do not need to be ionic-liquid ion sources; other sources of charged particles such as liquid-metal ion sources and even electron sources can be applied.

The use of the ensemble Kalman update for thrust inference in low-Earth orbit is able to reduce the posterior uncertainty in the thrust output by multiple orders of magnitude relative to a commonly-used analytical approach, as demonstrated in Section 2.7.1. Relative to other numerical approaches based on linear filtering, the methodology developed here is able to account for potential modeling error and properly quantify the resulting posterior uncertainty in the thrust output. Many prior approaches neglect to account for the potential of modeling error and as a result will likely report overly-confident uncertainty bounds for the thrust estimate. Representing the modeling error is critical for properly determining the uncertainty, and the ensemble Kalman update allows for simple incorporation of the modeling error through representation as process noise.

In addition to the ensemble Kalman update, a linear measurement model for thrust inference in low-Earth orbit was derived. The core contribution was the extension of linear orbit theory through the derivation of approximate sensitivities of the spacecraft's radial and along-track position with respective to propulsive and atmospheric drag accelerations. The derivation of the linear measurement model allows for computationally-simple predictions of the posterior uncertainty in the propulsive acceleration relative to running the full ensemble Kalman update. In order to account for the modeling error in the linear measurement model, a polynomial chaos expansion of the measurement noise caused by modeling error was developed in order to allow for approximation of the observation covariance. Predictions of the posterior uncertainty with the linear measurement model are approximate, and best serve as a method of surveying a wide range of maneuver parameters prior to running the ensemble Kalman update on a limited set of possible maneuvers.

For proximity operations, the work of this thesis resolves two issues. First, it resolves the issue of controllability for underactuated spacecraft during proximity operations by leveraging a baseline circular orbit; in a frame that rotates with the spacecraft while it is performing the circular motion, the spacecraft can be controlled through linear control approaches. In addition, the circular motion aids in mitigating the possibility of plume impingement from the propulsion system on the central target. Second, an analytical maneuver library was derived in order to leverage the circular motion and guide an underactuated spacecraft during basic proximity maneuvering such as point-to-point maneuvering and landing on or docking to a rotating target. The analytical maneuver library helps to resolve some of the issues with the limited computational capability onboard small spacecraft. Prior approaches typically rely on some form of nonlinear optimization which may be beyond the capabilities of small spacecraft computers whereas the analytical trajectories from the maneuver library can be computed at minimal computational cost.

Finally, opportunities for using ionic-liquid ion sources for novel forms of surface actuation were investigated. Based on the observation of natural surface charging, which is hypothesized to cause the transport of dust particles across the surfaces of atmosphere-less planetary bodies, the use of electric forces was considered in order to anchor a small vehicle to the surface of an atmosphere-less planetary body or even potentially achieve levitation. Preliminary analyses show the possibility of anchoring a small, 1 kg, vehicle to the surface of known asteroids in the solar system such as 2006 RH_{120} and 2011 MD which have both been identified as easily-retrievable objects and may be future targets for asteroid-redirection missions. Levitation on small planetary bodies such as Phobos and Psyche may also be possible with current technology, while levitation on larger planetary bodies such as the Moon may be possible in the future. Basic experiments conducted in a laboratory environment provide confidence in the simple analytical models developed here, and provide the basis for continued research on this concept.

References

[1] Asphaug, E. and Reufer, A., "Mercury and Other Iron-rich Planetary Bodies as Relics of Inefficient Accretion," *Nature Geoscience*, Vol. 7, No. 8, 2014, pp. 564–568, doi:10.1038/ngeo2189.

[2] Marzari, F., Davis, D., and Vanzani, V., "Collisional Evolution of Asteroid Families," *Icarus*, Vol. 113, No. 1, 1995, pp. 168–187, doi:10.1006/icar.1995.1014.

[3] Marrocchi, Y., Bekaert, D. V., and Piani, L., "Origin and Abundance of Water in Carbonaceous Asteroids," *Earth and Planetary Science Letters*, Vol. 482, 2018, pp. 23–32, doi:10.1016/j.epsl.2017.10.060.

[4] Elvis, M., "How Many Ore-bearing Asteroids?" *Planetary and Space Science*, Vol. 91, 2014, pp. 20–26, doi:10.1016/j.pss.2013.11.008.

[5] Chin, A., Coelho, R., Nugent, R., Munakata, R., and Puig-Suari, J., "CubeSat: The Pico-satellite Standard for Research and Education," in "Proceedings of the AIAA Space Conference & Exposition," San Diego, USA, 2008, doi:10.2514/6.2008-7734.

[6] Sternberg, D., Essmiller, J., Colley, C., Klesh, A., and Krajewski, J., "Attitude Control System for the Mars Cube One Spacecraft," in "41st IEEE Aerospace Conference," Big Sky, USA, 2020, doi:10.1109/AERO.2019.8741816.

[7] Lemmer, K., "Propulsion for CubeSats," *Acta Astronautica*, Vol. 134, 2017, pp. 231–243, doi:10.1016/j.actaastro.2017.01.048.

[8] Krejci, D., Jenkins, M. G., and Lozano, P., "Staging of Electric Propulsion Systems: Enabling an Interplanetary CubeSat," *Acta Astronautica*, Vol. 160, 2019, pp. 175–182, doi:10.1016/j.actaastro.2019.04.031.

[9] Jia-Richards, O., Sternberg, D., Grebow, D., Mohan, S., and Lozano, P., "Feasibility of a Deep-Space CubeSat Mission with a Stage-Based Electrospray Propulsion System," in "Proceedings of the 41st IEEE Aerospace Conference," Big Sky, USA, 2020, doi:10.1109/AERO47225.2020.9172544.

[10] "NASA's Mission Operations and Communications Services," Tech. rep., NASA Jet Propulsion Laboratory, 2014.

[11] Gamero-Castano, M. and Fernandez De La Mora, J., "Direct Measurement of Ion Evaporation Kinetics from Electrified Liquid Surfaces," *The Journal of Chemical Physics*, Vol. 113, No. 2, 2000, pp. 815–832,
doi:10.1063/1.481857.

[12] Gamero-Castano, M. and Hruby, V., "Electrospray as a Source of Nanoparticles for Efficient Colloid Thrusters," *Journal of Propulsion and Power*, Vol. 17, No. 5, 2001, pp. 977–987,
doi:10.2514/2.5858.

[13] Chiu, Y.-H., Austin, B. L., Dressler, R. A., Levandier, D., Murray, P. T., Lozano, P., and Martinez-Sanchez, M., "Mass Spectrometric Analysis of Colloid Thruster Ion Emission from Selected Propellants," *Journal of Propulsion and Power*, Vol. 21, No. 3, 2005, pp. 416–423,
doi:10.2514/1.9690.

[14] Ziemer, J. et al., "Colloid Microthruster Flight Performance Results from Space Technology 7 Disturbance Reduction System," in "Proceedings of the 35th International Electric Propulsion Conference," Atlanta, USA, 2017.

[15] Ziemer, J. K. et al., "Incorporating Lessons Learned into LISA Colloid Microthruster Technology Development," in "AIAA Propulsion and Energy Forum," Indianapolis, USA, 2019,
doi:10.2514/6.2019-3814.

[16] Bartoli, C., Von Rohden, H., Thompson, S., and Blommers, J., "A Liquid Caesium Field Ion Source for Space Propulsion," *Journal of Physics D: Applied Physics*, Vol. 17, No. 12, 1984, p. 2473,
doi:10.1088/0022-3727/17/12/014.

[17] Krejci, D., Hugonnaud, V., Schönherr, T., Little, B., Reissner, A., Seifert, B., Koch, Q., Bosch Borras, E., and Gonzalez del Amo, J., "Full Performance Mapping of the IFM Nano Thruster, Including Direct Thrust Measurements," *Journal of Small Satellites*, Vol. 8, No. 2, 2019, pp. 881–893.

[18] Rebelo, L. P. N., Canongia Lopes, J. N., Esperanca, J. M. S. S., and Filipe, E., "On the Critical Temperature, Normal Boiling Point, and Vapor Pressure of Ionic Liquids," *The Journal of Physical Chemistry B*, Vol. 109, No. 13, 2005, pp. 6040–6043,
doi:10.1021/jp050430h.

[19] Earle, M. J., Esperanca, J. M. S. S., Gilea, M. A., Canongia Lopes, J. N., Rebelo, L. P. N., Magee, J. W., Seddon, K. R., and Widegren, J. A., "The Distillation and Volatility of Ionic Liquids," *Nature*, Vol. 439, No. 7078, 2006, pp. 831–834,
doi:10.1038/nature04451.

[20] Lozano, P. and Martinez-Sanchez, M., "Ionic Liquid Ion Sources: Characterization of Externally Wetted Emitters," *Journal of Colloid and Interface Science*, Vol. 282, No. 2, 2004, pp. 415–421,
doi:10.1016/j.jcis.2004.08.132.

[21] Lozano, P. C., "Energy Properties of an EMI-Im Ionic Liquid Ion Source," *Journal of Physics D: Applied Physics*, Vol. 39, No. 1, 2005, p. 126, doi:10.1088/0022-3727/39/1/020.

[22] Legge Jr, R. S. and Lozano, P. C., "Electrospray Propulsion Based on Emitters Microfabricated in Porous Metals," *Journal of Propulsion and Power*, Vol. 27, No. 2, 2011, pp. 485–495, doi:10.2514/1.50037.

[23] Courtney, D. G., Li, H. Q., and Lozano, P., "Emission Measurements from Planar Arrays of Porous Ionic Liquid Ion Sources," *Journal of Physics D: Applied Physics*, Vol. 45, No. 48, 2012, p. 485203, doi:10.1088/0022-3727/45/48/485203.

[24] Krejci, D., Mier-Hicks, F., Thomas, R., Haag, T., and Lozano, P. C., "Emission Characteristics of Passively Fed Electrospray Microthrusters with Propellant Reservoirs," *Journal of Spacecraft and Rockets*, Vol. 54, No. 2, 2017, pp. 447–458, doi:10.2514/1.A33531.

[25] Mier-Hicks, F. and Lozano, P. C., "Electrospray Thrusters as Precise Attitude Control Actuators for Small Satellites," *Journal of Guidance, Control, and Dynamics*, Vol. 40, No. 3, 2017, pp. 642–649, doi:10.2514/1.G000736.

[26] Krejci, D. and Lozano, P., "Scalable Ionic Liquid Electrospray Thrusters for Nanosatellites," in "39th Annual Guidance and Control Conference," Breckenridge, USA, 2016.

[27] Petro, E. M., Bruno, A. R., Lozano, P. C., Perna, L. E., and Freeman, D. S., "Characterization of the TILE Electrospray Emitters," in "AIAA Propulsion and Energy Forum," Virtual Event, 2020, doi:10.2514/6.2020-3612.

[28] Rayman, M. D. et al., "Dawn: A Mission in Development for Exploration of Main Belt Asteroids Vesta and Ceres," *Acta Astronautica*, Vol. 58, No. 11, 2006, pp. 605–616, doi:10.1016/j.actaastro.2006.01.014.

[29] Krejci, D., Mier-Hicks, F., Fucetola, C., Lozano, P., Schouten, A. H., and Martel, F., "Design and Characterization of a Scalable ion Electrospray Propulsion System," in "Proceedings of the 34th International Electric Propulsion Conference," Hyogo-Kobe, Japan, 2015.

[30] Grustan-Gutierrez, E. and Gamero-Castaño, M., "Microfabricated Electrospray Thruster Array with High Hydraulic Resistance Channels," *Journal of Propulsion and Power*, Vol. 33, No. 4, 2017, pp. 984–991, doi:10.2514/1.B36268.

[31] Rojas-Herrera, J., Fucetola, C., Krejci, D., Freeman, D., Jivanescu, I., and Lozano, P. C., "Porous Materials for Ion-Electrospray Spacecraft Micro-Engines," *Nanomechanics and Micromechanics*, Vol. 7, No. 3, Paper 04017006, doi:10.1061/(ASCE)NM.2153-5477.0000121.

[32] Rojas-Herrera, J. and Lozano, P. C., "Mitigation of Anomalous Expansion of Carbon Xerogels and Controllability of Mean-Pore-Size by Changes in Mold Geometry," *Journal of Non-Crystalline Solids*, Vol. 458, 2017, pp. 22–27, doi:10.1016/j.jnoncrysol.2016.12.015.

[33] Guerra-Garcia, C., Krejci, D., and Lozano, P., "Spatial Uniformity of the Current Emitted by an Array of Passively Fed Electrospray Porous Emitters," *Journal of Physics D: Applied Physics*, Vol. 49, No. 11, Paper 115503, doi:10.1088/0022-3727/49/11/115503.

[34] Coffman, C., Martinez-Sanchez, M., Higuera, F. J., and Lozano, P. C., "Structure of the Menisci of Leaky Dielectric Liquids During Electrically-Assisted Evaporation of Ions," *Applied Physics Letters*, Vol. 109, No. 23, Paper 231602, doi:10.1063/1.4971778.

[35] Brikner, N. and Lozano, P. C., "The Role of Upstream Distal Electrodes in Mitigating Electrochemical Degradation of Ionic Liquid Ion Sources," *Applied Physics Letters*, Vol. 101, No. 19, Paper 193504, doi:10.1063/1.4766293.

[36] Jia-Richards, O. and Lozano, P. C., "Stage-Based Electrospray Propulsion System for Deep-Space Exploration with CubeSats," in "Proceedings of the 40th IEEE Aerospace Conference," Big Sky, USA, 2019, doi:10.1109/AERO.2019.8742094.

[37] Jia-Richards, O. and Lozano, P. C., "Laboratory Demonstration of a Staging System for Electrospray Thrusters," in "Proceedings of the 36th International Electric Propulsion Conference," Vienna, Austria, 2019.

[38] Jia-Richards, O. and Lozano, P. C., "Analytical Framework for Staging of Space Propulsion Systems," *Journal of Propulsion and Power*, Vol. 36, No. 4, 2020, pp. 527–534, doi:10.2514/1.B37722.

[39] Jia-Richards, O. and Lozano, P. C., "Redundancy for Asteroid Detumbling via Staging," in "Proceedings of the 42nd IEEE Aerospace Conference," Big Sky, USA, 2021, doi:10.1109/AERO50100.2021.9438201.

[40] Jia-Richards, O. and Lozano, P. C., "Analytical Guidance for Circular Orbit Transfers with Staging of Space Propulsion Systems," *Acta Astronautica*, Vol. 179, 2021, pp. 69–77, doi:10.1016/j.actaastro.2020.10.034.

[41] Pettersson, G. M., Jia-Richards, O., and Lozano, P. C., "Development and Laboratory Testing of a CubeSat-Compatible Staged Ionic-Liquid Electrospray Propulsion System," in "Proceedings of the AIAA SciTech Forum," San Diego, USA, 2022, doi:10.2514/6.2022-0040.

[42] Cybulski, R. J., Shellhammer, D. M., Lovell, R. R., Domino, E. J., and Kotnik, J. T., "Results from SERT I Ion Rocket Flight Test," Tech. rep., NASA, 1965.

[43] Nieberding, W. C., Lesco, D. J., and Berkopec, F. D., "Comparative In-Flight Thrust Measurements of the SERT II Ion Thruster," Tech. rep., NASA, 1970.

[44] Young, B. and Martin-Mur, T., "Using Telemetry to Navigate the MarCO CubeSats to Mars," *Proceedings of the 18th Australian Aerospace Congress*, Melbourne, Australia, 2019.

[45] Pugia, S., Cofer, A., and Alexeenko, A., "Characterization of Film-Evaporating Microcapillaries for Water-Based Microthrusters," *Acta Astronautica*, doi:10.1016/j.actaastro.2020.09.011.

[46] Samples, S. A. and Wirz, R. E., "Development of the MiXI Thruster with the ARCH Discharge," *Plasma Research Express*, Vol. 2, No. 2, 2020, p. 025008, doi:10.1088/2516-1067/ab906d.

[47] Krishnan, M., Velas, K., and Leemans, S., "Metal Plasma Thruster for Small Satellites," *Journal of Propulsion and Power*, Vol. 36, No. 4, 2020, pp. 535–539, doi:10.2514/1.B37603.

[48] Nakamura, T., Krech, R. H., and Smith, B. K., "Pulsed Electrogasdynamic Thruster for In-Space Propulsion," *Journal of Propulsion and Power*, Vol. 36, No. 6, 2020, pp. 950–960, doi:10.2514/1.B37298.

[49] Chen, C., Chen, M., Fan, W., and Zhou, H., "Effects of Non-Uniform Operation of Emission Sites on Characteristics of a Porous Electrospray Thruster," *Acta Astronautica*, Vol. 178, 2021, pp. 192–202, doi:10.1016/j.actaastro.2020.09.002.

[50] Wiesel, W. E., *Spaceflight Dynamics*, McGraw-Hill, New York, USA, pp. 90–92, 2nd ed., 1997.

[51] Kerslake, W. R., Goldman, R. G., and Nieberding, W. C., "SERT II: Mission, Thruster Performance, and In-Flight Thrust Measurements," *Journal of Spacecraft and Rockets*, Vol. 8, No. 3, 1971, pp. 213–224, doi:10.2514/3.30250.

[52] Schroeder, M., Womack, C., and Gagnon, A., "Maneuver Planning for Demonstration of a Low-Thrust Electric Propulsion System," *Proceedings of the 34th Annual Small Satellite Conference*, Logan, USA, 2020.

[53] Krejci, D., Reissner, A., Schönherr, T., Seifert, B., Saleem, Z., and Alejos, R., "Recent Flight Data from IFM Nano Thrusters in a Low-Earth Orbit," in "Proceedings of the 36th International Electric Propulsion Conference," University of Vienna, Austria, 2019.

[54] Goff, G. M., Black, J. T., and Beck, J. A., "Orbit Estimation of a Continuously Thrusting Spacecraft Using Variable Dimension Filters," *Journal of Guidance, Control, and Dynamics*, Vol. 38, No. 12, 2015, pp. 2407–2420, doi:10.2514/1.G001091.

[55] Craft, K. J., Pernicka, H. J., and Darling, J. E., "Performance Determination of a Multi-Mode Thruster Using GPS and Star Tracker Data," *Proceedings of the 41st IEEE Aerospace Conference*, Big Sky, USA, 2020, doi:10.1109/AERO47225.2020.9172624.

[56] Jia-Richards, O. and Lozano, P. C., "Progress Towards Efficient Thrust Estimation for Low-Acceleration Propulsion Systems in Low-Earth Orbit," in "Proceedings of the 37th International Electric Propulsion Conference," Cambridge, USA, 2022.

[57] Jia-Richards, O. and Lozano, P. C., "On-Orbit Thrust Inference from Low-Acceleration Orbital Maneuvers via the Ensemble Kalman Update," In preparation.

[58] Jia-Richards, O., "Segmented Reconstruction of Low-Acceleration Orbital Maneuvers," In preparation.

[59] Jia-Richards, O., Corrado, M., and Lozano, P. C., "Thrust Inference for Ionic-Liquid Electrospray Thrusters on a Magnetically-Levitating Thrust Balance," in "Proceedings of the 37th International Electric Propulsion Conference," Cambridge, USA, 2022.

[60] Jia-Richards, O. and Lozano, P. C., "Ensemble Kalman Update for Inference of Spatial Uniformity of Emission across an Electrospray Array," in "Proceedings of the 43rd IEEE Aerospace Conference," Big Sky, USA, 2022.

[61] Evensen, G., *Data Assimilation: The Ensemble Kalman Filter*, Springer Science & Business Media, 2nd ed., 2009, doi:10.1007/978-3-642-03711-5.

[62] Hughes, S. P., Qureshi, R. H., Cooley, D. S., Parker, J. J. K., and Grubb, T. G., "Verification and Validation of the General Mission Analysis Tool (GMAT)," in "Proceedings of the AIAA/AAS Astrodynamics Specialist Conference," San Diego, USA, 2014.

[63] Tapley, B. D. et al., "The Joint Gravity Model 3," *Journal of Geophysical Research*, Vol. 101, No. B12, 1996, pp. 28029–28049, doi:10.1029/96JB01645.

[64] Hedin, A. E., "Extension of the MSIS Thermosphere Model Into the Middle and Lower Atmosphere," *Journal of Geophysical Research*, Vol. 96, No. A2, 1991, pp. 1159–1172, doi:10.1029/90JA02125.

[65] Wertz, J. R., Everett, D. F., and Puschell, J. J., *Space Mission Engineering: The New SMAD*, Microcosm Press, 2011.

[66] Prussing, J. E. and Conway, B. A., *Orbital Mechanics*, Oxford University Press, New York, USA, pp. 179–196, 2nd ed.

[67] Jones, E. M., "Recovery of Thrust Magnitude from Minitrack Data for the SERT-II Spacecraft," Tech. rep., NASA, 1970.

[68] Walton, P., Cannon, J., Damitz, B., Downs, T., Glick, D., Holtom, J., Kohls, N., Laraway, A., Matheson, I., Redding, J., et al., "Passive CubeSats for Remote Inspection of Space Vehicles," *Journal of Applied Remote Sensing*, Vol. 13, No. 3, doi:10.1117/1.JRS.13.032505.

[69] Pedrotty, S., Sullivan, J., Gambone, E., and Kirven, T., "Seeker Free-Flying Inspector GNC System Overview," in "Proceedings of the 42nd AAS Guidance & Control Conference," Breckenridge, USA, 2019.

[70] Henshaw, C., Healy, L., and Roderick, S., "LIIVe: A Small, Low-Cost Autonomous Inspection Vehicle," in "Proceedings of the AIAA Space Conference & Exposition," Pasadena, USA, 2009,
doi:10.2514/6.2009-6544.

[71] Fourie, D., Tweddle, B. E., Ulrich, S., and Saenz-Otero, A., "Flight Results of Vision-Based Navigation for Autonomous Spacecraft Inspection of Unknown Objects," *Journal of Spacecraft and Rockets*, Vol. 51, No. 6, 2014, pp. 2016–2026,
doi:10.2514/1.A32813.

[72] Kim, S. C., Shepperd, S. W., Norris, H. L., Goldberg, H. R., and Wallace, M. S., "Mission Design and Trajectory Analysis for Inspection of a Host Spacecraft by a Nicrosatellite," in "Proceedings of the 28th IEEE Aerospace Conference," Big Sky, USA, 2007,
doi:10.1109/AERO.2007.352811.

[73] Corpino, S. and Stesina, F., "Inspection of the Cis-Lunar Station Using Multi-Purpose Autonomous CubeSats," *Acta Astronautica*, Vol. 175, 2020, pp. 591–605,
doi:10.1016/j.actaastro.2020.05.053.

[74] Kannenberg, K. C. and Boyd, I. D., "Three-Dimensional Monte Carlo Simulations of Plume Impingement," *Journal of Thermophysics and Heat Transfer*, Vol. 13, No. 2, 1999, pp. 226–235,
doi:10.2514/2.6440.

[75] Tajmar, M., González, J., and Hilgers, A., "Modeling of Spacecraft-Environment Interactions on SMART-1," *Journal of Spacecraft and Rockets*, Vol. 38, No. 3, 2001, pp. 393–399,
doi:10.2514/2.3697.

[76] Richards, A., Schouwenaars, T., How, J. P., and Feron, E., "Spacecraft Trajectory Planning with Avoidance Constraints Using Mixed-Integer Linear Programming," *Journal of Guidance, Control, and Dynamics*, Vol. 25, No. 4, 2002, pp. 755–764,
doi:10.2514/2.4943.

[77] Breger, L. and How, J. P., "Safe Trajectories for Autonomous Rendezvous of Spacecraft," *Journal of Guidance, Control, and Dynamics*, Vol. 31, No. 5, 2008, pp. 1478–1489,
doi:10.2514/1.29590.

[78] Deaconu, G., Louembet, C., and Théron, A., "Designing Continuously Constrained Spacecraft Relative Trajectories for Proximity Operations," *Journal of Guidance, Control, and Dynamics*, Vol. 38, No. 7, 2015, pp. 1208–1217,
doi:10.2514/1.G000283.

[79] Hartley, E. N., Trodden, P. A., Richards, A. G., and Maciejowski, J. M., "Model Predictive Control System Design and Implementation for Spacecraft Rendezvous,"

Control Engineering Practice, Vol. 20, No. 7, 2012, pp. 695–713, doi:10.1016/j.conengprac.2012.03.009.

[80] Di Cairano, S., Park, H., and Kolmanovsky, I., "Model Predictive Control Approach for Guidance of Spacecraft Rendezvous and Proximity Maneuvering," *International Journal of Robust and Nonlinear Control*, Vol. 22, No. 12, 2012, pp. 1398–1427, doi:10.1002/rnc.2827.

[81] Leomanni, M., Rogers, E., and Gabriel, S. B., "Explicit Model Predictive Control Approach for Low-Thrust Spacecraft Proximity Operations," *Journal of Guidance, Control, and Dynamics*, Vol. 37, No. 6, 2014, pp. 1780–1790, doi:10.2514/1.G000477.

[82] Weiss, A., Baldwin, M., Erwin, R. S., and Kolmanovsky, I., "Model Predictive Control for Spacecraft Rendezvous and Docking: Strategies for Handling Constraints and Case Studies," *IEEE Transactions on Control Systems Technology*, Vol. 23, No. 4, 2015, pp. 1638–1647, doi:10.1109/TCST.2014.2379639.

[83] Jackson, M. C., *A Six Degree of Freedom, Plume-Fuel Optimal Trajectory Planner for spacecraft Proximity Operations Using an A* Node Search*, Master's thesis, Massachusetts Institute of Technology, 1994.

[84] DiGirolamo, L. J., Hacker, K. A., Hoskins, A. H., and Spencer, D. B., "A Hybrid Motion Planning Algorithm for Safe and Efficient, Close Proximity, Autonomous Spacecraft Missions," in "Proceedings of the AIAA/AAS Astrodynamics Specialist Conference," San Diego, USA, 2014, doi:10.2514/6.2014-4130.

[85] Miele, A., Weeks, M., and Ciarcia, M., "Optimal Trajectories for Spacecraft Rendezvous," *Journal of Optimization Theory and Applications*, Vol. 132, No. 3, 2007, pp. 353–376, doi:10.1007/s10957-007-9166-4.

[86] Spehar, P. T. and Le, T. Q., "Automating an Orbiter Approach to Space Station Freedom to Minimize Plume Impingement," Tech. rep., NASA, 1991.

[87] Miller, D. W., Sedwick, R. J., Kong, E. M., and Schweighart, S., "Electromagnetic Formation Flight for Sparse Aperture Telescopes," in "Proceedings of the 23rd IEEE Aerospace Conference," Big Sky, USA, 2002, doi:10.1109/AERO.2002.1035616.

[88] Broschart, S. B. and Scheeres, D. J., "Control of Hovering Spacecraft Near Small Bodies: Application to Asteroid 25143 Itokawa," *Journal of Guidance, Control, and Dynamics*, Vol. 28, No. 2, 2005, pp. 343–354, doi:10.2514/1.3890.

[89] Broschart, S. B. and Scheeres, D. J., "Boundedness of Spacecraft Hovering under Dead-Band Control in Time-Invariant Systems," *Journal of Guidance, Control, and Dynamics*, Vol. 30, No. 2, 2007, pp. 601–610, doi:10.2514/1.20179.

[90] Huang, X., Yan, Y., and Huang, Z., "Finite-time Control of Underactuated Spacecraft Hovering," *Control Engineering Practice*, Vol. 68, 2017, pp. 46–62, doi:10.1016/j.conengprac.2017.08.006.

[91] Kawaguchi, J., Fujiwara, A., and Uesugi, T., "Hayabusa—Its Technology and Science Accomplishment Summary and Hayabusa-2," *Acta Astronautica*, Vol. 62, No. 10, 2008, pp. 639–647,
doi:10.1016/j.actaastro.2008.01.028.

[92] Guelman, M., "Closed-loop Control of Close Orbits Around Asteroids," *Journal of Guidance, Control, and Dynamics*, Vol. 38, No. 5, 2015, pp. 854–860,
doi:10.2514/1.G000158.

[93] Guelman, M. M., "Closed-loop Control for Global Coverage and Equatorial Hovering About an Asteroid," *Acta Astronautica*, Vol. 137, 2017, pp. 353–361,
doi:10.1016/j.actaastro.2017.04.035.

[94] Shi, Y., Wang, Y., Misra, A. K., and Xu, S., "Station-Keeping for Periodic Orbits near Strongly Perturbed Binary Asteroid Systems," *Journal of Guidance, Control, and Dynamics*, Vol. 43, No. 2, 2020, pp. 319–326,
doi:10.2514/1.G004638.

[95] Dunham, D. W., Farquhar, R. W., McAdams, J. V., Holdridge, M., Nelson, R., Whittenburg, K., Antreasian, P., Chesley, S., Helfrich, C., Owen, W. M., et al., "Implementation of the First Asteroid Landing," *Icarus*, Vol. 159, No. 2, 2002, pp. 433–438,
doi:10.1006/icar.2002.6911.

[96] Veverka, J., Farquhar, B., Robinson, M., Thomas, P., Murchie, S., Harch, A., Antreasian, P., Chesley, S., Miller, J., Owen, W., et al., "The Landing of the NEAR-Shoemaker Spacecraft on Asteroid 433 Eros," *Nature*, Vol. 413, No. 6854, 2001, pp. 390–393,
doi:doi.org/10.1038/35096507.

[97] Yoshimitsu, T., Kawaguchi, J., Hashimoto, T., Kubota, T., Uo, M., Morita, H., and Shirakawa, K., "Hayabusa-Final Autonomous Descent and Landing Based on Target Marker Tracking," *Acta Astronautica*, Vol. 65, No. 5-6, 2009, pp. 657–665,
doi:10.1016/j.actaastro.2009.01.074.

[98] Guelman, M. and Harel, D., "Power Limited Soft Landing on an Asteroid," *Journal of Guidance, Control, and Dynamics*, Vol. 17, No. 1, 1994, pp. 15–20,
doi:10.2514/3.21153.

[99] Furfaro, R., Cersosimo, D., and Wibben, D. R., "Asteroid Precision Landing via Multiple Sliding Surfaces Guidance Techniques," *Journal of Guidance, Control, and Dynamics*, Vol. 36, No. 4, 2013, pp. 1075–1092,
doi:10.2514/1.58246.

[100] Herrera-Sucarrat, E., Palmer, P., and Roberts, R., "Asteroid Observation and Landing Trajectories using Invariant Manifolds," *Journal of Guidance, Control, and Dynamics*, Vol. 37, No. 3, 2014, pp. 907–920,
doi:10.2514/1.59594.

[101] Jia-Richards, O. and Lozano, P. C., "Analytical Maneuver Library for Remote Inspection with an Underactuated Spacecraft," *Journal of Guidance, Control, and Dynamics*, doi:10.2514/1.G005766. In press.

[102] Jenkins, R. O. and Trodden, W. G., *Electron and Ion Emission From Solids*, Dover Publications, New York, New York, chapter 5, pp. 44–53, 1st ed., 1965.

[103] Manka, R. H., "Plasma and Potential at the Lunar Surface," in "Photon and Particle Interactions with Surfaces in Space," Springer, pp. 347–361, 1973.

[104] Jenkins, R. O. and Trodden, W. G., *Electron and Ion Emission From Solids*, Dover Publications, New York, New York, chapter 6, pp. 54–70, 1st ed., 1965.

[105] McDaniel, E. W., *Collision Phenomena in Ionized Gases*, John Wiley & Sons, New York, New York, chapter 13, pp. 626–692, 1st ed., 1964.

[106] Minnebaev, K., Rau, E., and Tatarintsev, A., "Charging Dielectrics when Bombarded with Ar+ Ions of Medium Energies," *Physics of the Solid State*, Vol. 61, No. 6, 2019, pp. 1013–1016.

[107] Andersen, C., Roden, H., and Robinson, C., "Negative Ion Bombardment of Insulators to Alleviate Surface Charge-Up," *Journal of Applied Physics*, Vol. 40, No. 8, 1969, pp. 3419–3420,
doi:10.1063/1.1658212.

[108] Freeman, J. W. and Ibrahim, M., "Lunar Electric Fields, Surface Potential and Associated Plasma Sheaths," *The Moon*, Vol. 14, No. 1, 1975, pp. 103–114,
doi:10.1007/BF00562976.

[109] Halekas, J. S., Delory, G. T., Lin, R. P., Stubbs, T. J., and Farrell, W. M., "Lunar Prospector Observations of the Electrostatic Potential of the Lunar Surface and Its Response to Incident Currents," *Journal of Geophysical Research: Space Physics*, Vol. 113, Article 9,
doi:10.1029/2008JA013194.

[110] Rennilson, J. J. and Criswell, D. R., "Surveyor Observations of Lunar Horizon-Glow," *The Moon*, Vol. 10, No. 2, 1974, pp. 121–142,
doi:10.1007/BF00655715.

[111] Lee, P., "Dust Levitation on Asteroids," *Icarus*, Vol. 124, No. 1, 1996, pp. 181–194,
doi:10.1006/icar.1996.0197.

[112] Hirata, N. and Miyamoto, H., "Dust Levitation as a Major Resurfacing Process on the Surface of a Saturnian Icy Satellite, Atlas," *Icarus*, Vol. 220, No. 1, 2012, pp. 106–113,
doi:10.1016/j.icarus.2012.03.028.

[113] Robinson, M. S., Thomas, P. C., Veverka, J., Murchie, S., and Carcich, B., "The Nature of Ponded Deposits on Eros," *Nature*, Vol. 413, No. 6854, 2001, pp. 386–400,
doi:10.1038/35096518.

[114] Murphy, T. W., Adelberger, E., Battat, J. B. R., Hoyle, C. D., McMillan, R. J., Michelsen, E. L., Samad, R. L., Stubbs, C. W., and Swanson, H. E., "Long-term

Degradation of Optical Devices on the Moon," *Icarus*, Vol. 208, No. 1, 2010, pp. 31–35,
doi:10.1016/j.icarus.2010.02.015.

[115] Vernazza, P., Delbo, M., King, P. L., Izawa, M. R. M., Olofsson, J., Lamy, P., Cipriani, F., Binzel, R. P., Marchis, F., Merín, B., and Tamanai, A., "High Surface Porosity as the Origin of Emissivity Features in Asteroid Spectra," *Icarus*, Vol. 221, No. 2, 2012, pp. 1162–1172,
doi:10.1016/j.icarus.2012.04.003.

[116] Nordheim, T., Jones, G., Halekas, J., Roussos, E., and Coates, A., "Surface Charging and Electrostatic Dust Acceleration at the Nucleus of Comet 67P During Periods of Low Activity," *Planetary and Space Science*, Vol. 119, 2015, pp. 24–35,
doi:10.1016/j.pss.2015.08.008.

[117] Thomas, N. et al., "Redistribution of Particles Across the Nucleus of Comet 67P/Churyumov-Gerasimenko," *Astronomy and Astrophysics*, Vol. 583, Article 17,
doi:10.1051/0004-6361/201526049.

[118] Wang, X., Horányi, M., and Robertson, S., "Experiments on Dust Transport in Plasma to Investigate the Origin of the Lunar Horizon Glow," *Journal of Geophysical Research: Space Physics*, Vol. 114, Article 5,
doi:10.1029/2008JA013983.

[119] Sheridan, T. E., Goree, J., Chiu, Y. T., Rairden, R. L., and Kiessling, J. A., "Observation of Dust Shedding from Material Bodies in a Plasma," *Journal of Geophysical Research: Space Physics*, Vol. 97, Article 3,
doi:10.1029/91JA02801.

[120] Flanagan, T. M. and Goree, J., "Dust Release from Surfaces Exposed to Plasma," *Physics of Plasmas*, Vol. 13, No. 12, Paper 123504,
doi:10.1063/1.2401155.

[121] Wang, X., Horányi, M., and Robertson, S., "Investigation of Dust Transport on the Lunar Surface in a Laboratory Plasma with an Electron Beam," *Journal of Geophysical Research: Space Physics*, Vol. 115, Article 11,
doi:10.1029/2010JA015465.

[122] Wang, X., Colwell, J., Horanyi, M., and Robertson, S., "Charge of Dust on Surfaces in Plasma," *IEEE transactions on plasma science*, Vol. 35, No. 2, 2007, pp. 271–279,
doi:10.1109/TPS.2007.891639.

[123] Wang, X., Horányi, M., and Robertson, S., "Dust Transport Near Electron Beam Impact and Shadow Boundaries," *Planetary and Space Science*, Vol. 59, No. 14, 2011, pp. 1791–1794,
doi:10.1016/j.pss.2010.12.005.

[124] Wang, X., Schwan, J., Hsu, H. W., Grün, E., and Horányi, M., "Dust Charging and Transport on Airless Planetary Bodies," *Geophysical Research Letters*, Vol. 43, No. 12, 2016, pp. 6103–6110,
doi:10.1002/2016GL069491.

[125] Quadrelli, M. B., Garrett, H., Castillo, J., Stoica, A., Ono, M., Christianson, C., Lusso, D., and Schaub, H., "Active Electrostatic Flight for Airless Bodies," *Proceedings of the 38th IEEE Aerospace Conference*, Big Sky, USA, 2017, doi:10.1109/AERO.2017.7943821.

[126] Bechini, M., Quadrelli, M. B., Lavagna, M., and Wang, J. J., "Hovering of an Electrically Actuated Spacecraft in a Small-Body Plasma Field," *Journal of Spacecraft and Rockets*, Vol. 58, No. 5, 2021, pp. 1461–1476, doi:10.2514/1.A34954.

[127] Albee, K., Cabrales Hernandez, A., Jia-Richards, O., and Terán Espinoza, A., "Real-time Motion Planning in Unknown Environments for Legged Robotic Planetary Exploration," in "Proceedings of the 41st IEEE Aerospace Conference," Big Sky, USA, 2020, doi:10.1109/AERO47225.2020.9172596.

[128] Jia-Richards, O., Hampl, S. K., and Lozano, P. C., "Electrostatic Levitation on Atmosphere-Less Planetary Bodies with Ionic Liquid Ion Sources," *Journal of Spacecraft and Rockets*, Vol. 58, No. 6, 2021, pp. 1694–1703, doi:10.2514/1.A35001.

[129] Lev, D. R., Mikellides, I. G., Pedrini, D., Goebel, D. M., Jorns, B. A., and McDonald, M. S., "Recent Progress in Research and Development of Hollow Cathodes for Electric Propulsion," *Reviews of Modern Plasma Physics*, Vol. 3, No. 6, doi:10.1007/s41614-019-0026-0.

[130] Miller, C. E., *Characterization of Ion Cluster Fragmentation in Ionic Liquid Ion Sources*, Ph.D. thesis, Massachusetts Institute of Technology, 2019.

[131] Mier-Hicks, F. and Lozano, P. C., "Spacecraft-Charging Characteristics Induced by the Operation of Electrospray Thrusters," *Journal of Propulsion and Power*, Vol. 33, No. 2, 2017, pp. 456–467, doi:10.2514/1.B36292.

[132] Whipple, E. C., "Potentials of Surfaces in Space," *Reports on Progress in Physics*, Vol. 44, No. 11, 1981, pp. 1197–1250, doi:10.1088/0034-4885/44/11/002.

[133] Halekas, J. S., Lin, R. P., and Mitchell, D. L., "Large Negative Lunar Surface Potentials in Sunlight and Shadow," *Geophysical Research Letters*, Vol. 32, 2005, p. L09102, doi:10.1029/2005GL022627.

[134] Mommert, M. et al., "Physical Properties of Near-Earth Asteroid 2011 MD," *The Astrophysical Journal Letters*, Vol. 789, No. 1, doi:10.1088/2041-8205/789/1/L22.

[135] Warner, B. D., Harris, A. W., and Pravec, P., "The Asteroid Lightcurve Database," *Icarus*, Vol. 202, No. 1, 2009, pp. 134–146, doi:10.1016/j.icarus.2009.02.003.

[136] Krasinsky, G. A., Pitjeva, E. V., Vasilyev, M. V., and Yagudina, E. I., "Hidden Mass in the Asteroid Belt," *Icarus*, Vol. 158, No. 1, 2002, pp. 98–105, doi:10.1006/icar.2002.6837.

[137] de Pater, I. and Lissauer, J. J., *Planetary Sciences*, Cambridge University Press, Updated 2nd ed., 2015.

[138] Pravec, P. and Harris, A. W., "Fast and Slow Rotation of Asteroids," *Icarus*, Vol. 148, No. 1, 2000, pp. 12–20, doi:10.1006/icar.2000.6482.

[139] Kwiatkowski, T. et al., "Photometry of 2006 RH_{120}: An Asteroid Temporary Captured into a Geocentric Orbit," *Astronomy and Astrophysics*, Vol. 495, No. 3, 2009, pp. 967–974, doi:10.1051/0004-6361:200810965.

[140] Pravec, P., Hergenrother, C., Whiteley, R., Šarounová, L., Kušnirák, P., and Wolf, M., "Fast Rotating Asteroids 1999 TY_2, 1999 SF_{10}, and 1998 WB_2," *Icarus*, Vol. 147, No. 2, 2000, pp. 477–486, doi:10.1006/icar.2000.6458.

[141] García Yárnoz, D., Sanchez, J. P., and McInnes, C. R., "Easily Retrievable Objects among the NEO Population," *Celestial Mechanics and Dynamical Astronomy*, Vol. 116, No. 4, 2013, pp. 367–388, doi:10.1007/s10569-013-9495-6.

[142] Griffiths, D. J., *Introduction to Electrodynamics*, Cambridge University Press, 4th ed., 2017.

[143] Morea, S. F., "The Lunar Roving Vehicle - Historical Perspective," *Proceedings of the 2nd Conference on Lunar Bases and Space Activities*, Houston, TX, 1992.

[144] Malenkov, M., "Self-Propelled Automatic Chassis of Lunokhood-1: History of Creation in Episodes," *Frontiers of Mechanical Engineering*, Vol. 11, No. 1, 2016, pp. 60–86, doi:10.1007/s11465-016-0370-5.

[145] Hruby, V., Gamero-Castaño, M., Cordero, J., Kolencik, J., and Martínez-Sánchez, M., "Colloid Thrusters for Micro and Nano-Satellites," , 1999. Final report, Phase I SBIR NASA.

[146] Ulamec, S. and Biele, J., "Surface Elements and Landing Strategies for Small Bodies Missions–Philae and Beyond," *Advances in Space Research*, Vol. 44, No. 7, 2009, pp. 847–858, doi:10.1016/j.asr.2009.06.009.